Preparation and Characterization of Nanocrystalline Cerium-based Oxides as a Carbon Monoxide Oxidation Catalyst

HO Chun Man

A Thesis Submitted in Partial Fulfillment

of the Requirements for the Degree of

Master of Philosophy

In

Environmental Science

The Chinese University of Hong Kong

July 2005

MASTER OF PHILOSOPHY (2005) The Chinese University of Hong Kong

(Environmental Science)

TITLE: Preparation and Characterization of Nanocrystalline Cerium-based Oxides as a Carbon Monoxide Oxidation Catalyst.

AUTHOR: Ho Chun Man BSc (The Chinese University of Hong Kong)

SUPERVISOR: Prof. Jimmy C. Yu

NO. OF PAGES: XVI, 112

Thesis Committee:

Prof. Jimmy C. YU (Supervisor)

Prof. Hung Kay LEE (Chairman)

Prof. Chak Tong AU (External examiner)

Prof. Po Keung WONG (Internal examiner)

The work in this dissertation has been published in *Journal of Materials Chemistry* and *Chemistry of Materials*.

ABSTRACT

A series of hierarchically macro-mesoporous palladium-loaded cerium-zirconium mixed oxides ($Pd/Ce_xZr_{1-x}O_2$) were prepared by using a combined surfactant and colloidal crystal templating method. The $Pd/Ce_xZr_{1-x}O_2$ products possessed mesoporous structures and macrochannels. With increasing calcination temperature, better crystallization of the cubic phase and incorporation of more zirconium into the ceria lattice were observed. The extent of surface Ce^{3+} and oxygen vacancy on the samples were studied by XPS. The T_{50} and T_{90} for CO oxidation over Pd supported catalysts were 65 and 75°C respectively. These values were better than those obtained from catalysts without macrochannel structures and the one prepared by the co-precipitation method. Such high catalytic efficiency can be explained by the high crystal phase homogeneity, availability of more oxygen vacancy and enlarged surface area.

In the second part of the thesis, polycrystalline CeO_2 nanospheres, microrods and spindle-like particles were also prepared by a polyol synthesized approach. By controlling the duration of reaction and the concentration of the cerium precursor, CeO_2 in different morphologies could be selectively produced. Before calcination,

cerium formate microrods and spindle-like particles, and CeO_2 nanospheres were obtained. Products were transformed to CeO_2 and their nanostructures were intact after calcination. The order of bandgap energy of these samples was found to be microrods > nanospheres > spindle-like particles. The nanostructured samples exhibit higher activity on CO oxidation than bulk sample. The higher catalytic activity on CO conversion in spindle-like particles can be explained from the extent of Ce(IV) reduction , oxygen vacancies and reduced crystalline size.

摘要

本論文分二部分。論文第一部分報道了採用表面活性劑組裝和膠體粒子組裝相結合的方法，研製出了一系列具有分級中孔、大孔結構的新型 $Pd/Ce_xZr_{1-x}O_2$ 催化材料。實驗發現，催化劑燒結溫度升高有利於促進立方相二氧化鈰結晶生成，同時也有效地增加了鋯在二氧化鈰晶格中的摻雜量。對一氧化碳的氧化反應評價結果表明，這種新型的分級中孔、大孔材料比沒有大孔結構的催化劑具有更高的催化活性。新型催化劑具有的優異物理化學性能（比如大的表面積、更多的表面氧空位、及高度均勻的晶相）很好地解釋其所具有的良好催化性能。

論文的第二部分報導了多晶二氧化鈰納米球、微米棒、和梭狀微米棒的合成和性能。發現，通過反應時間及鈰前驅體溶度的控制，可以選擇性地合成不同形貌的二氧化鈰材料。試驗還發現，在樣品焙燒之前，得到的是甲酸鈰的微米棒和梭狀微米棒，以及二氧化鈰的納米球；焙燒後，這些物質能保持它們各自的形貌不變，並轉化成二氧化鈰。各樣品的帶隙能量均比體相二氧化鈰爲大，它們的帶隙能量大小順序是微米棒〉納米球〉梭狀微米棒。一氧化碳的催化氧化反應評價結果表明，同體相二氧化鈰相比，這些納米結構材料具有更高的催化活性。特別是梭狀二氧化鈰微米棒，其良好的催化性能可以從其表面四價態鈰的還原程度，氧空位以及細小的結晶體積來解釋。

DECLARATION

I hereby declare that this thesis entitled "Preparation and Characterization of Nanocrytalline Cerium-based Oxides as a Carbon Monoxide Oxidation Catalyst" has not been, either in whole or in part, previously submitted to any other institution for a degree or other qualification. It contains no materials previously published or written to another person, except where due reference is made in the text.

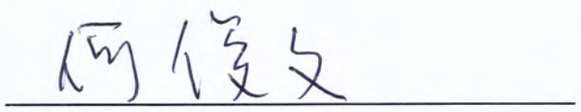

(HO Chun Man)

ACKNOWLEDGEMENT

I sincerely acknowledge my chief supervisor, Prof. Jimmy C. Yu, who gave me not only the opportunity to begin my MPhil study at The Chinese University of Hong Kong, but valuable advices and encouragement throughout my research and the preparation of this thesis. I am also thankful for his patience and effort in reviewing all the drafts of my thesis, this making my research possible.

I am very grateful to Prof. S. Y Lai from the Department of Chemistry, Hong Kong Baptist University for her kindness and technical support in the experimental study. Her comments are crucial to the improvement of my research.

My gratitude and thanks also go to my groupmates who supported me constantly in the past few years for doing the research and study. Finally, I would like to express my profound gratitude to my family. They are the inspirations of my life and my learning.

TABLE OF CONTENTS

LIST OF TABLES

LIST OF FIGURES

Chapter One

Introduction

1.1 Overview

Under the classification of rare-earth element, there are 15 lanthanide elements and 2 elements located above lanthanum in the periodic table, scandium and yttrium. The lanthanides are divided into two groups: the first four elements (La, Ce, Pr and Nd) are referred to as ceric or light rare-earths, while the other elements named the yttric or heavy rare-earth. Among these 15 lanthanide elements, ceria-based materials are used extensively as catalysts in industrial processes, ranging from catalysis automobile emission control,[1] styrene formation,[2] fuel cell,[3] gas sensor,[4] solid electrolytes,[5] and ceramic biomaterials.[6] Ceria provides a number of important functions in an automotive three-way catalytic converter (TWC). These include improving the activity for water-gas shift reaction,[7] stabilizing the surface area of the catalyst support [8] and provide the oxygen-storing capacity.[9] The performance of ceria in TWC can be enhanced by optimizing their structural properties. The objective of this study is to explore new ideas for modifying the structure of ceria.

1.2 Fundamental of CeO_2

Cerium with a $4f^2 5d^0 6s^2$ electron configuration can undergo a facile conversion between +3 and +4 formal oxidation states, and intermediate oxides whose composition is in the range Ce_2O_3-CeO_2 can be formed. Thermodynamic data indicate that the cerium metal is easily oxidized to Ce_2O_3 and CeO_2 (Table 1.1). The final stoichiometry is highly dependent on temperature and oxygen pressure. Cerium metal reacts with oxygen to form Ce_2O_3 at about 10^{-93} atm of oxygen at 573K. Ce_2O_3 can also be converted to homologous series Ce_nO_{2n-2m} if pressure increases to above 10^{-40} atm of oxygen, where CeO_2 starts to form.[2] Therefore, ceria catalysts are capable of storing oxygen under oxidizing conditions and releasing oxygen under reducing conditions through a transformation between Ce(IV) and Ce(III) oxidation states.[10]

Table 1.1 Thermodynamic properties of Ce oxides.[2]

Reaction	ΔH^o_{298} (kJmol^{-1})	ΔG^o_{298} (kJmol^{-1})	S^o_{298} (JK^{-1}mol^{-1})
$Ce + O_2 \rightleftharpoons CeO_2$	-1089	-1026	61.5
$2Ce + \frac{3}{2}O_2 \rightleftharpoons Ce_2O_3$	-1796	-1708	152
$Ce_2O_3 + \frac{1}{2}O_2 \rightleftharpoons 2CeO_2$	-191	-172	14.5

The effects of oxide anion vacancies and structural defects of ceria on catalysis have been studied since 1970s. These two factors are strongly correlated.[2] Oxide anion vacancies in CeO_2 can be generated by insertion of the foreign lower oxidation state metal cation or removal of O^{2-} ions from the CeO_2 lattice, according to the following equation,

$$4Ce^{4+}{}_{(s)} + O^{2-}{}_{(s)} \rightarrow 4Ce^{4+}{}_{(s)} + 2e^{-}/V_{(O,s)} + \frac{1}{2}O_2 \rightarrow 2Ce^{4+}, 2Ce^{3+}{}_{(s)} + V_{(O,s)} + \frac{1}{2}O_2$$

where $V_{(O,\,s)}$ represents an empty position (anion-vacant site) originating from the removal of O^{2-} from the lattice, here represented as an oxygen tetrahedral site (Ce_4O). Charge neutrality is maintained by the reduction of two cerium cations from +4 to +3. These oxygen anion-vacant sites are ready for the incorporation of foreign oxygen molecules. Surface adsorbed carbon monoxide molecules react with this neutral oxygen and are oxidized to carbon dioxide. Finally, the oxide anion vacancy is generated again and be involved in another catalytic reaction cycle (Figure 1.1). Therefore, the extent of cerium reduction and introduction of oxide anion vacancy have the positive effect on the performance of CO oxidation.[2, 11]

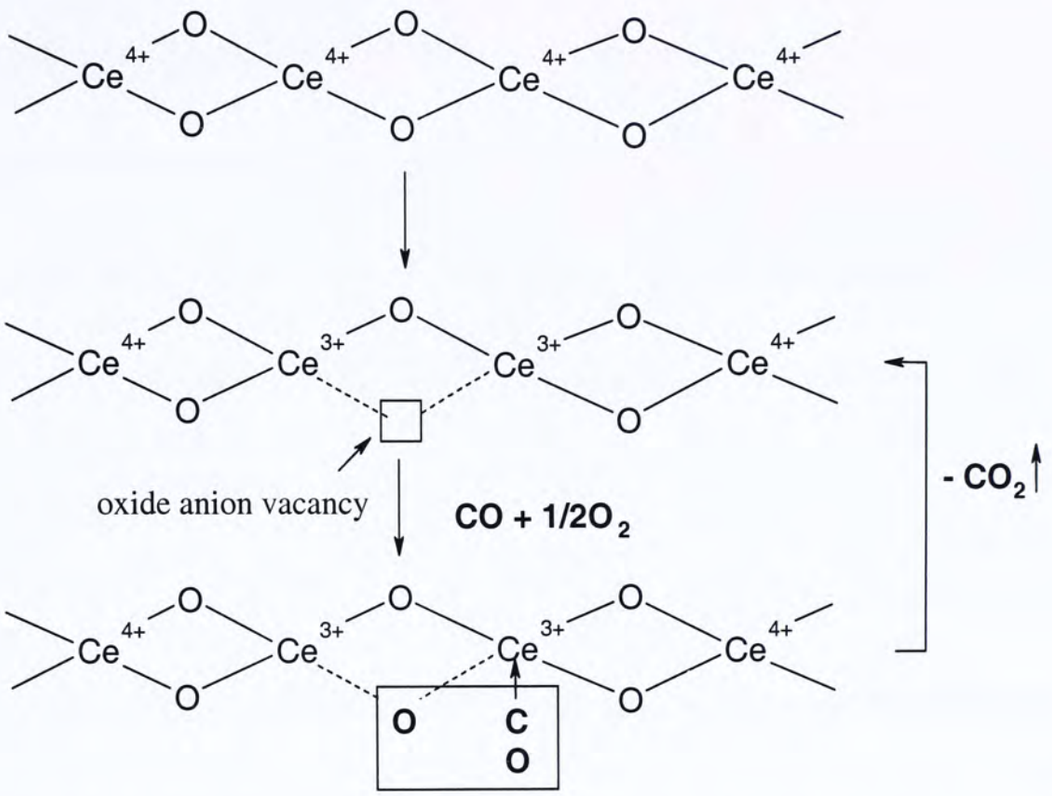

Figure 1.1 Systematic representation of generation of oxide vacancy and CO + $\frac{1}{2}O_2$ reaction over the CeO_2.

The creation of oxide anion vacancy is strongly related to the oxidation state of cerium atom and it can induce structural defects inside the lattice cell. Since the size of Ce(III) is notably larger than Ce(IV) (atomic sizes 1.14 and 0.97 Å, respectively)[12], the presence of Ce(III) cation and oxide anion vacancies increases the size of the unit size.[13] Apart from the creation of oxide anion vacancies, other structural imperfections can also introduce strain in the lattice.[14] It has been suggested that the incorporation of other metal cations (e.g. Ca^{2+}, Zr^{4+}, Pt^{2+}, Pd^{2+}) into a CeO_2 lattice would result in the generation of structural defects that promote the redox actions between Ce(IV) and Ce(III), and thus enhance its catalytic

performance on CO oxidation.[11, 15] Therefore, introduction of structural defects not only promote the generation of oxides-anion vacancies, but also the redox action on the catalyst. Moreover, it is always desirable for catalysts to possess large surface areas and highly porous structures. Methods for the fabrication of such catalysts are discussed in the following sections.

1.3 Synthesis and Modification of Ceria-based Materials

1.3.1 Synthetic Method

Preparation method affects both physical and chemical properties of ceria-based materials such as crystal phase, particle size, surface area, catalytic activities, and oxygen storage capacity (OSC), etc. Therefore, designs of various preparation methods have been carried out to fabricate the ceria-based materials of high catalytic activities, OSC, and thermal durability.[16-18] Many methods have been developed over the last decade including solid-to-solid synthesis (ceramic method, mechanical milling) [16], liquid-to-solid synthesis (precipitation, hydrothermal and solvothermal synthesis, sol-gel method, surfactant-assisted method) [17] and gas-to-solid synthesis (sputtering method, chemical vapor deposition).[18] Among these methods, the surfactant assisted methods are the most commonly used.

1.3.2 Mesoporous Structure of CeO_2, $Ce_xZr_{1-x}O_2$

Surfactant assisted method can be used to synthesize various types of materials in different morphology and forms.[19] This method is particularly applicable for the synthesis of high-surface area mesoporous materials for catalytic applications.[20] A high surface area of catalysts is a necessary requisite to facilitate an enhanced gas-solid contact. Moreover, the reduction of CeO_2 is usually limited on the surface, it is believed that a high surface area can further promote the extent of surface Ce(IV) reduction and hence the creation of oxide anion vacancies. Therefore, fabrication of mesoporous structure is currently a hot topic in the development of ceria material.[21]

1.3.3 Doped CeO_2 Materials

The performance of ceria as automotive catalysts can be enhanced by doping with a second metal (Zr, Pt, Pd, Cu, Ag and Au)[11, 22] Doping often enhances the thermal stability of the support system or favors the transport of oxygen. In some cases, the doped ceria become very active catalysts for reaction such as CO oxidation,[22e] water-gas-shift reaction.[23] Substitution of cerium by other metal cations leads to the creation of oxide anion vacancies. This improves the mobility of oxygen in the bulk, making CeO_2 an effective oxygen storage material in automotive applications.

The CeO_2-ZrO_2 system is one of the most studied mixed-metal oxides. Ceria belongs to the fluorite structure, and each O^{2-} anion is surrounded by a tetrahedron of Ce^{4+} cations located at the center of a cubic arrangement of equivant O^{2-} atom.[2] Insertion of smaller zirconium cation into ceria lattice leads to structural modification of the fluorite lattice and oxide anion vacancy creation.[24] The resulting structural distortions facilitate high oxygen storage capacity, thermal stability and resistant to sintering. Low-valent and small cations appear as the most effective ones in stabilizing ceria because oxide anion vacancies are created, which effectively decrease the number of oxygen atoms in the lattices, and releasing the steric hindrance due to an overcrowded coordination lattice.[25]

1.3.4 Fabrication of Ceria and Cerium-based Nanoparticles

Apart from the increase the surface area of ceria catalyst and doping other element inside ceria lattice, nanostructuring the materials also seem to be an attractive method for the chemical modification of ceria material. Yan *et al.* reported that mesoporous $Ce_{0.2}Zr_{0.8}O_2$ nanosized particles synthesized by the hydrothermal method showed a blue-shift in UV absorption and high CO conversion activity.[26] Chiang *et al.* demonstrated a four order of magnitude increase in electronic conductivity in CeO_2 nanocrystals compared to micrometer-sized coarse grain.[27]

The rate of CO oxidation on gold deposited on nanocryatalline particles of cerium dioxide was found to be a hundred times higher than that of Au on regular CeO_2 support.[28] Nanosized metal oxide particles exhibit unique chemical properties because of their limited size and a high density of corner or edge surface sites.[29] The variation of CeO_2 lattice parameters with particle size is attributed to the generation of defects in the nanocrystalline materials. Favorable formation of reduced Ce(III) species occurs as the particle size decreases below 15 nm. Lattice relaxations have been observed in different nanocrystalline materials.[29b]

1.4 Scope of work

Preparation of porous and nanostructured ceria seems to be an attractive method to develop the new generation of TWC. Most of the studies pay attention on either mesoporous or macroporous structural design of ceria or cerium-containing binary metal oxide.[19-21, 30] There is no report focus on the preparation of the hierarchically porous structure on ceria system. Therefore, development of hierarchically mesostructured porous binary ceria-zirconia oxide with ordered macrochannel is a promising approach for the next generation of ceria-based catalyst. Herein, the first part of the thesis is focused on the synthesis and characterization of a thermally stable, hierarchically-ordered, macro-mesostructured, palladium-loaded ceria-

zirconia catalyst by using a combination of surfactant and colloidal crystal templating methods.

These hierarchically mesoporous macroporous networks in the sample can be preserved even at a high cerium content of 60% and after calcination at 800°C. Macro-mesostructured samples possess large BET surface area and pore volume, and favor surface Ce(IV) reduction and oxide anion vacancy formation. Samples prepared from this templating method show higher phase homogeneity than the ones obtained from the traditional co-precipitation method. These samples exhibit superior performance on carbon monoxide oxidation. This can be explained by its large surface area, porous texture, better chemical homogeneity, high oxide anion vacancy and structural defects.

Nanostructuring the materials also seem to be alternative method in designing catalysts and catalyst promoters for specific catalytic reactions.[31] The development of preparation methods to control the morphology of CeO_2 is needed for tapping the full potential of CeO_2.[32] In the second part, CeO_2 nanoparticles with different morphologies were synthesized via simple solution route. The physical (band gap energies) and chemical properties (carbon monoxide oxidation) of these samples

were characterized. The band gap energies of these CeO_2 nanomaterials are in the order of microrods > nanospheres > spindle-like particles. The higher catalytic activity on CO conversion in spindle-like particles can be explained by the extent of Ce(IV) reduction and the oxide anion vacancies.

1.5 Reference:

(1) (a) J. Kaspar, P. Fornasiero, *J. Solid State Chem.*, **2003**, *171*, 19. (b) X. M. Song, A. Sayari, *Catal. Rev. Sci. Eng.*, **1996**, *38*, 329. (c) A. Trovarelli, *Catal. Rev. Sci. Eng.*, **1996**, *38*, 439.

(2) A. Trovarelli, *Catalysis by Ceria and Related Materials*, Imperial College Press, London, **2002**, pp 1-50.

(3) (a) B. C. H. Steele, *Solid State Ionics*, **2000**, *129*, 95. (b) J. P. Nair, E. Wachtel, I. Lubomirsky, J. Fleig, J. Maier, *Adv. Mater.*, **2003**, *15*, 2077. (c) H. Inaba, H. Tagawa, *Solid State Ionics*, **1996**, *83*, 1.

(4) (a) H. J. Beie, A. Gnoerich, *Sens. Actuators B*, **1991**, *4*, 393. (b) P. Jasinski, T. Suzuki, H. U. Anderson, *Sens. Actuators B*, **2003**, *95*, 73.

(5) J. R. Jurado, *J. Mater. Sci.*, **2003**, *38*, 1133.

(6) C. Piconi, G. Maccauro, *Biomaterials*, **1999**, *20*, 1.

(7) (a) X. Qi, M. Flytzani-Stephanopoulos, *Ind. Eng. Chem. Res.*, **2004**, *43*, 3055. (b) G. Jacobs, L. Williams, U. Graham, D. Sparks, B. H. Davis, *J. Phys. Chem. B*, **2003**, *107*, 10398.

(8) J. R. Gonzalez-Velasco, M. A. Gutierrez-Ortiz, J. L. Marc, J. A. Botas, M. P. Gonzalez-Marcos, G. Blanchard, *Ind. Eng. Chem. Res.*, **2003**, *42*, 311.

(9) R. Si, Y. W. Zhang, S. J. Li, B. X. Lin, C. H. Yan, *J. Phys. Chem. B.*, **2004**, *108*,

12481.

(10) M. Fernandez-Garcia, A. Martinez-Arias, J. C. Hanson, J. A. Rodriguez, *Chem. Rev.* **2004**, *104*, 4063.

(11) (a) K. R. Priolkar, P. Bera, P. R. Sarode, M. S. Hegde, S. Emura, R. Kumashiro, N. P. Lalla, *Chem. Mater.*, **2002**, *14*, 2120. (b) P. Bera, A. Gayen, M. S. Hegde, N. P. Lalla, L. Spadaro, F. Frusteria, F. Arena, *J. Phys. Chem. B*, **2003**, *107*, 6122.

(12) Y. Nagai, T. Yamamoto, T. Tanaka, S. Yoshida, T. Nonaka, T. Okamoto, A. Suda, M. Sugiura, *Catal. Today*, **2002**, *74*, 225.

(13) (a) J. A. Rodriguez, J. C. Hanson, J. Y. Kim, G. Liu, A. Iglesias-Juez, M. Fernandez-Garcia, *J. Phys. Chem. B*, **2003**, *107*, 3535. (b) J. A. Rodriguez, X. Wang, J. C. Hanson, G. Liu, A. Iglesias-Juez, M. Fernandez-Garcia, *J. Phys. Chem. B*, **2003**, *119*, 5659.

(14) M. D. Hernandez-Alonso, A. B. Hungria, J. M. Coronado, A. Martinez-Arias, J. C. Conesa, J. Soria, M. Fernandez-Garcia, *Phys. Chem. Chem. Phys.* **2004**, *6*, 3524.

(15) (a) A. Trovarelli, C. DeLeitenburg, G. Dolcetti, *CHEMTECH*, **1997**, *27*, 32. (b) B. M. Reddy, A. Khan, Y. Yamamda, T. Kobayashi, S. Loridant, J. C. Volta, *Langmuir*, **2003**, *19*, 3025. (c) P. Bera, K. C. Patil, V. Jayaram, G. N.

Subbanna, M. S. Hegde, *J. Catal.*, **2000**, *196*, 293.

(16) (a) T. Tsuzuki, P. G. McCormick, I. W. Chen, *J. Am. Ceram. Soc.*, **2001**, *84*, 1453. (b) J. M. Dean, W. Chun, H. W. Jen, D. A. Benson, R. W. McCabe, G. W. Graham, *Appl. Catal. A*, **2001**, *207*, 379. (c) K. Sato, H. Yugami, T. Hashida, *J. Mater. Sci.*, **2004**, *39*, 5765.

(17) (a) A. Pintar, J. Batista, S. Hocevar, *J. Colloid. Interface Sci.*, **2005**, *285*, 218. (b) F. Bondioli, A. M. Ferrari, L. Lusvarghi, T. Manfredini, S. Nannarone, L. Pasquali, G. Selvaggi, *J. Mater. Chem.*, **2005**, *15*, 1061. (c) C. M. Ho, J. C. Yu, X. Wang, S. Lai, Y. Qiu, *J. Mater. Chem*, **2005**, *15*, 2193. (d) S. Rossignol, F. Gerard, D. Duprez, *J. Mater. Chem.*, **1999**, *9*, 1615.

(18) (a) S. Suh, J. Guan, L. A. Miinea, J. S. M. Lehn, D. M. Hoffman, *Chem. Mater.*, **2004**, *16*, 1667. (b) D. Kim, W. Heui, I. Seong, *Catal. Lett.*, **2004**, *98*, 23.

(19) A. Vantomme, Z.Y. Yuan, G. Du, B. L. Su, *Langmuir*, **2005**, *21*, 1132.

(20) D. Terribile, A. Trovarelli, C. De Leitenburg, G. Dolcetti, J. Llorca, *Chem. Mater.* **1997**, *9*, 2676

(21) (a) T. Brezesinski, C. Erpen, K. Iimura, B. Smarsly, *Chem. Mater.*, **2005**, *17*, 1683. (b) A. K. Sinha, K. Suzuki, *J. Phy. Chem. B*, **2005**, *109*, 1708. (c) D. M. Lyons, K. M. Ryan, M. A. Morris, *J. Mater. Chem.*, **2002**, *12*, 1207. (d) A. S.

Deshpande, N. Pinna, B. Smarsly, M. Antonietti, A. Niederberger, *Small*, **2005**, *1*, 313.

(22) (a) B. A. Riguetto, S. Damyanova, G. Gouliev, C. M. P. Marques, L. Petrov, J. M. C. Bueno, *J. Phys. Chem. B*, **2004**, *108*, 5349. (b) W. Shan, W. Shen, C. Li, *Chem. Mater.*, **2003**, *15*, 4761. (c) P. Bera, K. C. Patil, M. S. Hegde, *Phys. Chem. Chem. Phys.*, **2000**, *2*, 3715. (d) A. M. Venezia, G. Pantaleo, A. Longo, G. Di Carlo, M. P. Casaletto, F. L. Liotta, G. Deganello, *J. Phys. Chem. B*, **2005**, *109*, 2821. (e) S. Carrettin, P. Concepcion, A. Corma, J. M. Lopez Nieto, V. F. Puntes, *Angew. Chem. Int. Ed.*, **2004**, *43*, 2538.

(23) (a) A. Goguet, F. C. Meunier, D. Tibiletti, J. P. Breen, R. Burch, *J. Phys. Chem. B,* **2004**, *108*, 20240. (b) X. Qi, M. Flytzani-Stephanopoulos, *Ind. Eng. Chem. Res.*, **2004**, *43*, 3055.

(24) (a) E. Mamontov, T. Egami, R. Brezny, M. Koranne, S. Tyagi, *J. Phys. Chem. B*, **2000**, *104*, 11110. (b) P. Fornasiero, R. Di Monte, G. Ranga Rao, J. Kaspar, S. Meriani, A. Trovarelli, M. Graziani, *J. Catal.*, **1995**, *151*, 168.

(25) P. Li, I. W. Chen, J. E. Penner-Hahn, *J. Am. Ceram. Soc.*, **1994**, *77*, 1281.

(26) (a) R. Si, Y. W. Zhang, C. X. Xiao, S. J. Li, B. X. Lin, Y. Kou, C. H. Yan, *Phys. Chem. Chem. Phys.,* **2004**, *6*, 1056. (b) Y. W. Zhang, R. Si, C. S. Liao, C. H. Yan, C. X. Xiao, Y. Kou, *J. Phys. Chem. B*, **2003**, *107*, 10159.

(27) Y. M. Chiang, E. B. Lavik, I. Kosacki, H. L. Tuller, J. Y. Ying, *Appl. Phys. Lett.* **1996**, *69*, 185.

(28) S. Carrettin, P. Concepcion, A. Corma, J. M. Lopez Nieto, V. F. Puntes, *Angew. Chem. Int. Ed.* **2004**, *43*, 2538.

(29) (a) M. Fernandez-Garcia, A. Martinez-Arias, J. C. Hanson, J. A. Rodriguez, *Chem. Rev.*, **2004**, *104*, 4063. (b) R. Di Monte, J. Kaspar, *J. Mater. Chem.*, **2005**, *15*, 633.

(30) (a) Q. Z. Wu, Y. Shen, J. F. Liao, Y. G. Li, *Mater. Lett.*, **2004**, *58*, 2688. (b) D. Gulkova, Z. Vit, *Appl. Cat. A*, **1995**, *125*, 61.

(31) C. Burda, X. Chen, R. Narayanan, M. A. El-Sayed, Chem. Rev., **2005**, *105*, 1025.

(32) (a) Z. L. Wang, X. Feng, *J. Phys. Chem. B*, **2003**, *107*, 13563. (b) M. Yada, S. Sakai, T. Torikai, T. Watari, S. Furuta, H. Katsuki, *Adv. Mater.* **2004**, *16*, 1222. (c) C. Sun, H. Li, Z. X. Wang, Li, Chen, X. Huang, *Chem. Lett.* **2004**, *33*, 662. (d) G. S. Wu, T. Xie, X. Y. Yuan, B. C. Cheng, L. D. Zhang, *Mater. Res. Bull.* **2004**, *39*, 1023.

Chapter Two

Meso- and Macro-porous $Pd/Ce_xZr_{1-x}O_2$ as Carbon Monoxide Oxidation Catalysts

2.1 Introduction

The synthesis of ceria and ceria-containing materials is of considerable interest for applications as diverse as catalysts for treating car exhaust, substances for glass polishing, ultraviolet absorbers, luminous materials, solid oxide fuel cells and ceramics.[1] Binary metal oxides of ceria and zirconia are particularly interesting due to their unique redox properties, high oxygen storing/releasing capacity and high thermal stability. These materials are naturally the latest generation of automotive exhaust three-way catalysts.[2] Many preparation methods, such as co-precipitation, sol-gel, sonochemical, high energy ball milling, hydrothermal synthesis and solution-combustion method,[3] have been developed. Controlling the porosity of these catalysts is highly desirable, and it was noted that the physical properties and structural texture are strongly dependent on the preparation procedure. Since the discovery of the silica-based mesophases, MCM-41 [4] and FSM-16,[5] highly-ordered mesoporous ceria and mesoporous ceria-zirconia materials have also

been synthesized by surfactant-assisted and templating methods.[6] Highly-ordered mesoporous ceria-zirconia thin films were also reported in 2003.[7] Hierarchically mesoporous-macroporous materials of alumina, titania, silica, zirconia, aluminosilicate have been synthesized recently.[8] However, these mesoporous-macroporous frameworks are unstable at temperatures higher than 500°C. The fabrication of thermally stable hierarchically-ordered porous materials has recently attracted considerable attention because of their attractive functions for catalysis. Herein, we report the synthesis of a thermally stable, hierarchically-ordered, macro-mesostructured, palladium-loaded ceria zirconia catalyst by using a combination of surfactant and colloidal crystal templating methods.

Yan *et al.* reported that mesoporous $Ce_{0.2}Zr_{0.8}O_2$ nanosized particles synthesized by the hydrothermal method showed a blue-shift in UV absorption and high CO conversion activity.[3g] Wang *et al.* also found different CO adsorption behaviors on the catalysts synthesized from two different methods.[9] Furthermore, a better crystal phase homogeneity can be achieved by using the sol-gel method which leads to higher oxygen capacity and thermal stability,[10] as well as superior performance in NO_x sorption capacity.[3b] It should be noted that there are also reports suggesting the irrelevance of CeO_2-ZrO_2 phase homogeneity on the performance of three-way

catalysts.[11] In this study, a surfactant-assisted synthetic method was applied to prepare a high surface area macro-mesostructured ceria-zirconia catalyst. The influence of structural parameters on thermal catalytic performance is also discussed.

2.2 Experimental Section

2.2.1 Sample Preparation - Synthesis of the Catalyst Support.

Chemical reagents including cetyltrimethylammonium bromide (CTAB, Acros), zirconium n-propoxide ($[Zr(OC_3H_7)_4]$, Aldrich), ammonium cerium (IV) nitrate ($[(NH_4)_2Ce(NO_3)_6]$, Acros), palladium chloride ($PdCl_2$, Aldrich), n-propanol and ammonia water were used as received without further purification. A 10 wt.% (0.27 M) micellar solution of CTAB was prepared by dissolving the surfactant in water at room temperature under ultrasound irradiation. A series of macro-mesostructured samples with different cerium contents $Ce_xZr_{1-x}O_2$ (x = 0.2, 0.4, 0.6 and 0.8; denoted as MM20 MM40, MM60, MM80) were prepared from mixing an appropriate ratio of zirconium n-propoxide ($[Zr(OC_3H_7)_4]$) and ammonium cerium (IV) nitrate ($[(NH_4)_2Ce(NO_3)_6]$) in a minimum amount of n-propanol with ultrasound assisted dissolution. After homogenization, the resulting reddish brown solution was slowly added to the surfactant solution under gentle stirring to disperse the droplets, and the

pH of the solution was kept at 11 using ammonia (35%). The obtained mass was further stirred for 30 minutes and then transferred to a teflon-lined autoclave, and heated under static condition at 80°C for 48 h. The product was filtered and dried overnight at 80°C. The dried solid was calcined at 500 to 800°C for 4 h (ramp of 1°C min^{-1}) for the removal of surfactant and for crystallization. The sample without macroporous framework (M60) was also prepared by the same procedures, except with vigorous stirring. [8a]

Stoichiometric amount of $CeCl_3.7H_2O$ and $ZrCl_4$ were dissolved in de-ionized water to give a colorless solution. Then the resulting solution was added dropwise to ammonia (35%). The hydrated precipitates were filtered off and dried at 80°C. Finally, the purple solid was calcined at 700°C.[3b] A series of samples with different cerium contents of 20, 40, 60, and 80% were prepared by this co-precipitation method (samples denoted as CP20, CP40, CP60 and CP80).

2.2.2 Addition of Pd to the Catalyst Support.

A 0.8 wt. % Pd in $Ce_xZr_{1-x}O_2$ was prepared by immersing the catalyst support to an aqueous solution of $PdCl_2$ under reduced pressure and ultrasound irradiation.[12] After drying, the metal loaded catalysts were calcined at 500°C for 4 h.

2.2.3 Characterization.

Powder X-ray diffraction data were recorded by using a Bruker D8 Advance X-ray diffractometer with Cu $K\alpha_1$ irradiation (λ=1.5406 Å) at a scanning rate of 0.01° per second. The crystal size was estimated by applying the Schrerrer equation ($\Phi = K\lambda/\beta\cos\theta$),[13] where Φ is crystal size, λ is the wavelength of the X-ray irradiation (0.154 nm), K is usually taken as 0.89, β is the peak width at half-maximum height after subtraction of the instrumental line broadening using silicon as a standard, and θ is the diffraction angle of the (111) peak of the cubic phase. Scanning electron microscopy (SEM) measurements were carried out on a LEO 1450VP scanning microscope to investigate the morphology and surface roughness of samples.

Transmission electron microscopy (TEM) and high-resolution transmission electron microscopy (HRTEM) images were recorded on a Tecnai 20 FEG microscope. A trace amount of sample was suspended in ethanol solution, followed by sonication for 10 minutes. Carbon-coated copper grids were used as the sample holders. Nitrogen adsorption-desorption isothermals were collected at 77 K using Micromeritics ASAP 2010 equipment (BET and BJH models, respectively, for specific surface area and porosity evaluation). All the samples were degassed at 150°C and 10^{-6} torr for 24 h prior to the measurement. Surface composition was

determined by X-ray photoelectron spectroscopy (XPS) using a PHI Quantum 2000 XPS System with a monochromatic Al Kα source and a charge neutralizer. All the binding energies were referenced to the C 1s peak at 284.8 eV of the surface adventitious carbon.

2.2.4 Carbon Monoxide Oxidation Measurement

$Pd/Ce_{0.6}Zr_{0.4}O_2$ pellets calcined at 700°C for 4 h were selected as the catalysts for CO oxidation. Catalytic tests were carried out in a conventional fixed-bed quartz microreactor (8 mm in outer diameter) between 50 and 140°C with the feeding of 0.2 g of sample diluted with 0.2 g silica gel. The catalysts were activated in a flow of air (80% N_2 and 20% O_2, 50 ml min^{-1}) at 400°C for 2 h, and cooled to desired temperatures. A gas mixture (1% CO, 20% O_2 and 79% N_2) was then introduced into the reactor at a flow rate of 50 ml min^{-1}. The reaction mixtures were analyzed on-line by gas chromatography using a Porapak Q column for the separation of CO and CO_2 and a 5A Molecular Sieve column for the separation of O_2 and N_2. The conversion of CO to CO_2 over the catalysts was measured at various temperatures after 2 h reaction, where the reaction rate became steady. After each measurement, the catalyst was reactivated by heating at 400°C for 2 h under the airflow. T_{50} and

T_{90} are defined as the temperature at which the conversion of CO to CO_2 reached 50 and 90%, respectively.

2.3 Results and Discussion

2.3.1 XRD Analysis.

The XRD spectra for samples with different cerium contents calcined at 500°C are shown in Figure 2.1a. It can be noted that the strong diffraction peak positioned at ca 30° shift to lower 2θ angles when the cerium content is increased from 20 to 80% (Pd-MM20 to Pd-MM80), indicating that the crystal phase of the sample changes from a tetragonal to a cubic structure. When the cerium content in ceria-zirconia solid solution is higher than 50% (Pd-MM60 and Pd-MM80), the lattice structure of the cell is changed from the tetragonal to face-centered cubic. The additional peak at 62° in the sample of Pd-MM20 and Pd-MM40 is corresponding to the (202) peaks for tetragonal $Ce_{0.2}Zr_{0.8}O_2$ and $Ce_{0.4}Zr_{0.6}O_2$. The powder samples Pd-MM60 for 500 to 800°C calcination temperatures are shown in Figure 2.1b. All four samples contain a single phase with cubic structure, and the cerium and zirconium ions are uniformly distributed in the structure. The average crystalline size is in the range of 5.2 to 8.4 nm. With increasing calcination temperature, there is a slight up-shift in the peak position. This indicates the incorporation of more zirconium into the ceria

lattice. The cubic indexation and unit cell parameters are calculated based on the most intense line (111) of the Pd-MM60 pattern.

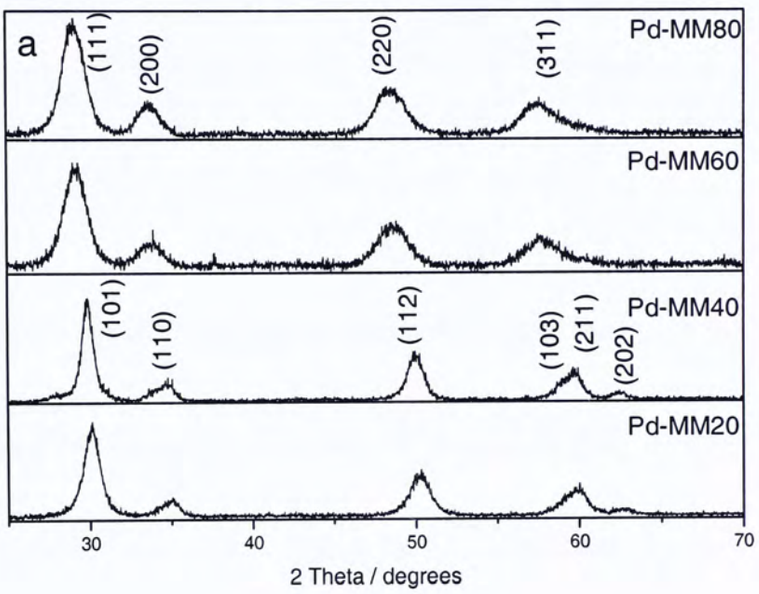

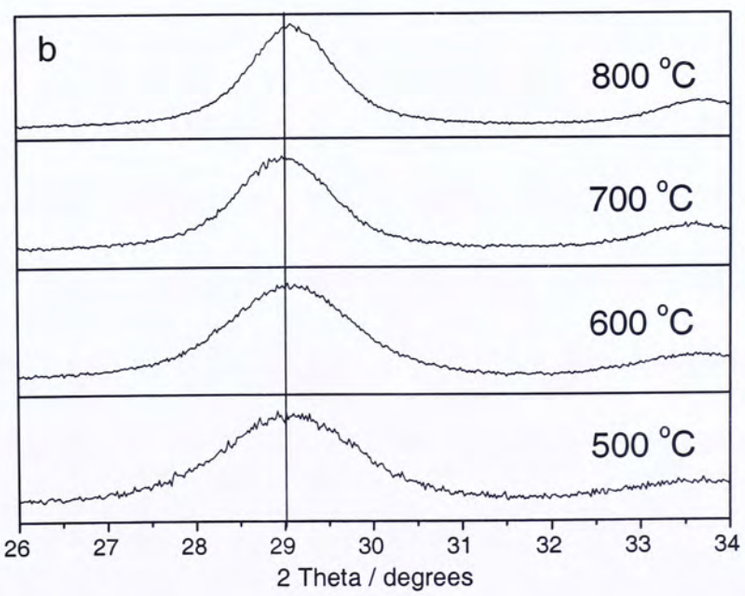

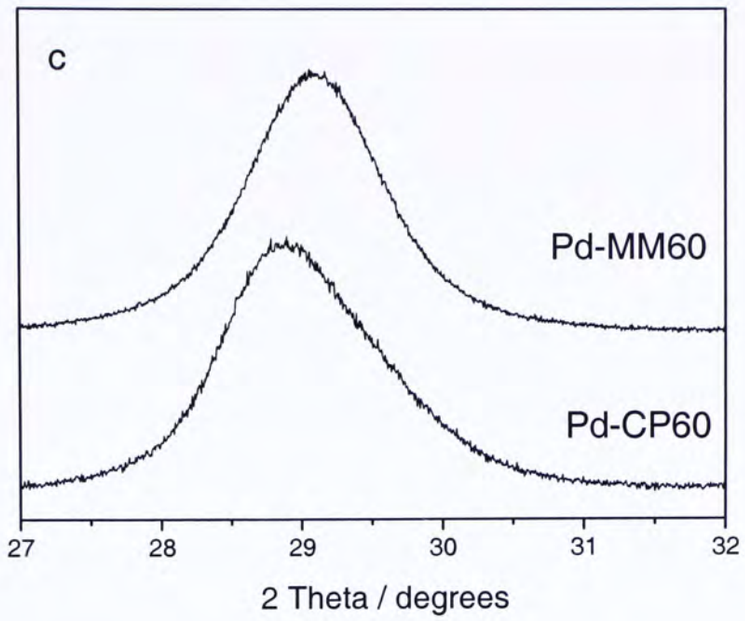

Figure 2.1 (a) XRD spectra for macro-mesostructured samples with different ceria contents: Pd-MM20, Pd-MM40, Pd-MM60 and Pd-MM80. (b) Pd-MM60 calcined at different temperatures. (c) The main (111) diffraction peaks for Pd-CP60 and Pd-MM60 annealed at 700°C.

The change in the cell parameter as a function of calcination temperature is summarized in Table 2.1. The size of the unit cell decreases progressively with increasing calcination temperature, which agrees with Vegard's law.[14] This is primarily due to incorporation of more zirconium into the ceria unit cell (for 8-coordinated M^{4+}, r_{Zr4+} = 0.84 Å, r_{Ce4+} = 0.97 Å). The substitution of smaller zirconium ions into the structure induces a contraction of the lattice cell volume and hence the shortening of the lattice distance. The (111) XRD diffraction peaks for the reference materials Pd-CP60 and Pd-MM60 annealed at 700°C are shown in Figure 2.1c. The asymmetric diffraction peak of Pd-CP60 reveals the presence of both tetragonal ZrO_2 and cubic CeO_2 [ZrO_2: JCPDS 24-1164, $2\theta = 29.8^{\circ}$; CeO_2: JCPDS

34-0394, $2\theta = 28.6^{o}$; $Ce_{0.6}Zr_{0.4}O_2$: JCPDS 38-1439, $2\theta = 29.1^{o}$].[3c, 15] The Pd-MM60 sample, on the other hand, gives a symmetrical diffraction peak. Our proposed method allows the production of homogenous and thermally stable $Ce_xZr_{1-x}O_2$ over a wide range of composition.

Table 2.1 Summary of cell parameters for Pd-MM60 annealed at different temperatures.

Sample	Crystallite size / nm	Lattice param (Å)	Cell Volume ($Å^3$)
800°C	8.3(7)	5.31(2)	149.(9)
700°C	7.5(5)	5.31(6)	150.(2)
600°C	5.5(9)	5.31(9)	150.(5)
500°C	5.1(8)	5.32(9)	151.(3)

2.3.2 SEM and TEM.

The hierarchical structure of the 0.8 wt% Pd / $Ce_xZr_{1-x}O_2$ samples are clearly shown in the scanning electron microscopy images. Figure 2.2 shows the morphologies of the particles with different cerium contents annealed at 700°C. The formation of macroporous framework in the sample is not favorable when the material has cerium content over 60%. Therefore, neither macrochannels nor macropores can be observed in Pd-MM80. This may be due to the different hydrolysis rate of

ammonium cerium (IV) nitrate and zirconium alkoxide. Shanks *et al.* stated that formation of a macroporous framework was highly influenced by the hydrolysis and condensation rate of inorganic precursors.[8a] It should be noted that such a macroporous framework is preserved even after sonochemical and thermal treatments. The particle size is in the range of tens to hundreds of micrometers. The irregularly shaped ceria-zirconia grains appear to be fragments of larger particles. As shown in Figure 2.3, the non-interconnected macrochannels are aligned from a smooth and curved particle surface. The channels were typically 20-60 μm in length and 1-2 μm in diameter. The high magnification SEM image reveals that the walls of these macrochannels are built up from the packing of fine particles. The intra-spacing among these particles relates well with the mesopores in the product and hence both macrotextural and mesotextural structures coexist in the system. The short-range ordered aggregation of polygonal holes can also be observed in the TEM images (Figure 2.4).

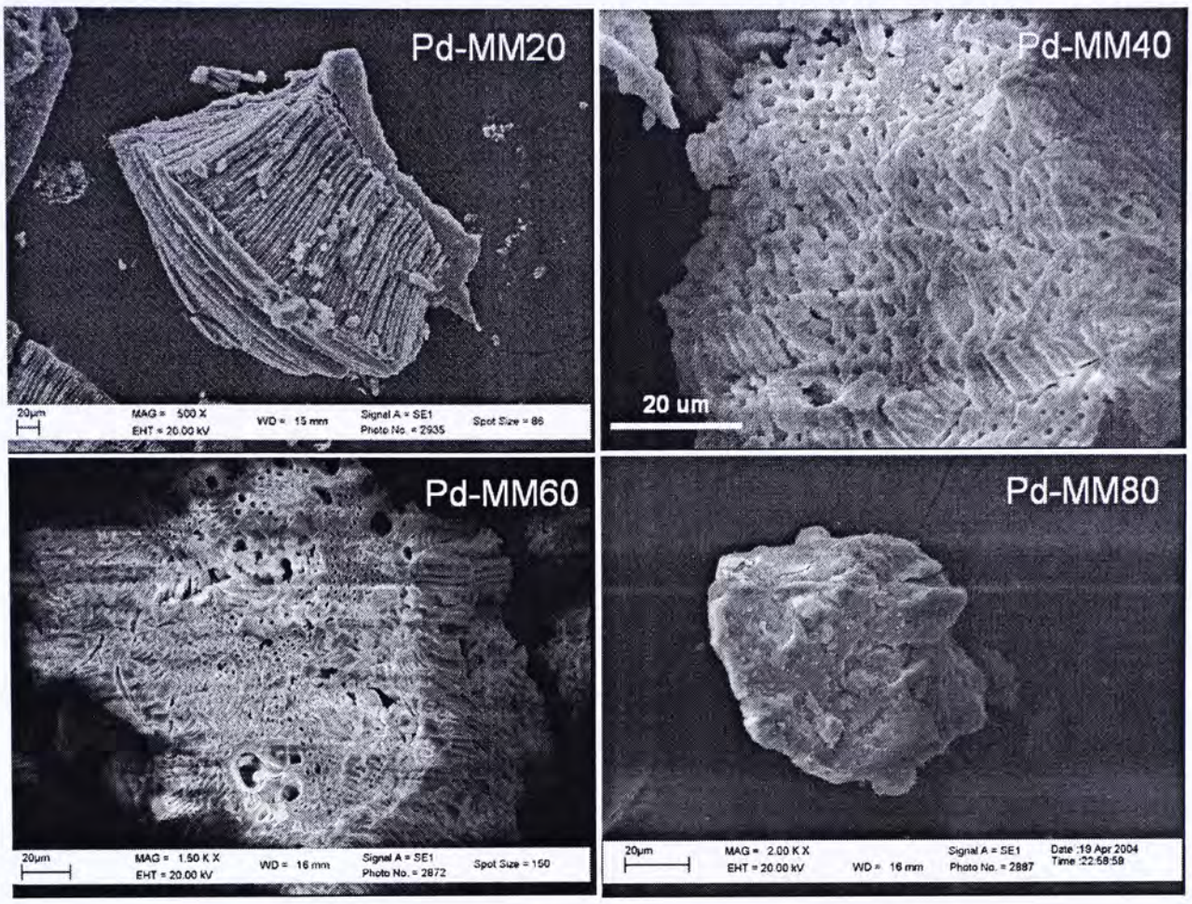

Figure 2.2 SEM images for macro-meso $Pd/Ce_xZr_{1-x}O_2$ (X=0.2 to 0.8) annealed at 700°C.

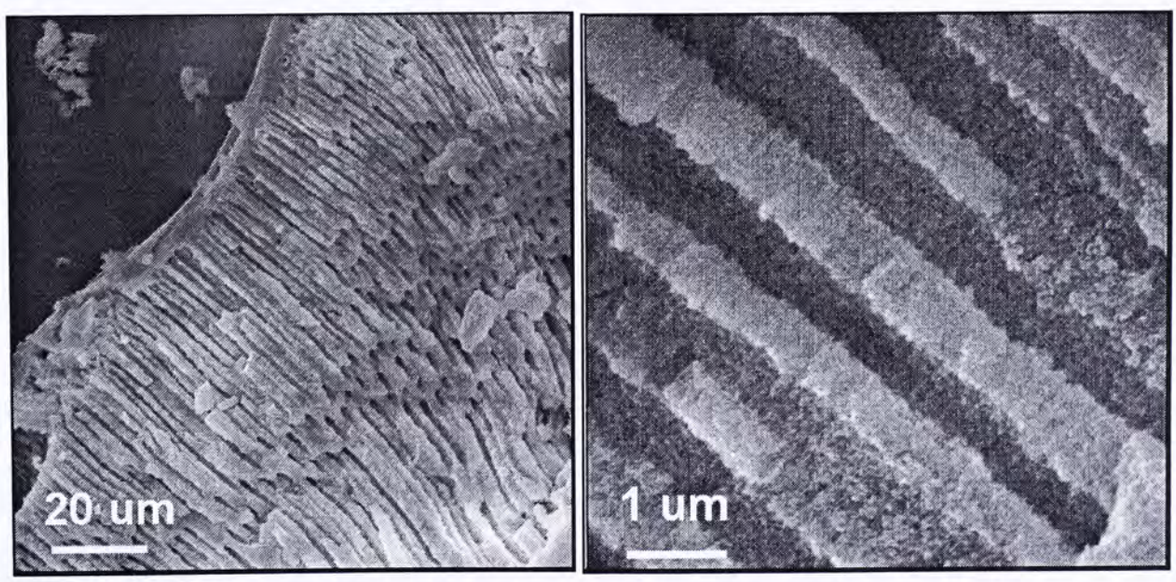

Figure 2.3 SEM images for Pd-MM60 annealed at 800°C.

From the HRTEM micrographs, the (111) facet with an interplanar spacing of about 3.08 Å can be identified from the sample. Crystals are grown in different orientations and they are uniform in size. Figures 2.5a-d show the HRTEM for the sample Pd-MM60 annealed at different temperature. The crystallize size of the samples estimated from HRTEM show the consistency to the size calculated from the Schrerrer equation. From the image, the crystals grow larger and pack more tightly as the calcinations temperature increases.

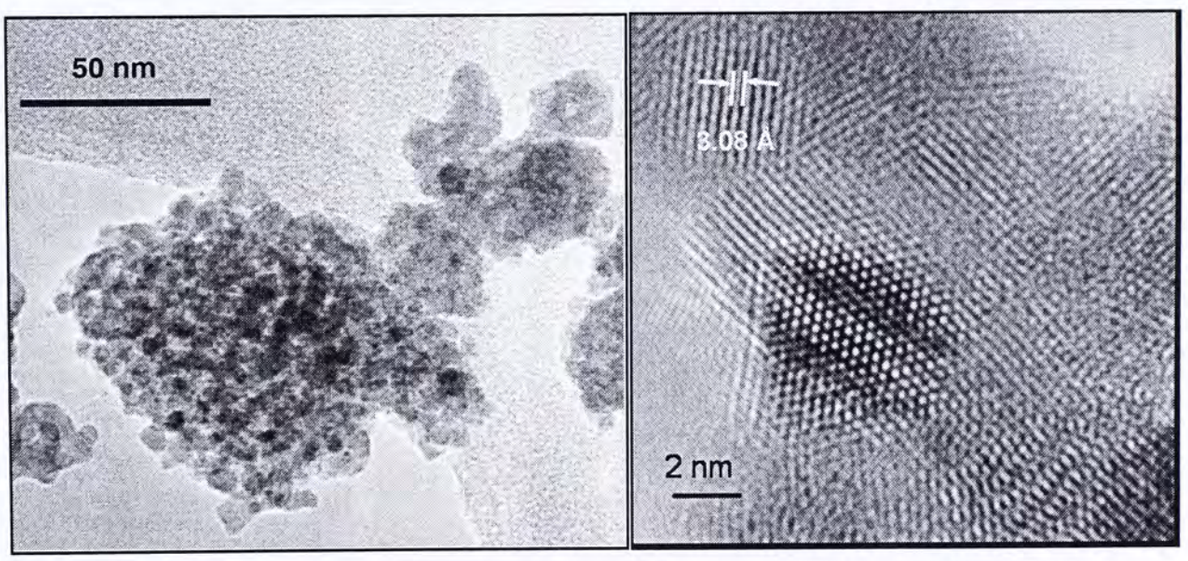

Figure 2.4 TEM images of Pd-MM60 annealed at 700°C with different magnification.

The elemental analysis of the samples were also studied by the EDX spectroscopy, As shown in the EDX spectrum (Figure 2.6, Table 2.2) Pd-MM60 consists of a 3:2 ratio of Ce ion to Zr ion, and 0.82% of Pd, in good agreement with the theoretical

composition. It has been reported that ordered macrochannels could be formed even without the addition of any surfactants.[16] Figures 2.7a-c show the SEM images of catalysts prepared with different amounts of surfactant (0, 2 and 5%). All three samples indeed possess ordered macrochannels. This suggests that the surfactant does not serve as a template for the self-assembling of macropores.

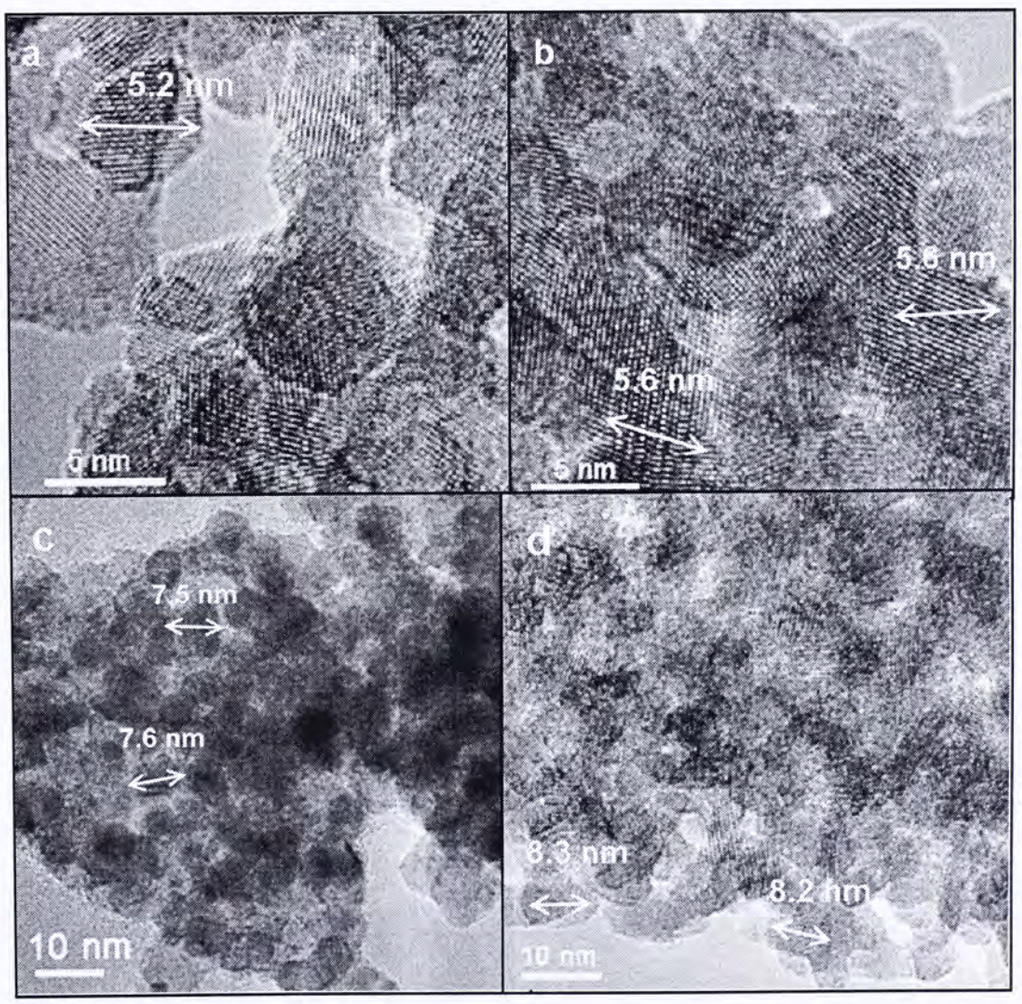

Figure 2.5 HRTEM images of Pd-MM60 annealed at different temperatures a) 500 C, b) 600°C, c) 700°C and d) 800°C.

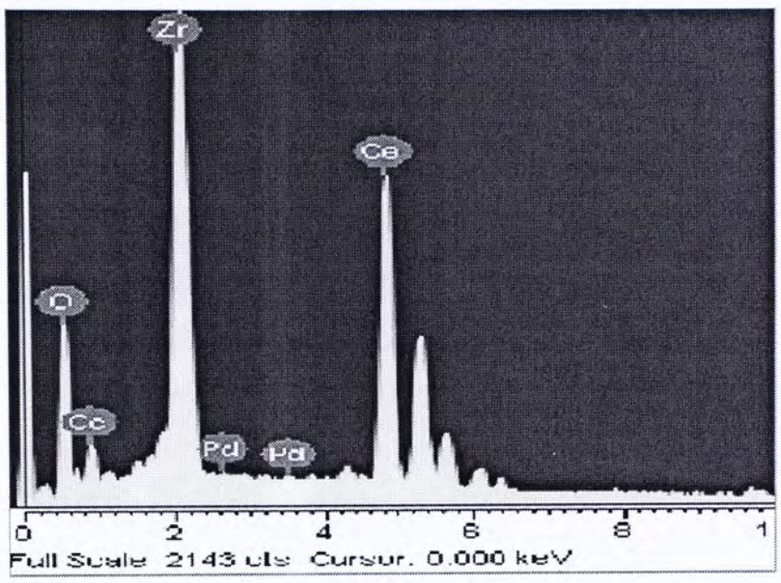

Figure 2.6 EDX spectrum for Pd-MM60

Table 2.2 Summary of results from EDX analysis

Element	Weight %	Atomic %
Ce L	52.14	20.35
Zr L	27.10	14.44
O K	19.94	64.81
Pd L	0.82	0.40

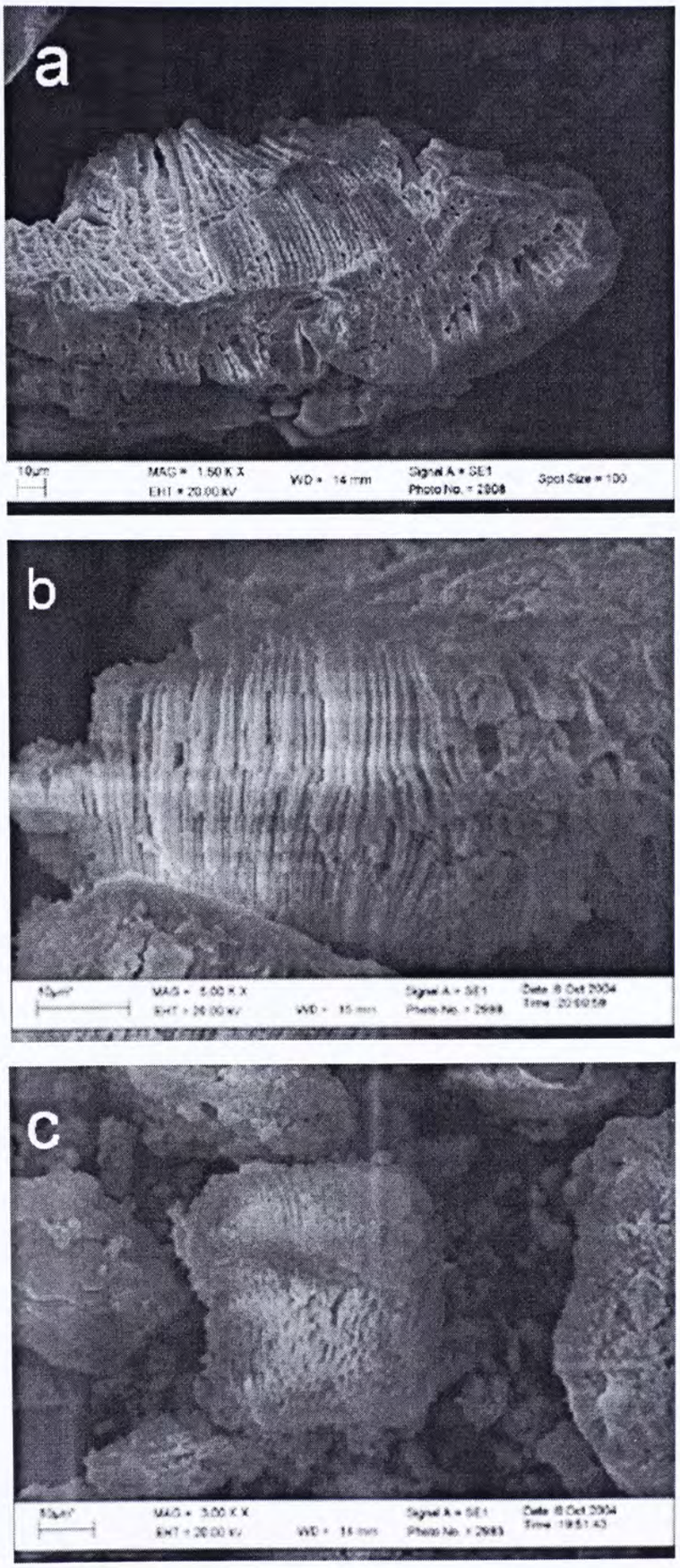

Figure 2.7 SEM images for (a) 0% surfactant/Pd-MM60, (b) 2% surfactant/Pd-MM60 and (c) 5% surfactant/Pd-MM60.

2.3.3 N_2-Soprtion.

Nitrogen adsorption-desorption isotherms and the corresponding Barrett-Joyner-Halenda (BJH) pore size distributions for Pd-MM60 annealed at different temperatures are shown in Figure 2.8. With an increase in the calcination temperature, the surface area of these mesoporous materials gradually decreases while the pore diameter increases, as listed in Table 2.3. For the sample annealed at 500°C, the surface area and pore volume are 131.4 m^2/g and 0.14 m^3/g, respectively. Meanwhile, the pore-size distribution curves for these samples exhibit a mean pore diameter of 4.2 nm. After 800°C calcinations, the mean pore size of the sample increases to 10.1 nm. This is possibly due to the sintering effect, but the mesoporosity of the sample is still preserved.

a. 500°C

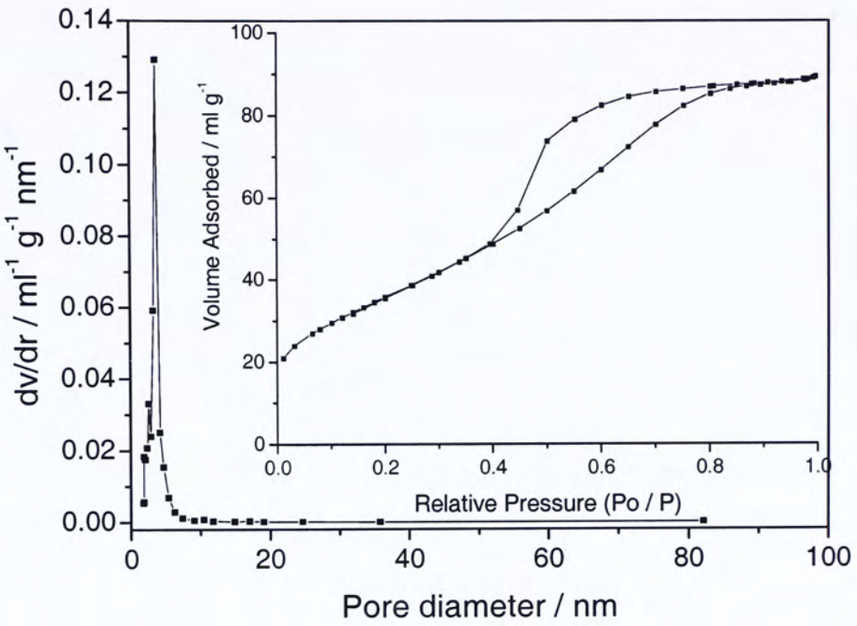
dv/dr / ml^{-1} g^{-1} nm^{-1}
Pore diameter / nm
Volume Adsorbed / ml g^{-1}
Relative Pressure (Po / P)

b. 600°C

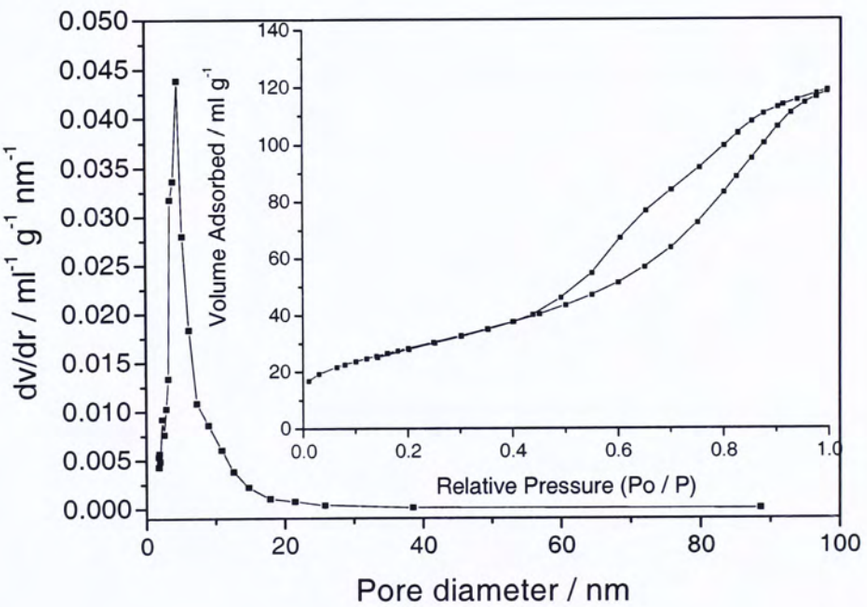
dv/dr / ml^{-1} g^{-1} nm^{-1}
Pore diameter / nm
Volume Adsorbed / ml g^{-1}
Relative Pressure (Po / P)

c. 700°C

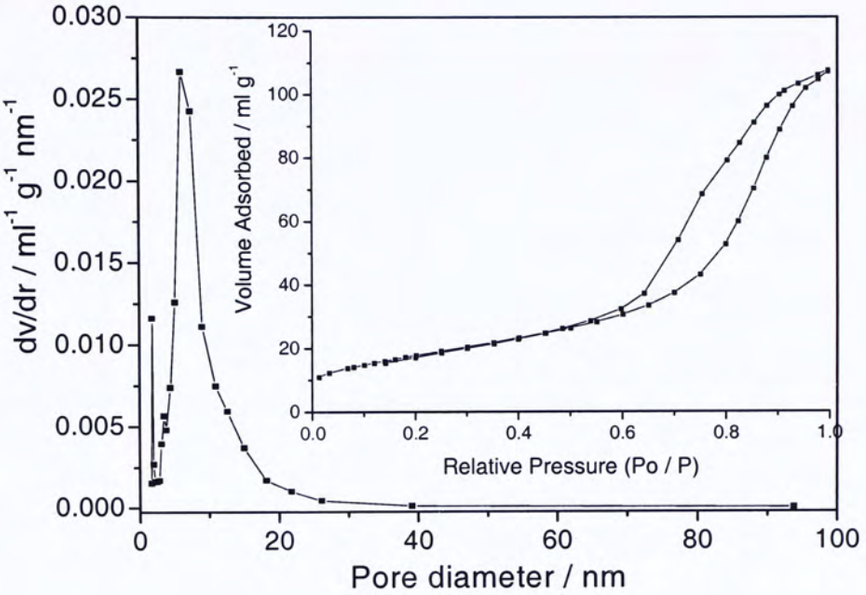

d. 800°C

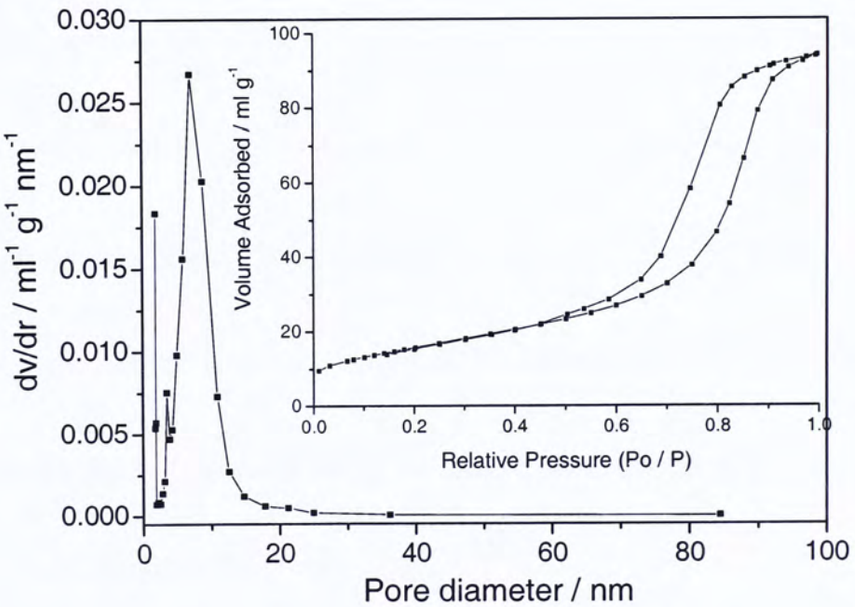

Figure 2.8 Nitrogen adsorption-desorption isotherms and BJH pore size distribution for Pd-MM60 calcined at 500, 600 700 and 800°C.

Table 2.3 Physicochemical properties of the Pd-MM60 annealed at different temperatures.

Sample (Pd-MM60)	S_{BET}[a] (m^2/g)	V[b]/ (cm^3/g)	D_{BJH}[c]/ (nm)
500°C	131.4	0.14	4.2
600°C	103.1	0.18	7.0
700°C	69.5	0.16	10.0
800°C	57.2	0.14	10.1
Pd-CP60 (700°C)	20.6	0.05	10.8
Pd-M60 (700°C)	61.8	0.16	9.4

a BET surface area calculated from the linear part of the BET plot (P/P_0 = 0.1–0.2).

b Total pore volume, taken from the volume of N_2 adsorbed at P/P_0 = 0.995.

c Average pore diameter, estimated using the desorption branch of the isotherm and the Barrett–Joyner–Halenda (BJH) formula.

Table 2.4 Physicochemical properties of the Pd-MM*x* annealed at 500°C.

Sample calcined at 500°C	S_{BET}[a] (m^2g^{-1})	V[b]/ (cm^3g^{-1})	D_{BJH}[c]/ (nm)
Pd-MM20	135.2	0.14	5.5
Pd-MM40	128.5	0.13	4.1
Pd-MM60	131.4	0.14	4.2
Pd-MM80	78.8	0.24	17.0

As compared to Pd-CP60, the surface area and pore volume of Pd-MM60 are much higher (Table 2.3). This is reasonable as the presence of surfactants in the structural formation process can greatly increase the surface area and pore volume. Table 2.4 summarizes the N_2 sorption data for all Pd-MM*x* samples calcined at 500°C. Surface area, pore size and pore volume are almost the same for samples Pd-MM20, Pd-MM40 and Pd-MM60 but they are very different for Pd-MM80. This cannot be explained by the absence of macrochannels in Pd-MM80 because the sample Pd-MM60 and its macrochannel-free counterpart Pd-M60 exhibit similar N_2 sorption properties. We believe during the preparation of Pd-MM80, there is simply not enough zirconium alkoxide [$Zr(OPr^i)_4$] for reacting with the cerium precursor in the following reaction:

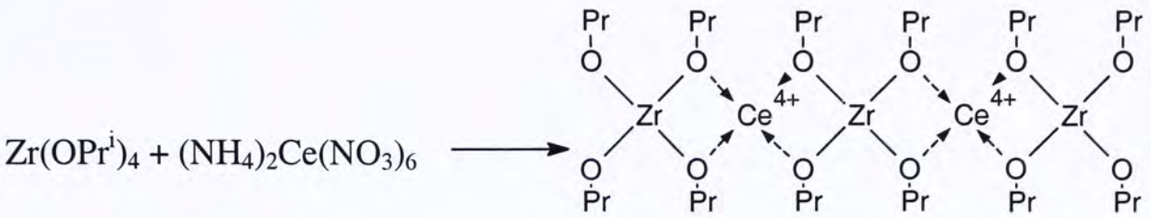

(A)

As a result, very few alkoxide groups are available on the surface of the sample leading to poor network formation in the subsequent steps of hydrolysis and condensation. A high surface coverage of alkoxide groups is known to have a positive effect on the surface area, pore size distribution and particle packing density.[17] In the cerium-rich sample (Pd-MM80), less alkoxide groups on the surface of the samples may cause the decrease in the surface and poor particles packing.

The textural properties of samples prepared with different amounts of surfactant were also studied. The sample prepared with 5% surfactant shows a significantly narrower pore size distribution than that synthesized without or with only 2% surfactant (Figures 2.9). The surface area for the samples (0, 2 and 5% surfactant) is 49.2, 53.4 and 67.8 m^2g^{-1}, respectively. Obviously, the introduction of mesoporous texture in the 5% surfactant/Pd-MM60 sample leads to an increase in its surface area. Mesostructured surfactant/metal oxide compounds are formed by a well-known

neutral surfactant-templating pathway initiated by the reaction between the surfactant micellar solution and the metal-oxide species hydrolyzed from the metal alkoxide precursors.[18] A high concentration of surfactant micellar solution provides sufficient surfactant molecules to be adsorbed onto the hydrophilic solid surfaces, followed by self-assembling at the solid/solution interface. It is the adsorption and self-assembly of surfactant molecules on the external surface of zirconia-ceria/surfactant nanocomposites that form the surface aggregates during the development of internal mesostructures. These primary aggregates can attract more individual surfactant micelles to form supermicelles. Finally these supermicelles should interlink successfully with the surfactant micelles in macrochannels.[8]

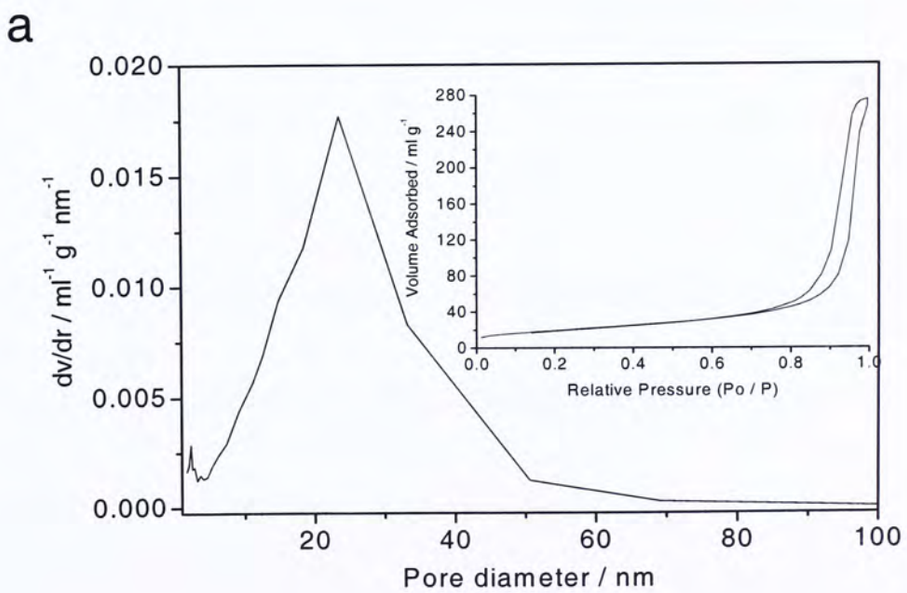

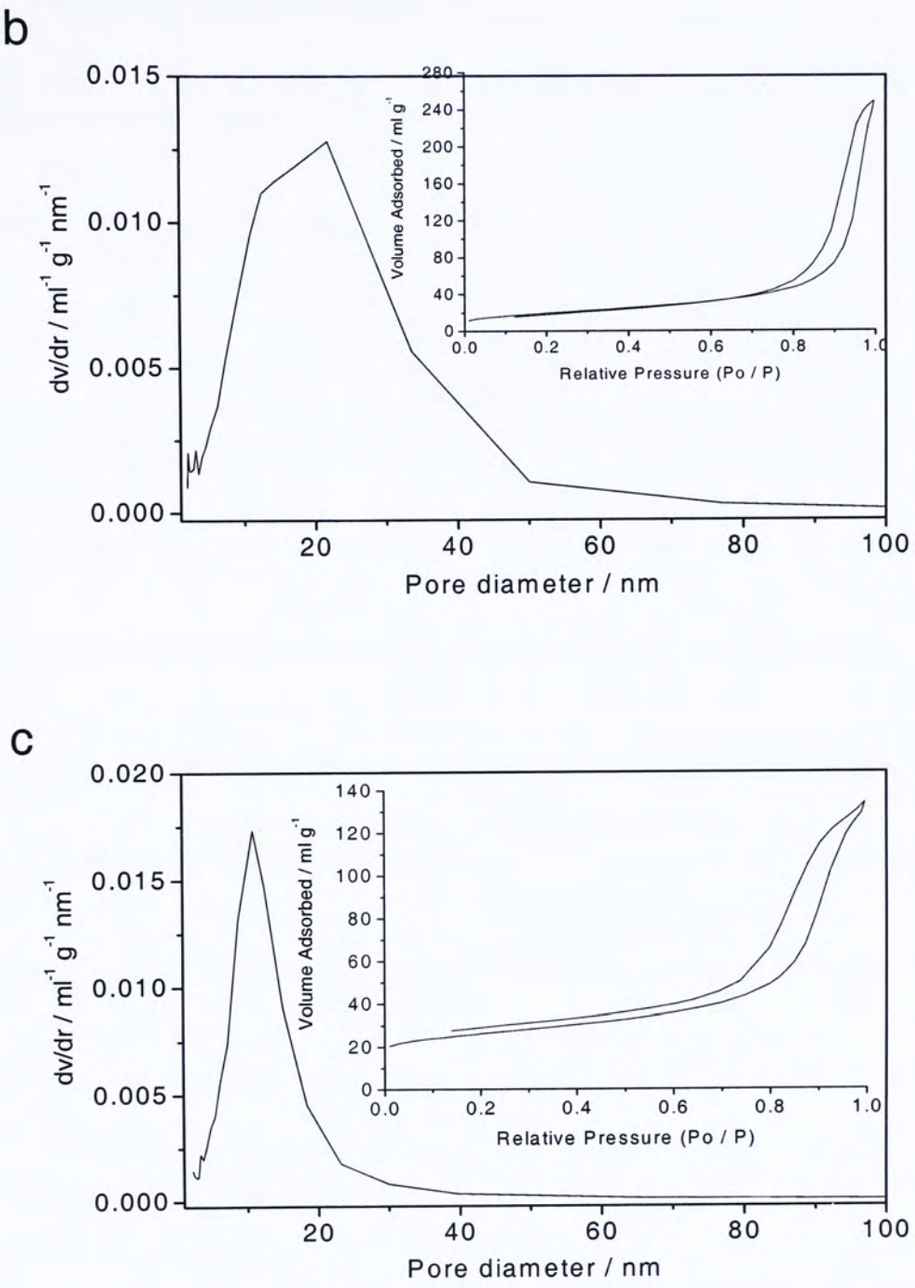

Figure 2.9 Nitrogen adsorption-desorption isotherms and BJH pore size distribution for (a) 0% surfactant/Pd-MM60, (b) 2% surfactant/Pd-MM60 and (c) 5% surfactant/Pd-MM60.

2.3.4 X-ray Photoelectron Spectroscopy.

Figure 2.10a shows a typical XPS survey spectrum of the macro-mesostructured sample. Core levels of Ce 4d, Ce 3d, Zr 3d, Zr 3p, Zr 3s, Pd 3d, C 1s and O 1s can be identified. The atomic ratio of cerium to zirconium is generally consistent with the results from EDX measurements. The Zr 3d level splitting is shown in Figure 2.10b with binding energies in the range of 182.1 – 184.3 eV, in good agreement with values reported in the literature.[19] The overlapping Pd 3d and Zr 3p peaks in Figure 2.10a are well-resolved in the high-resolution spectrum (Figure 2.10c). The four distinct peaks (336.3 and 342.0 eV from Pd, and 332.8 and 346.3 eV from Zr) correspond to the PdO and ZrO_2 species.[20] Shoulder peaks at 338 and 343 eV due to Pd^{2+} are also present. These binding energies closely resemble that of Pd^{2+} in $PdCl_2$.[3h] This suggests that in addition to PdO particles, Pd^{2+} ions are also present in the ceria-zirconia matrix. The absence of diffraction peaks for PdO and $PdCl_2$ in the XRD spectra in the samples illustrates that these species are of particle size smaller than 3 nm and finely dispersed in the matrix.[21]

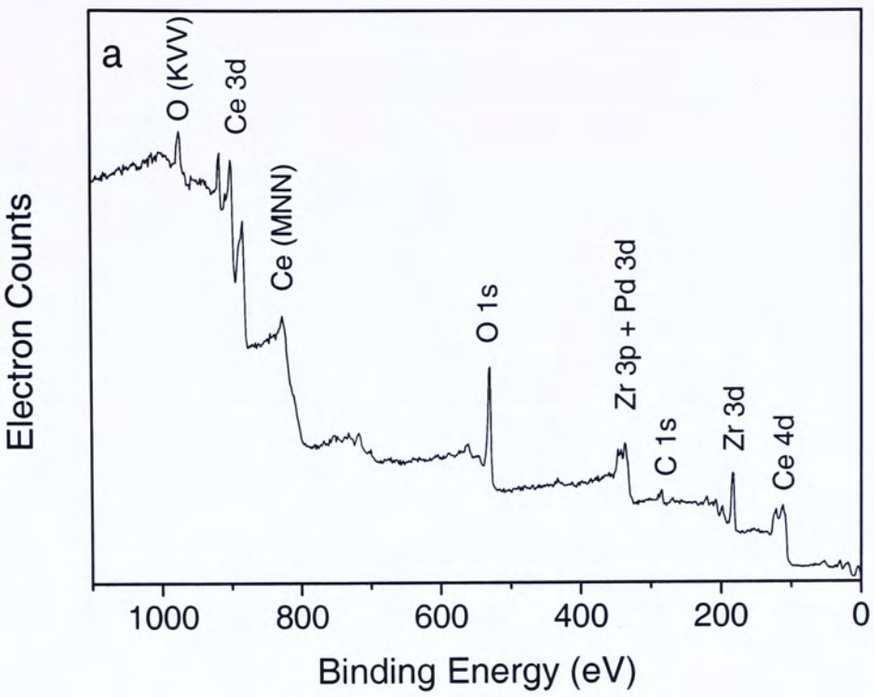
a
O (KVV)
Ce 3d
Ce (MNN)
O 1s
Zr 3p + Pd 3d
C 1s
Zr 3d
Ce 4d
Electron Counts
1000
800
600
400
200
0
Binding Energy (eV)

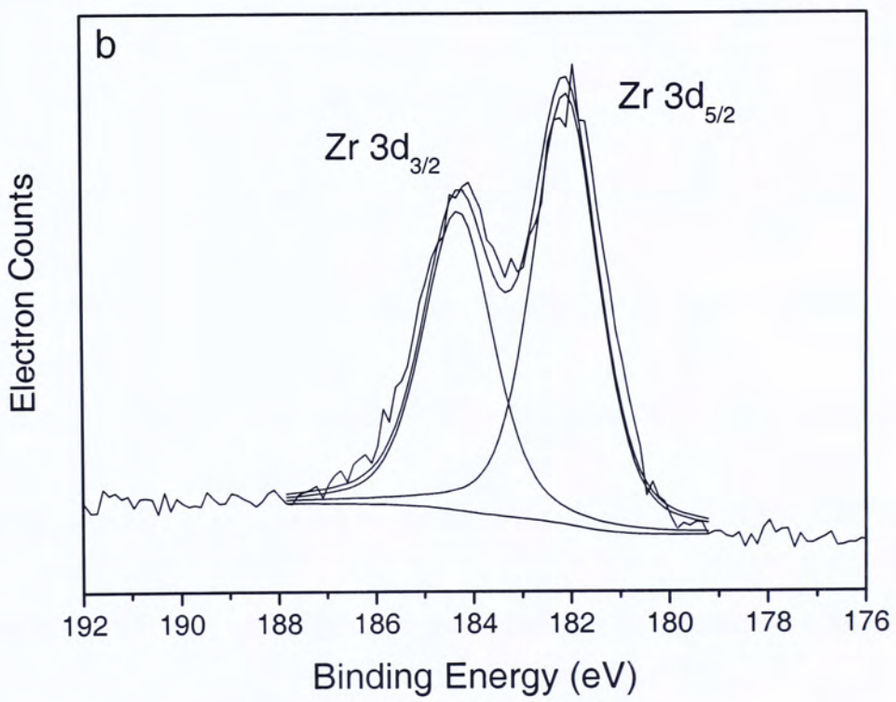
b
Zr 3d5/2
Zr 3d3/2
Electron Counts
192
190
188
186
184
182
180
178
176
Binding Energy (eV)

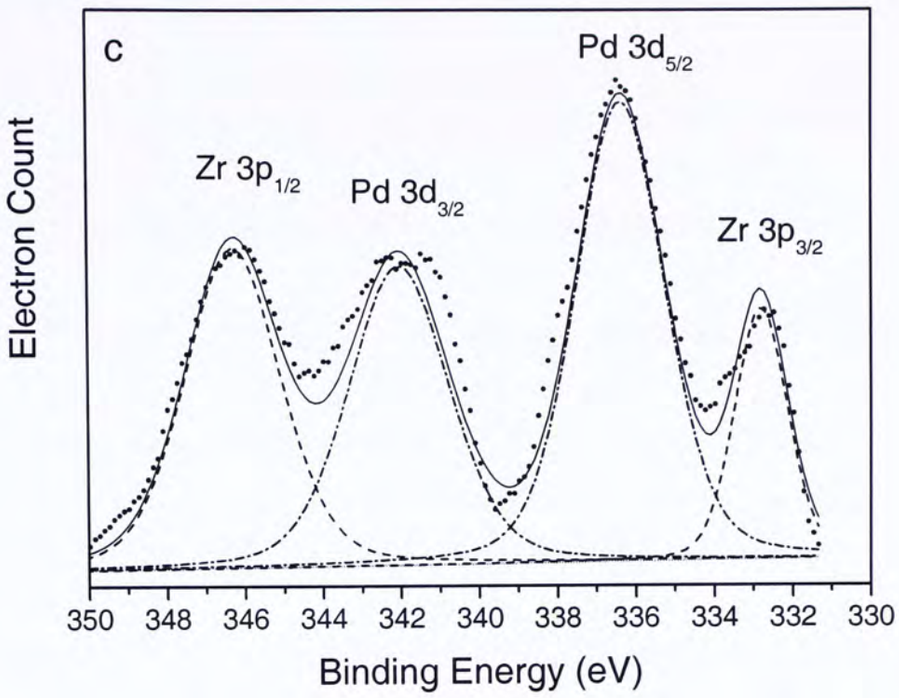

Figure 2.10 (a) Survey (b) Zr 3d and (c) Pd 3d XPS spectra of the Pd-MM60.

The complex XPS spectrum of Ce 3d (Figure 2.11) is formed by the overlap of a series of peaks in the Ce^{4+} and Ce^{3+} states. The spectrum can be deconvoluted into eight Gaussian peaks including the Ce^{4+} $3d_{3/2}$ at 901.3 (u), 907.4 (u_2) and 916.9 (u_3) eV and the $3d_{5/2}$ at 882.7 (v), 889.1 (v_2) and 898.6 (v_3) eV. Specific Ce^{3+} features are also present at 885.6 (v_1) and 903.8 (u_1) eV but the intensities are relatively weak compared to that of Ce^{4+}. The peaks labeled v and v_2 are assigned to a mixing of the Ce $3d^9$ $4f^2$ L^{n-2} and Ce $3d^9$ $4f^1$ L^{n-1} Ce(IV) final states, and the peak denoted v_3 corresponds to the Ce $3d^9$ $4f^0$ L^n Ce(IV) final state. Moreover, lines v_0 and v_1 are assigned to the Ce $3d^9$ $4f^2$ L^{n-1} and Ce $3d^9$ $4f^1$ L^n states of Ce(III). The same assignment can be applied to the u structures, which correspond to the Ce $3d_{3/2}$

levels.[19, 22] Reduction of surface Ce^{4+} to Ce^{3+} by oxygen ion leads to the generation of surface oxide anion vacancy. During the reduction process, the intensity of Ce^{4+} (u_3, v_3) would decrease but that of Ce^{3+} (u_1, v_1) would increase. Based on the relative Ce^{3+} and Ce^{4+} signal intensity, the number of oxide anion vacancies can be estimated by using the following equation:[3g, 23]

$$2Ce^{4+}, 2Zr^{4+}{}_{(s)} + 4O^{2-}{}_{(s)} \rightarrow 2Ce^{3+}, 2Zr^{4+}{}_{(s)} + 3O^{2-}{}_{(s)} + V_{(O,s)} + \frac{1}{2}O_2$$

where $O^{2-}{}_{(s)}$ is the surface oxygen ion and $V_{(O,s)}$ is the surface oxide anion vacancy. The extent of oxide anion vacancy in Pd-CP60 and Pd-MM60 is related to the relative intensity of the Ce^{3+} (u_1 and v_1) peaks. Figure 2.11 shows two Ce 3d core level spectra, showing the influence of the Ce oxidation state on the Ce 3d lineshape. The Pd-MM60 sample has more intense u_1 and v_1 peaks than the Pd-CP60 sample does. This means that the reduction of Ce^{4+} to Ce^{3+} is more favorable on Pd-MM60 and that there are more oxide anion vacancies available on the catalyst surface. The Ce^{3+} ions may also be formed from the reduction of CeO_2 under the ultrahigh-vacuum (10^{-9} torr) conditions in XPS measurements.[24] However, the presence of Ce_2O_3 (Ce^{3+}) could not been observed from XRD measurements. Perrichon *et al.* also demonstrated the positive relationships between the extent of surface Ce^{4+} reduction and sample BET surface area.[25] Moreover, the increase in Ce^{3+} content can also relate to the nanometer particle size prepared from the

presence of surfactant. From the TEM images, Pd-MM60 is formed from the packing of ceria-zirconia nanocrystals. By decreasing the size of the particle, the ratio of surface to bulk atoms increases, which favors conversion of Ce^{4+} to Ce^{3+} near the surface region. This in turn leads to lattice expansion in Pd-MM60 due to the higher ionic radius of Ce^{3+} compared with Ce^{4+}.[3c, 25] Obviously, macro-mesostructured frameworks not only build up the pathway for the gas molecules to penetrate throughout the solid sample during the catalytic reaction, but also provide obstruction-free tunnels for interior cerium ions to undergo reduction. As both surface and bulk cerium ions are involved, the number of oxide anion vacancies would increase.

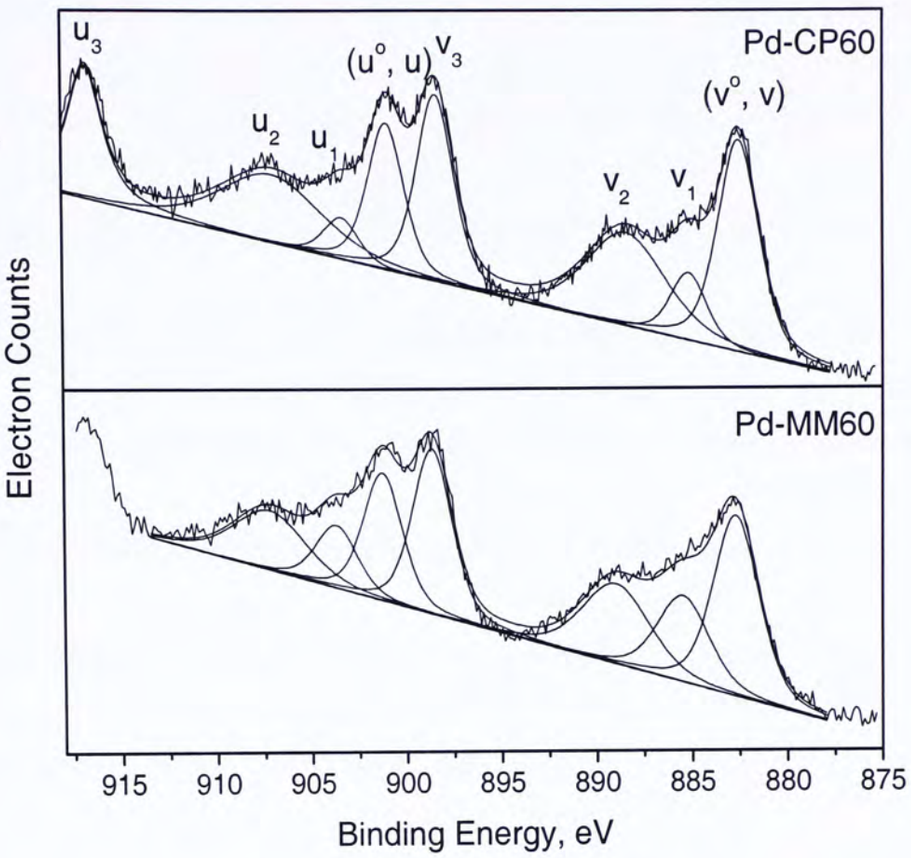

Figure 2.11 Ce3d XPS spectra of the Pd-MM60 and Pd-CP60.

2.3.5 Thermal Catalysis Study.

In order to investigate the relationship between the macroporous framework and its catalytic activity, Pd-MM60 and samples without macrochannels (Pd-M60), prepared with oxide supports calcined at 700°C, were chosen. Moreover, the catalytic activity of a reference material (Pd-CP60) was also included for comparison. Samples were tested for their ability to oxidize carbon monoxide:

$$CO + \frac{1}{2}O_2 \rightarrow CO_2$$

Figure 2.12 shows the catalytic activity profile of CO conversion for Pd-MM60 and Pd-M60. The T_{50} and T_{90} for Pd-MM60 are 65 and 75°C, respectively. These are much lower than the T_{50} and T_{90} for Pd-CP60 and Pd-M60 (without the macroporous network) (Figure 2.13a and b). Tables 2.5 and 2.6 summarize the results of the catalytic activity measurements. The CO conversion rates at 60°C for Pd-MM60, Pd-M60 and Pd-CP60 were 0.534, 0.386 and 0.194 μmol s^{-1} g^{-1}, respectively. Both Pd-MM60 and Pd-M60 possess mesoporous frameworks that provide a large surface to volume ratio, and hence more active sites are available for CO oxidation. The macrochannels in the Pd-MM60 are aligned parallel and perpendicular to the flat dense surface and extended throughout the whole mass (Figure 2.3). These distinct arrays create a barrier-free environment for reactants and products to pass through resulting in the highest CO conversion rate. Since the preparation methods for Pd-MM60 and Pd-M60 were similar, two samples have almost identical chemical structures (crystal phase, lattice cell parameters) and textural properties (surface area and pore size distribution). The variation in CO conversion rate should be mainly due to the presence and absence of a macroporous network. The poor activity of Pd-CP60 can be explained by its structural and chemical properties. When calcined at 700°C, the BET surface area of Pd-CP60 decreases sharply to 20.6 m^2g^{-1} (only 16 % of Pd-MM60). Pd-CP60 annealed at

700°C consists of a mixture of cubic and tetragonal phases, while cubic symmetry is much more favorable for oxygen diffusion. In addition to the inefficient oxygen migration, phase inhomogeneity also strongly inhibits the oxidation-reduction behavior.[27] From the XPS analysis, the extent of surface Ce^{3+} and hence the oxide anion vacancy in Pd-CP60 was indeed lower than that of Pd-MM60. In a cerium-zirconium catalyst, each surface Ce^{4+} ion is coordinated with 4 oxide ions. During calcination, some Pd^{2+} ions are converted to PdO and the rest are incorporated in the zirconia-ceria matrix. When a Pd^{2+} ion substitutes and replaces a Ce^{4+} ion in the lattice, an oxide anion vacancy is generated and a neighboring Ce^{4+} is reduced to maintain the charge balance. The relationship between metal ion substitution and oxide anion vacancy formation has been extensively studied.[3h, 28] These oxide anion vacancies have been suggested as promoting sites for NO and CO conversion.[29] The extent of oxide anion vacancy created is highly dependent on the surface area.[26] The unit cell volume for Pd-CP60 annealed at 700°C was determined to be 151.2 $Å^3$, while it was 150.4 $Å^3$ for Pd-MM60. Fornasiero *et al.* reported that the stress induced by the decrease of unit cell volume would create structural defects and generate oxide anion vacancies. And the structural defects occur preferentially in the pure cubic structure, rather than the mixed phase structure.[27] Figure 2.14 illustrates the function of the PdO nanocrystals.[30] PdO is

deposited mainly on the surface of the catalyst and serves as the catalytic site for the oxidation of carbon monoxide. Underneath the surface is a region where there is a strong interaction between Pd^{2+} and ZrO_2-CeO_2. The reduced ceria sites in the catalyst produce active oxygen species. These oxygen species then react with the adsorbed CO. The high reducibility and oxygen storage capacity of the zirconia-ceria catalyst make this an effective redox system. Consequently, the hierarchically-ordered framework, structural defects and higher oxide anion vacancy account for the high CO conversion activity observed in Pd-MM60.

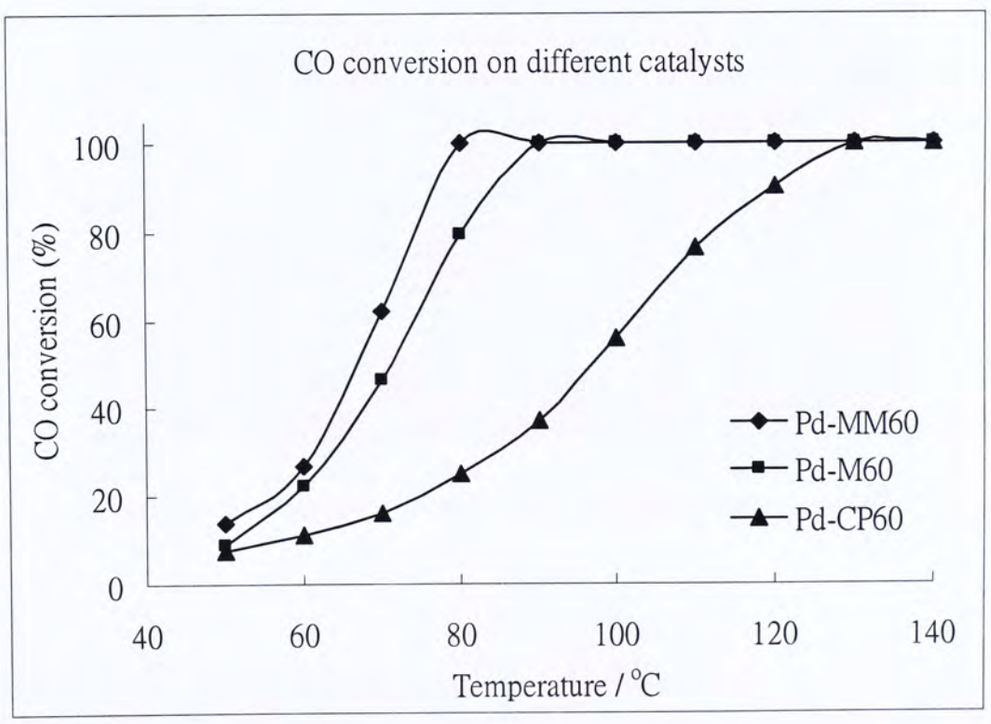

Figure 2.12 Catalytic activity of CO oxidation over the Pd-MM60, Pd-M60 and Pd-CP60.

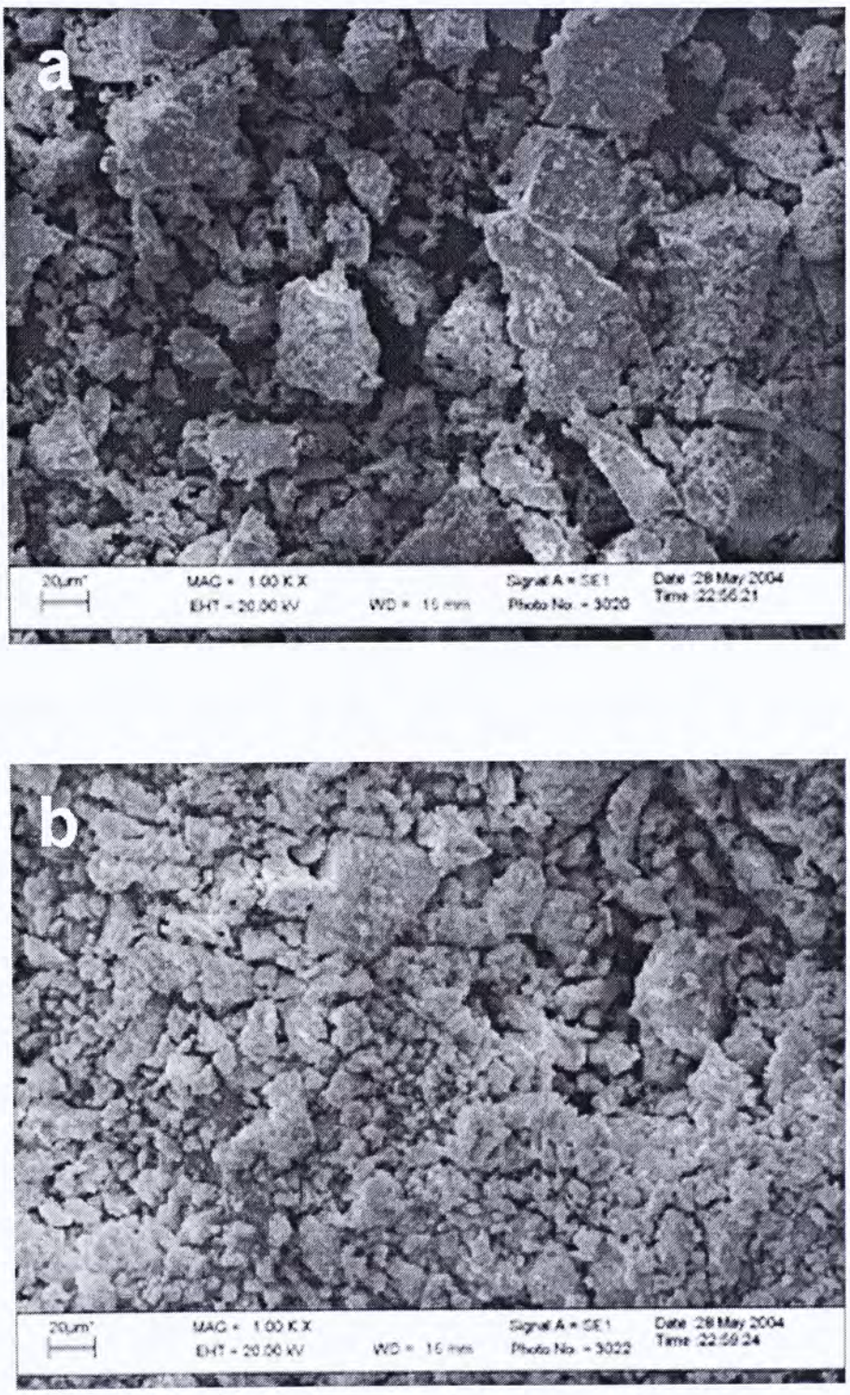

Figure 2.13 SEM images for (a) Pd-CP60 and (b) Pd-M60.

Table 2.5 Comparison of the textural properties, crystal phase and catalytic activities of the samples.

	Pd-MM60	Pd-M60	Pd-CP60 (reference)
CO conversion rate at 60°C / μmol s^{-1} g^{-1}	0.534	0.386	0.194
T50	65°C	70°C	97°C
T90	75°C	85°C	120°C
BET surface area (700°C)	69.5 m^2g^{-1}	61.8 m^2g^{-1}	20.6 m^2g^{-1}
Crystal Lattice Phase	Cubic	Cubic	Cubic + Tetragonal

Table 2.6 Results of the catalytic activity measurements.

Temperature / °C	CO conversion rate / μmol $s^{-1}g^{-1}$		
	Pd-MM60	Pd-M60	Pd-CP60
50	0.241	0.153	0.135
60	0.534	0.386	0.194
70	1.07	0.807	0.283
80	1.73	1.38	0.433
90	1.73	1.73	0.646
100	1.73	1.73	0.971
110	1.73	1.73	1.32
120	1.73	1.73	1.56
130	1.73	1.73	1.73
140	1.73	1.73	1.73

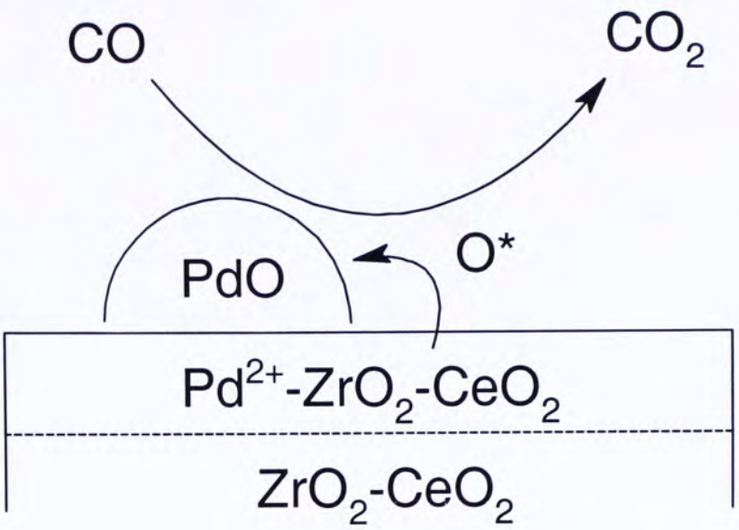

Figure 2.14 Proposed scheme for the role of PdO on CO oxidation.

2.4 Conclusion.

A series of hierarchically macro-mesostructured $Pd/Ce_xZr_{1-x}O_2$ three way catalysts were successfully prepared by using a surfactant-assisted method. These hierarchically mesoporous macroporous networks are preserved even at a high cerium content of 60% and after calcination at 800°C. These frameworks possess large BET surface area and pore volume, and favor surface Ce^{4+} reduction and hence favour oxide anion vacancy formation. Moreover, samples prepared from this method show higher phase homogeneity than the ones obtained from the co-precipitation method. The carbon monoxide conversion rate for Pd-MM60 was much higher than that of Pd-CP60. The superior performance of Pd-MM60 can be

explained by its large surface area, porous texture, better chemical homogeneity, high oxide anion vacancy and structural defects. This thermally stable, catalytically active macro-mesostructured ceria-zirconia catalyst will be very useful as a three-way catalyst.

2.5 References

(1) (a) A. Trovarelli, *Catal. Rev.*, **1996**, *38*, 439. (b) T. Masui, K. Fujiwara, K. Machida, G. Adachi, *Chem. Mater.*, **1997**, *9*, 2197. (c) W. Chengyun, Q. Yitai, X. Yi, W. Changsui, Y. Li, Z. Guiwen, *Mater. Sci. Eng. B.* **1996**, *39*, 160. (d) B. C. H. Steele, *Ceram. Int.*, **1993**, *19*, 269. (e) S. H. Oh, C. C. Eickel, *J. Catal.* **1998**, *112*, 543.

(2) (a) C. Force, J. P. Belzunegui, J. Sarnz, A. Martinez-Arias, J. Soria *J. Catal.* **2000**, *197*, 192. (b) J. Kašpar, P. Fornasiero, M. Graziani, *Catal. Today* **1999**, *50*, 285. (c) J. Kašpar, P. Fornasiero, M. Graziani, *Catal. Today* **2003**, *77*, 419. (d) M. Daturi, C. Binet, J. –C. Lavalley, A. Galtayries, R. Sporken, *Phys. Chem. Chem. Phys.* **1999**, *1*, 5717. (e) B. C. H. Steele, *Nature* **1999**, *400*, 619.

(3) (a) S. Pengpanich, V. Meeyoo, T. Rirksomboon, K. Bunyakiat, *Appl. Catal. A: Gen.*, **2002**, *234*, 221. (b) S. Rossignol, F. Gerard, D. Duprez, *J. Mater. Chem.* **1999**, *9*, 1615. (c) J. Kašpar, P. Fornasiero, G. Balducci, R. Di-Monte, N. Hickey, V. Sergo, *Inorg. Chim. Acta.* **2003**, *349*, 217. (d) J. C. Yu, L. Zhang, J. Lin, *J. Colloid Interf. Sci.*, **2003**, *260*, 240. (e) C. deLeitenburg, A. Trovarelli, F. Zamar, S. Maschio, G. Dolcetti, J. J. Llorca, *Chem. Soc. Chem. Commun.*, **1995**, *21*, 2181. (f) M. Hirano, T. Miwa, M. Inagaki, *J. Am.*

Ceram. Soc. **2001**, *84*, 1728. (g) R. Si, Y. W. Zhang, C. X. Xiao, S. J. Li, B. X. Lin, Y. Kou, C. H. Yan, *Phys. Chem. Chem. Phys.,* **2004**, *6*, 1056. (h) K. R. Priolkar, P. Bera, P. R. Sarode, M. S. Hegde, S. Emura, R. Kumashiro, N. P. Lalla, *Chem. Mater.,* **2002**, *14*, 2120. (i) A. Martinez-Arias, M. Fernandez-Garcia, V. Ballesteros, L. N. Salamanca, J. C. Conesa, C. Otero, J. Soria, *Langmuir* **1999**, *15*, 4796. (j) M. Fernandez-Garcia, A. Martinez-Arias, A. B. Hungria, A. Iglesias-Juez, J. C. Conesa, J. Soria, *Phys. Chem. Chem. Phys.,* **2002**, *4*, 2473. (k) A. Martinez-Arias, M. Fernandez-Garcia, A. B. Hungria, J. C. Conesa, G. Munuera, *J. Phys. Chem. B.*, **2004**, *108*, 17983.

(4) C. T. Kresge, M. E. Leonowicz, W. J. Roth, J. C. Vartuli, J. S. Beck, Nature, **1992**, *359*, 710.

(5) S. Inagaki, Y. Fukushima, K. Kuroda, *J. Chem. Soc. Chem. Commun.*, **1993**, *8*, 680.

(6) (a) D. M. Lyons, K. M. Ryan, M. A. Morris, *J. Mater. Chem.*, **2002**, *12*, 1207. (b) M. P. Kapoor, A. Raj, Y. Matsumura, *Microporous Mesoporous Mater.* **2001**, *44-45*, 565.

(7) E. L. Crepaldi, G. J. de A. A. Soler-Illia, A. Bouchara, D. Grosso, D. Durand, C. Sanchez, *Angew. Chem. Int. Ed.* **2003**, *42*, 347.

(8) (a) W. H. Deng, M. W. Toepke, B. H. Shanks, *Adv. Funct. Mater.*, **2003**, *13*, 61. (b) Z. Y. Yuan, T. Z. Ren, B. L. Su, *Adv. Mater.*, **2003**, *15*, 1462. (c) J. L. Blin, A. Léonard, Z. Y. Yuan, L. Gigot, A. Vantomme, A. K. Cheetham, B. L. Su, *Angew. Chem. Int. Ed.*, **2003**, *42*, 2872. (d) Z. Y. Yuan, A. Vantomme, A. Léonard, B. L. Su, *Chem. Commun.*, **2003**, *13*, 1558. (e) A. Léonard, J. L. Blin, B. L. Su, Chem. Commun., **2003**, *20*, 2568. (f) A. Léonard, B. L. Su, Chem. Commun., **2004**, *14*, 1674.

(9) J. A. Wang, J. M. Dominguez, A. Montoya, S. Castillo, J. Navarrete, M. Moran-Pineda, J. Reyes-Gasga, X. Bokhimi, *Chem. Mater.*, **2002**, *14*, 4676.

(10) (a) J. Kaspar, P. Fornasiero, *J. Solid State Chem.*, **2003**, *171*, 19. (b) R. Si, Y. W. Zhang, S. J. Li, B. X. Lin, C. H. Yan, *J. Phys. Chem. B,* **2004**, *108*, 12481. (c) J. Kaspar, P. Fornasiero, M. Graziani, *Catal. Today,* **1999**, *50*, 285. (d) J. P. Cuif, G. Blanchard, O. Touret, A. Seigneurin, M. Marczi, E. Quémeré, SAE J. (**1996**) paper #961906. (e) Y. Sun, P. A. Sermon, *J. Mater. Chem.* **1996**, *6*, 1025. (f) J. A. Rodriguez, J. C. Hanson, J. Y. Kim, G. Liu, A. Iglesias-Juez, M. Fernandez-Garcia, *J. Phys. Chem. B.*, **2003**, *107*, 3535.

(11) T. Egami, W. Dmowski, R. Brezny, R. SAE J. (**1997**) paper #970461.

(12) J. C. Yu, X. C. Wang, L. Wu, W. K. Ho, L. Z. Zhang, G. T. Zhou, *Adv. Funct. Mater.* **2004**, *14*, 1178.

(13) M. Addamo, V. Augugliaro, A. D. Paola, E. Garcia-Lopez, V. Loddo, G. Marci, R. Molinari, L. Palmisano, M. J. Schiavello, *J. Phys. Chem. B*, **2004**, *108*, 3303.

(14) (a) R. D. Shannon, *Acta Crystallogr.*, 1976, A32, 751. (b) S. Meriani, G. Spinolo, *Powder Diffract.*, **1987**, *2*, 255. (c) B. M. Reddy, A. Khan, Y. Yamada, T. Kobayashi, S. Loridant, J. C. Volta, *Langmuir*, **2003**, *19*, 3025.

(15) P. Vidmar, P. Fornasiero, J. Kašpar, G. Gubitosa, M. Graziani, *J. Catal.*, **1997**, *171*, 160.

(16) A. Collins, D. Carriazo, S. A. Davis, S. Mann, *Chem. Comm.* **2004**, *5*, 568.

(17) (a) C. J. Brinker, G. W. Scherer, *Sol-Gel Science – The Physics and Chemistry of Sol-Gel Processing,* Academic Press, New York, **1990**. (b) A. C. Pierre, *Introduction to Sol-gel Processing*, Kluwer Academic Publishers, Boston, **1998**.

(18) (a) S. A. Bagshaw, E. Prouzet, T. J. Pinnavaia, *Science*, **1995**, *269*, 1242. (b) S. A. Bagshaw, T. J. Pinnavaia, *Angew. Chem. Int. Ed. Engl,* **1996**, *35*, 1102.

(19) A. E. Nelson, K. H. Suhulz, *Appl. Surf. Sci.*, **2003**, *210*, 206.

(20) W. S. Epling, G. B. Hoflund, *J. Catal.,* **1999**, *182*, 5.

(21) H. Zhu, Z. Qin, W. Shan, W. Shen, J. Wang, *J. Catal.*, **2004**, *225*, 267.

(22) (a) A. Pfau, K. D. Schierbaum, *Surf. Sci.*, **1994**, *321*, 71. (b) G. U. Kulkarni, C. N. R. Rao, M. W. Roberts, J. Phys Chem.,**1995**, *99*, 3310. (c) A. Kotani, H. Mizuta, T. Jo, J. C. Parlebas, Solid State Commun., **1985**, *53*, 805. (d) E. Wuilloud, B. Delley, W. D. Schneide, Y. Baer, *Phys. Rev. Lett.,* **1984**, *53*, 202. (e) S. Tsunekawa, T. Fukuda, T.; Kasuya, A. *Surf. Sci.*, **2000**, *457*, L437.

(23) M. Daturi, E. Finocchio, C. Binet, J. C. Lavalley, F. Fally, V. Perrichou, H. Vidal, N. Hickey, J. Kašpar, *J. Phys. Chem. B,* **2000**, *104*, 9186.

(24) (a) P. W. Park, J. S. Ledford, *Langmuir* **1996**, *12*, 1794. (b) E. Paparazzo, G. M. Ingo, N. Zacchetti, *J. Vac. Sci. Technol. A* **1991**, *9*, 1416.

(25) V. Perrichon, A. Laachir, G. Bergeret, R. Frety, L. Tournayan, O. J. Touret, *J. Chem. Soc., Faraday Trans.*, **1994**, *90*, 773.

(26) R. D. Shannon, *Acta Crystallogr.,* 1976, *A32*, 751.

(27) P. Fornasiero, R. Di Monte, G. Ranga Rao, J. Kašpar, S. Meriani, A. Trovarelli, M. Graziani, *J. Catal.*, **1995**, *151*, 168.

(28) (a) P. Bera, K. R. Priolkar, A. Gayen, P. R. Sarode, M. S. Hegde, S. Emura, R. Kumashiro, V. Jayaram, G. N. Subbanna, *Chem. Mater.,* **2003**, *15*, 2049. (b) Parthasarathi. Bera, K. R. Priolkar, P. R. Sarode, M. S. Hegde, S. Emura, R. Kumashiro, N. P. Lalla, *Chem. Mater.* **2002**, *14*, 3591. (c) Arup Gayen, K.

R. Priolkar, P. R. Sarode, V. Jayaram, M. S. Hegde, G. N. Subbanna, S. Emura, *Chem. Mater.,* **2004**, *16*, 2317. (d) A. Trovarelli, C. De Leitenburg, G. Dolcettim, *CHEMTECH*, **1997**, *27*, 32. (e) H. He, H. X. Dai, L. H. Ng, K. W. Wong, C. T. Au, *J. Catal.*, **2002**, *206*, 1.

(29) J. G. Nunan, H. J. Robota, M. J. Cohn, S. A. Bradley, *J. Catal.*, **1992**, *133*, 307.

(30) (a) A. Trovarelli, *Catalysis by Ceria and Related Materials*, Imperial College Press, London, **2002**. (b) H. S. Roh, K. W. Jun, W. S. Dong, S. E. Park, Y. S. Baek, *Catal. Lett.,* **2001**, *74*, 31.

Chapter Three

Morphology-Controllable Synthesis of Mesoporous CeO_2 Nano and Meso-structures

3.1 Introduction

One-dimensional (1D) nanostructures (such as wires, rods, belts, whiskers and tubes) have enormous potential as components of nanodevices and sensors because of their peculiar properties, which originate from their high surface area and low dimensionality.[1] The size and morphology of such semiconductors strongly influence their applications.[2] There are many applications where nanostructured materials could be exploited to greatly enhance the functionality or performance of materials, including applications such as nanoelectronics and nanophotonics. Much effort has been devoted to the synthesis of various nanomaterials using various methods.[3] The ethylene glycol-mediated synthesis is known to be one of the most powerful general methods to prepare uniform 1D nanomaterials.[4] Ethylene glycol has been widely used in the so-called polyol-mediated synthesis of metal nanoparticles because of its physical properties: 1) a high dielectric constants, which enhances the solubility of inorganic salts, 2) a high boiling point (195°C at

atmospheric pressure), which makes it possible to carry out the preparation of inorganic compounds at relatively high temperatures and 3) its strong reducing power.

The morphology controllable synthesis of nanostructured metal compounds including PbSe,[5] ZnO,[6] $In(OH)_3$,[7] SnO_2 [8] and V_2O_5 [9] have been successfully developed CeO_2 possesses many attractive properties which makes it highly promising for a wide range of applications such as solid electrolytes in solid oxide fuel cells,[10] automotive three-way catalysts,[11] ultraviolet absorbers,[12] and oxygen sensors.[13] It is also used as catalyst for large-scale fluid cracking in refineries and dehydrogenation of ethyl benzene to styrene.[14] Nanocrystalline ceria are expected to have superior physical properties. Chiang *et al.* demonstrated a four order of magnitude increase in electronic conductivity in CeO_2 nanocrystals compared to micrometer-sized coarse grain.[15] Due to the quantum size effect, a blue shift in UV absorption spectrum was observed.[16] The rate of CO oxidation on gold deposited on nanocrystalline particles of cerium dioxide was found to be a hundred times higher than that of Au on regular CeO_2 support.[17] The development of preparation methods to control the morphology of CeO_2 is needed for tapping the full potential of CeO_2. Nevertheless, only a few reports have emerged about the fabrication of 1D cerium

compound nanostructures. These include the synthesis of cerium compound nanowires and nanorings templated by NaAOT and alkyl alcohol as well as the formation of cerium dioxide nanowires from a mixture of cerium acetate and NaAOT.[18] In this character, we report for the first time the synthesis of cerium dioxide nanospheres, spindle-like particles and microrods via simple solution route. The morphology can be controlled by simply changing the reaction time and the concentration of the cerium precursor. Moreover, the correlations between the band gap energies, grain size and morphology of the samples have been studied.

3.2 Experimental Section

3.2.1 Materials and Experimental Conditions

Chemical reagents including ammonium cerium (IV) nitrate ($[(NH_4)_2Ce(NO_3)_6]$, Acros), ethylene glycol (EG, Panreac) and poly(vinylpyrrolidone) (PVP M_w 10,000, Aldrich) were used as received without further purification. Table 3.1 shows the appropriate concentrations of ammonium cerium (IV) nitrate ($[(NH_4)_2Ce(NO_3)_6]$, required for the preparation of CeO_2 nanospheres, microrods and spindle-like particles. The cerium precursor was dissolved in 30 ml ethylene glycol containing 0.16 M PVP under vigorous stirring until a homogeneous colorless solution was obtained. The mixture was heated under reflux to the boiling point of ethylene glycol

(*ca* 190°C) for either 4 or 24 h (Table 3.1). The color of the solution changed initially to yellowish brown and a brown gas was evolved during reflux. A white precipitate started to appear after about 2 h and the reaction mixture became milky. At the end of the pre-determined reaction time, the mixture was centrifuged and washed with deionized water and absolute ethanol to remove excess ethylene glycol and PVP. After drying overnight in a vacuum oven at 80°C, the product was calcined at 600°C for 4 h for crystallization.

We also prepared another ceria catalyst support by a co-precipitation method. $(NH_4)_2Ce(NO_3)_6$ was dissolved in de-ionized water to give a clear orange solution. Then the resulting solution was added dropwise to ammonia (35%). The yellow hydrated precipitates were filtered off and dried at 80°C. Finally, the dried product was calcined at 500°C for crystallization.

Table 3.1 Summary of Experimental Conditions.

Morphology	Cerium precursor concentration	Reaction time (h)
Spheres	80 mM	4
Rods	80 mM	24
Spindle-like	40 mM	24

3.2.2 Characterizations

Powder X-ray diffraction data were recorded by using a Bruker D8 Advance X-ray diffractometer with Cu $K\alpha_1$ irradiation (λ=1.5406 Å) at a scanning rate of 0.01° per second. The crystal size was estimated by applying the Schrerrer equation ($\Phi = K\lambda/\beta\cos\theta$), where Φ is crystal size, λ is the wavelength of the X-ray irradiation (0.154 nm), K is usually taken as 0.89, β is the peak width at half-maximum height after subtraction of the instrumental line broadening using silicon as a standard, and θ is the diffraction angle of the (111) peak of the cubic phase.

Scanning electron microscopy (SEM) measurements were carried out on a LEO 1450VP scanning microscope to investigate the morphology and surface roughness of samples. Transmission electron microscopy (TEM) and high-resolution transmission electron microscopy (HRTEM) images were recorded on a Tecnai 20 FEG microscope. A trace amount of sample was suspended in ethanol solution, followed by sonication for 10 minutes. Carbon-coated copper grids were used as the sample holders.

Nitrogen adsorption-desorption isothermals were collected at 77 K using Micromeritics ASAP 2010 equipment (BET and BJH models, respectively, for

specific surface area and porosity evaluation). All the samples were degassed at 150°C and 10^{-6} torr for 24 h prior to the measurement.

Surface composition was determined by X-ray photoelectron spectroscopy (XPS) using a PHI Quantum 2000 XPS System with a monochromatic Al Kα source and a charge neutralizer. All the binding energies were referenced to the C 1s peak at 284.8 eV of the surface adventitious carbon.

The solvent of the reaction mixture was analyzed by gas chromatography-mass spectrometry (GC/MS) to detect the intermediates produced from the reactions between ethylene glycol and $(NH_4)_2Ce(NO_3)_6$. A HP 6890 GC system equipped with a HP-5MS (30 m x 0.25 mm x 0.25 μm, (5%-Phenyl-methylpolysiloxane) column and a HP 5973 Mass Selective Detector was used in the study. Before GC/MS analysis, the sample was centrifuged to remove the particles from the solution. 250μl of the sample and 250μl of chloroform were then transferred into a glass vial and dried in an oven for 5 days at 55°C. The organic residue was diluted in chloroform with addition of 50μl of 100 ppm naphthalene standard with dilution factor of 10. It was then sonicated for 30 min and was transferred to 1.5 ml amber vials with screw caps. 1μl of the sample was manually injected for analysis.

The initial temperature was maintained at 70°C for 3 min; then increased to 160°C at a rate of 80°C min^{-1}, then gradually raised to 250°C at a rate of 2°C min^{-1}. The solvent delay was 3.5 min. The flow rate of helium carrier gas was 1.0 ml min^{-1}. The MS transfer line temperature was set as 280°C. Mass spectra were recorded by standard electron ionization (70 eV) at the EI mode. The total GC run time was 60 min. The MS detector was operated in full scan mode, scanning between m/z 35 and m/z 700 repeatedly during each GC run. Interpretation of mass spectra was supported by literature data and NIST spectra library.

The FT-IR spectra of the solid samples were obtained on a Nicolet FT-IR 560 FT-IR spectrometer. The UV-Vis spectra of the samples were recorded on a Cary 100 a UV-Vis spectrophotometer using a quartz cell (1 cm path length). The calcined CeO_2 nanospheres, microrods and spindle-like particles were each dispersed in ethanol at a concentration of about 10^{-3} mol L^{-1} and then sonicated for 1 h to obtain transparent colloidal solutions. The UV-Vis absorption spectra were recorded using pure ethanol as a blank and spectral grade $BaSO_4$ powder as a reference.

CeO_2 nanospheres, microrods and spindle-like particles were selected as the catalysts for CO oxidation. Catalytic tests were carried out in a conventional

fixed-bed quartz microreactor (8 mm in outer diameter) between 50 and 140°C with the feeding of 0.2 g of sample diluted with 0.2 g silica gel. The catalysts were activated in a flow of air (80% N_2 and 20% O_2, 50 ml min^{-1}) at 400°C for 2 h, and cooled to desired temperatures. A gas mixture (1% CO, 20% O_2 and 79% N_2) was then introduced into the reactor at a flow rate of 50 ml min^{-1}. Reaction mixtures were analyzed on-line by gas chromatography using a Porapak Q column for the separation of CO and CO_2 and a 5A Molecular Sieve column for the separation of O_2 and N_2. The conversion of CO to CO_2 over the catalysts was measured at various temperatures. T_{50} and T_{90} are defined as the temperature at which the conversion of CO to CO_2 reached 50 and 90%, respectively.

3.3 Results and Discussion

3.3.1 SEM and TEM Analysis

Various shapes of CeO_2 nanoparticles were prepared by mixing $(NH_4)_2Ce(NO_3)_6$ and ethylene glycol, by varying the concentration of the cerium precursor and the duration of the reaction. The optimal reaction conditions for the formation of CeO_2 nanospheres, microrods and spindle-like particles are summarized in Table 3.1. The morphology of the obtained CeO_2 nanocrystals was examined by scanning electron microscope (SEM) and transmission electron microscope (TEM). Representative

SEM and TEM micrographs of annealed CeO_2 nanospheres are shown in Figures 3.1a, b and c. These figures reveal monodispersed nanospheres with a relatively uniform diameter of 80 - 100 nm. The electron diffraction (ED) pattern (inset of Figures 3.1b) confirms the polycrystalline nature of the sample and its face-centred cubic crystal structure. These results are consistent with that obtained by XRD (Figure 3.3a). From the ED pattern, it can be concluded that the CeO_2 nanospheres are built up from the aggregation of small crystallites. The energy-dispersive X-ray spectroscopy (EDX) measurements confirm that the nanospheres are composed of Ce and O in the ratio of 1:2 (Figures 3.1d).

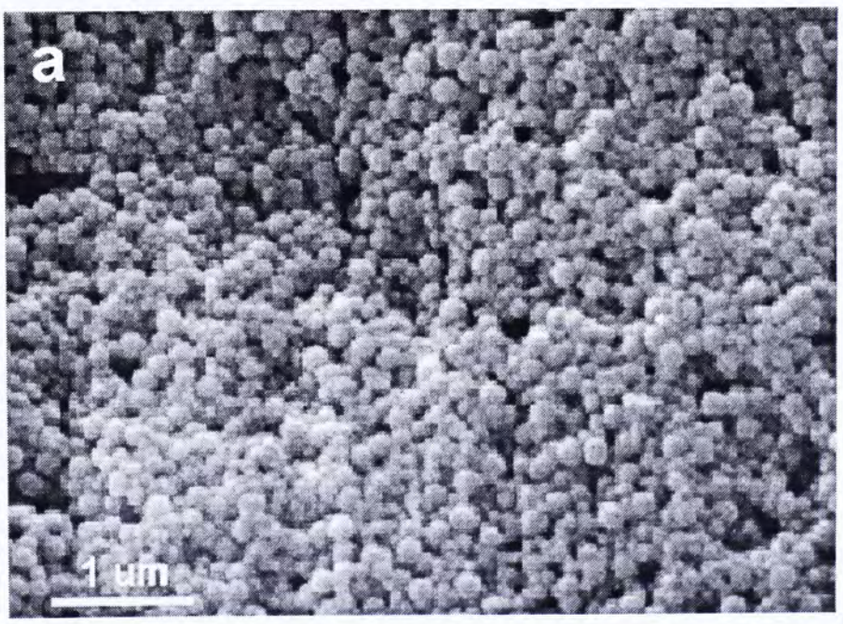

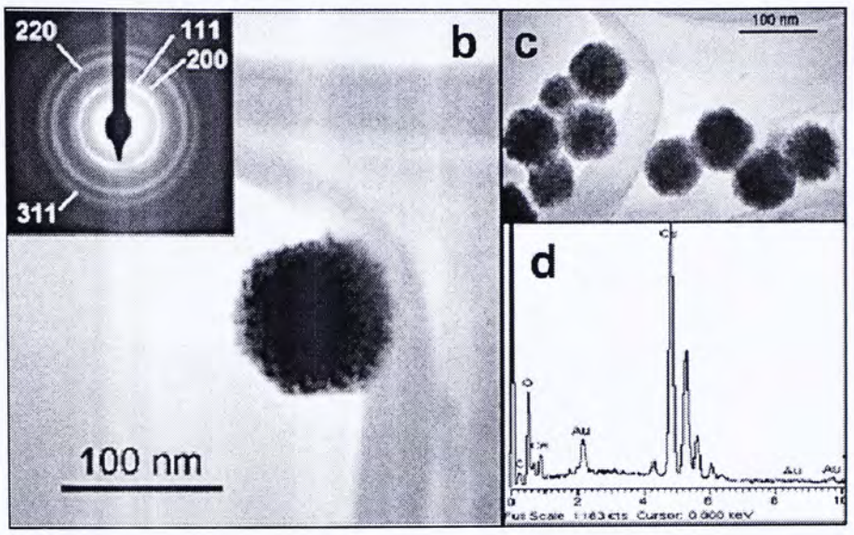

Figures 3.1 a) SEM images of annealed CeO_2 nanospheres at 600°C for 4 h. b, c) CeO_2 nanospheres TEM images and its electron diffraction pattern (inset), d) EDX of nanospheres shows the ratio of Ce : O ≈ 2:1.

The SEM and TEM images of the annealed CeO_2 microrods synthesized with different reaction times are shown in Figures 3.1e and f, respectively. When the reaction media was heated for 24 h, microrods were obtained with widths of several hundred nanometers and lengths ranging between 15 and 20 μm (based on SEM/TEM image estimations). A large aspect ratio is thus achieved in the range of 25 to 33. Furthermore, each microrod shows a highly uniform diameter. From the enlarged image, both ends of the microrods are spin-shaped. The HRTEM image (Figures 3.1g) indicates clearly that the microrods are composed of many tiny grains with different orientations. The spacing between two adjacent lattice planes is 0.313

nm, which corresponds to the separation of the (111) lattice planes of CeO_2 (Figures 3.1g).

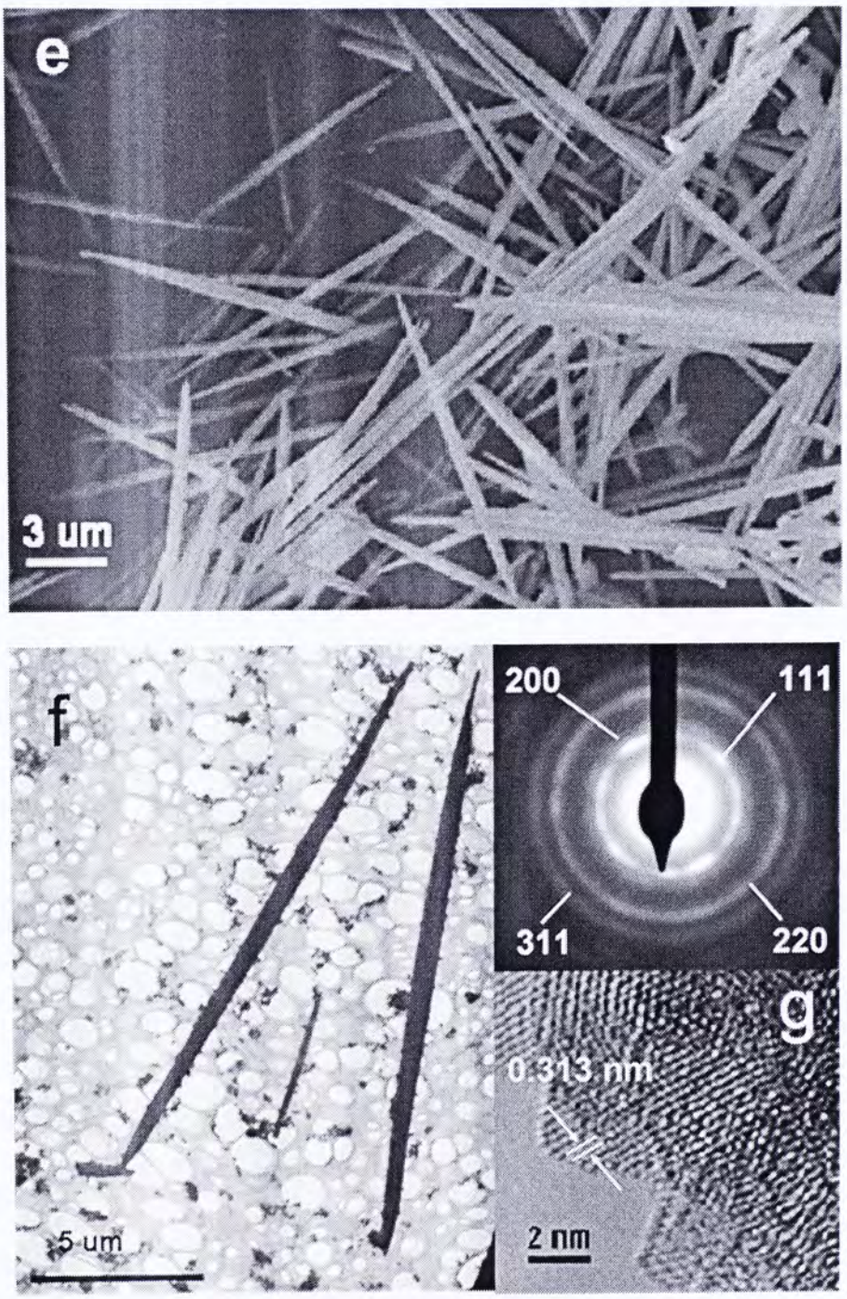

Figure 3.1 SEM e) and TEM f) images of annealed CeO_2 microrods at 600°C for 4 h, g) HRTEM image of the selected area of the CeO_2 microrods.

Representative SEM and TEM images of the spindle-like microstructure are shown in Figures 3.1h and i. When refluxed for 24 h, spindle-like particles are formed with widths of several hundred nanometers and lengths ranging from 2 to 4 μm and aspect ratios of 4 to 8. Moreover, each spindle-like particle shows sharp-ends and curved edges. The width of these microrods increases from the ends to the centre. The widths of microrods and spindle-like particles are similar, but they differ in length. A careful look from the end elevation of spindle-like particles reveals pyramid-like ends with sharp-edges (the insets in Figures 3.1h), whereas microrods have pin-like ends. In order to study the growth process of these microrods, an aliquot of the reaction mixture was withdrawn at 4, 8, 12 and 16 h. As illustrated in Figures 3.2a to d, the microrods and nanospheres co-existed in the reaction mixture after 8 h reflux, but neither small-size microrods nor pre-formed product can be observed. This may suggest that the microrods are not grown from the aggregation of nanospheres. In fact, the amount of microrods increased with duration of the reaction. However, the length and width of the microrods are independent of reaction time and refluxing temperature. After a 16 h reaction, over 90% of the products are microrods (estimated from the SEM micrograph) with just a small amount of nanospheres.

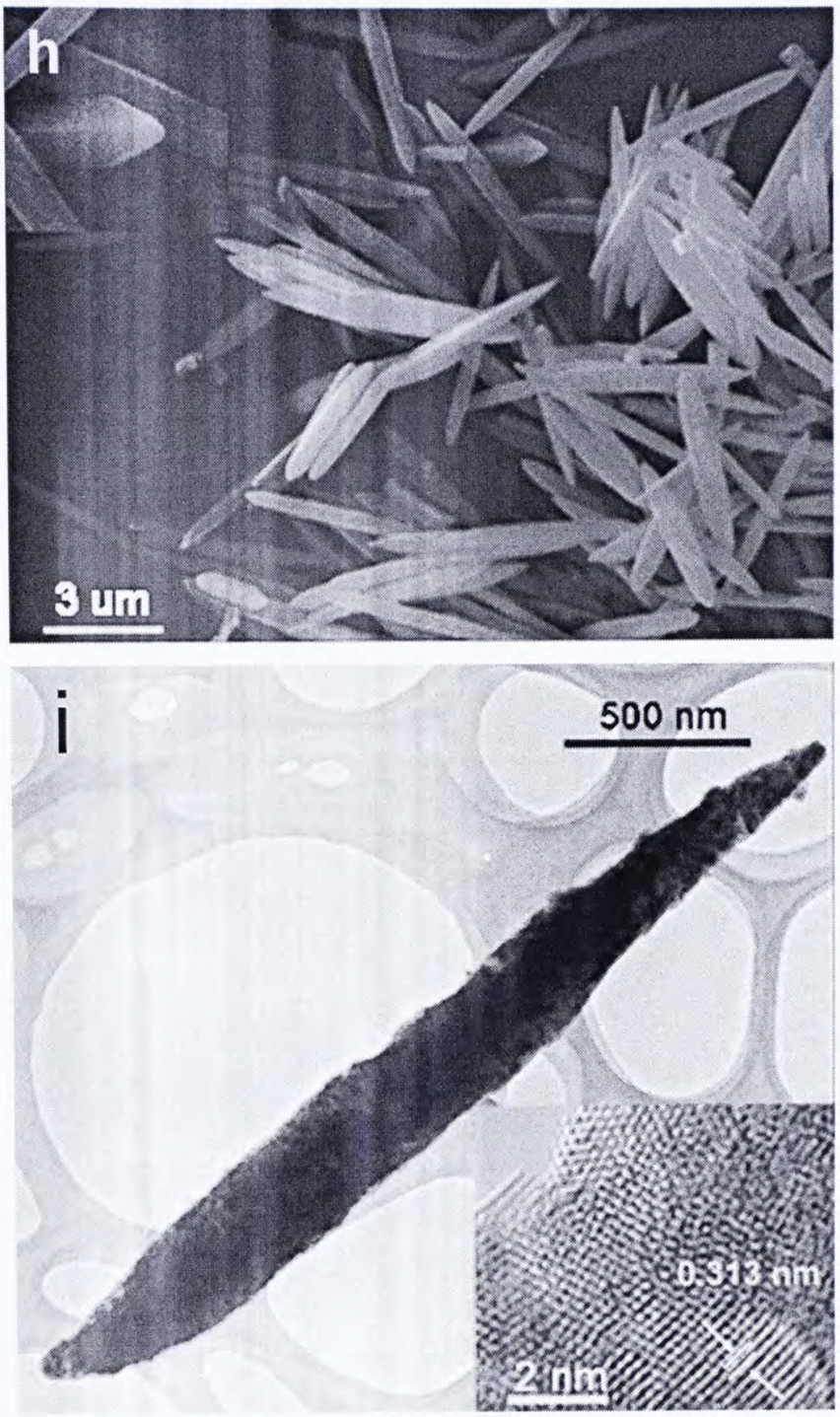

Figure 3.1 h) SEM image of CeO_2 spindle-like particles and g) TEM and HRTEM images (inset) of individual nanoparticles.

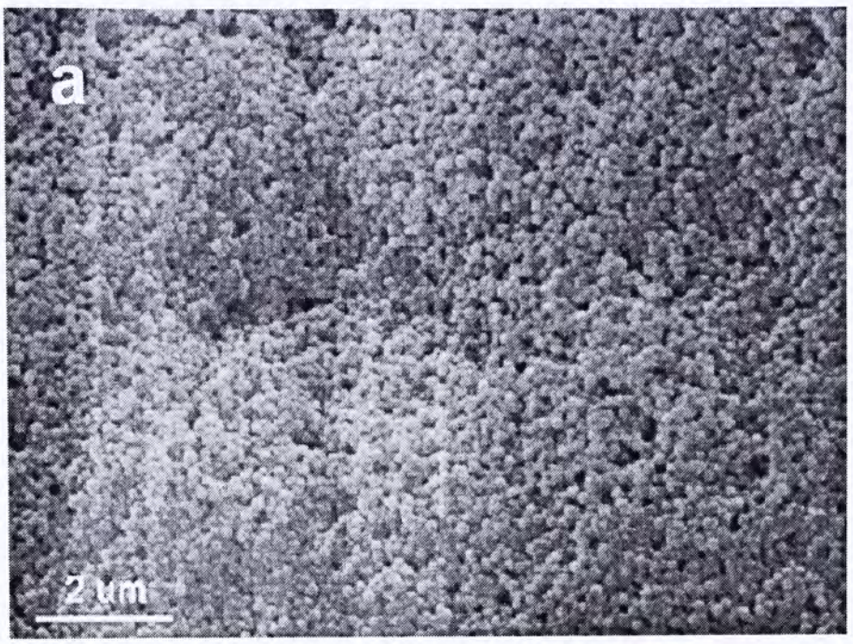
a
2 um

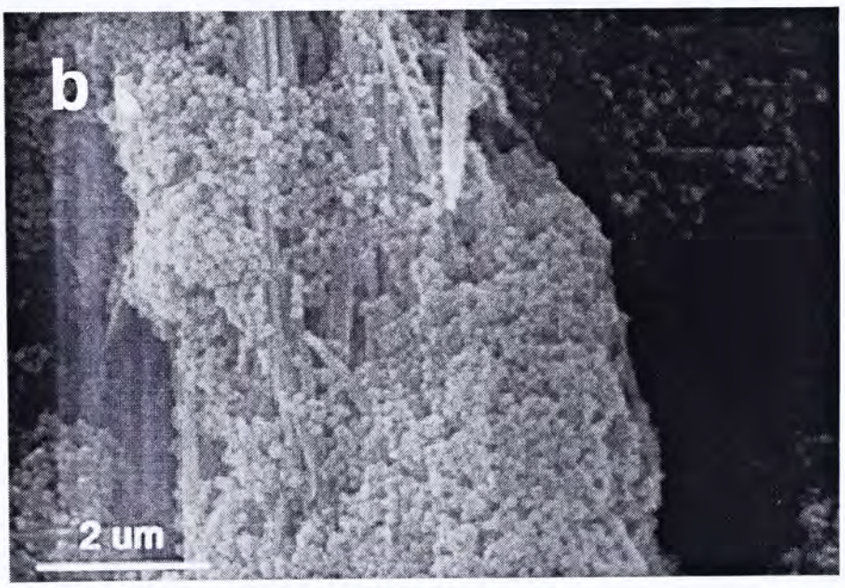
b
2 um

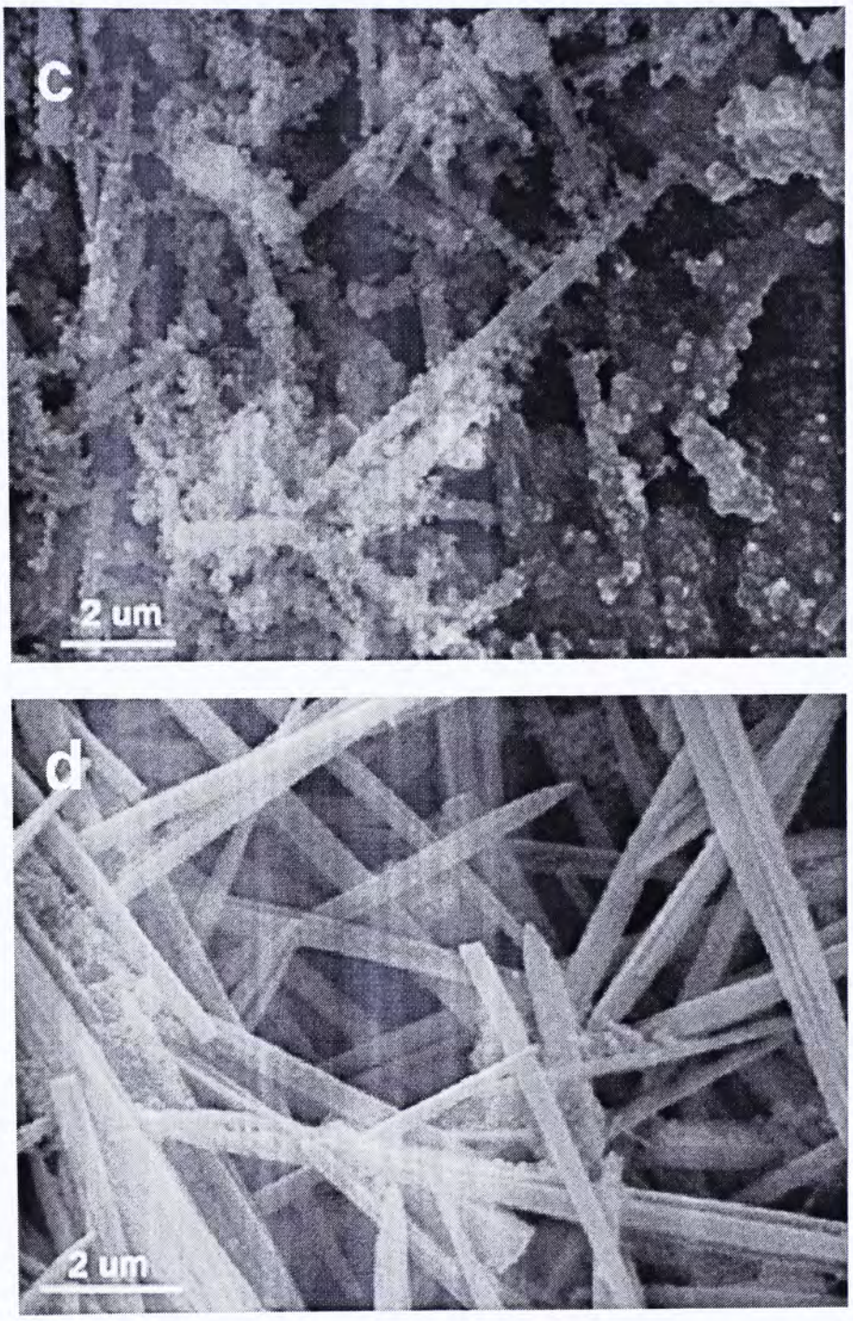

Figure 3.2 SEM images of product obtained from the reaction mixture 80 mM $[(NH_4)_2Ce(NO_3)_6]$ in ethylene glycol with 0.16 M PVP heating reflux for a) 4 h, b) 8 h, c) 12 h d) 16 h.

The above-mentioned investigations reveal that the morphology of CeO_2 nanoparticles is controlled by the concentration of cerium precursor and reaction duration. In order to study the growth mechanism, X-ray diffraction (XRD), Fourier-transform infrared spectroscopy (FT-IR), and X-ray photoelectron spectroscopy (XPS) were used to characterize the as-prepared sample and the calcined sample.

3.3.2 XRD Analysis

Phases and purities of the as-prepared samples were investigated by the XRD Analysis. Figure 3.3a shows the XRD patterns of the as-prepared CeO_2 nanospheres. All the diffraction peaks can be indexed as a face-centered cubic-phase CeO_2 (JCPDS 34-0394). The lattice parameters calculated from this pattern (a=b=c=3.12Å) are in accordance with the reported values. Surprisingly, diffraction patterns for the as-prepared microrods and spindle-like particles are completely different from those for the nanospheres (Figures 3.3b and c). Based on the XRD patterns, the microrods and spindle-like particles have the same crystal structure and can be identified as cerium formate (JCPDS 49-1245, $Ce(HCOO)_3$). The as-prepared samples are free of impurities and there is no trace of the precursor.

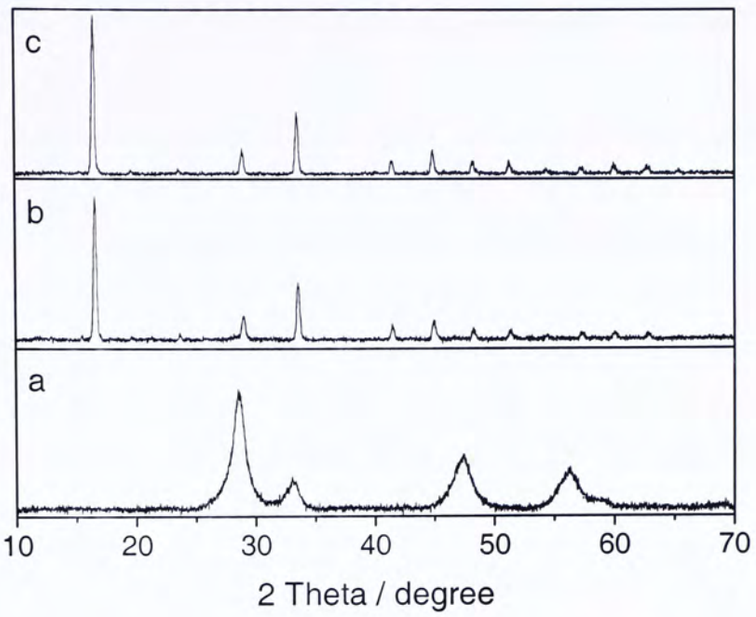

Figures 3.3 XRD pattern for as-prepared samples: a) CeO_2 nanospheres b) rod-shaped precursor $Ce(HCOO)_3H_2O$ and c) spindle-like particles $Ce(HCOO)_3H_2O$ precursor.

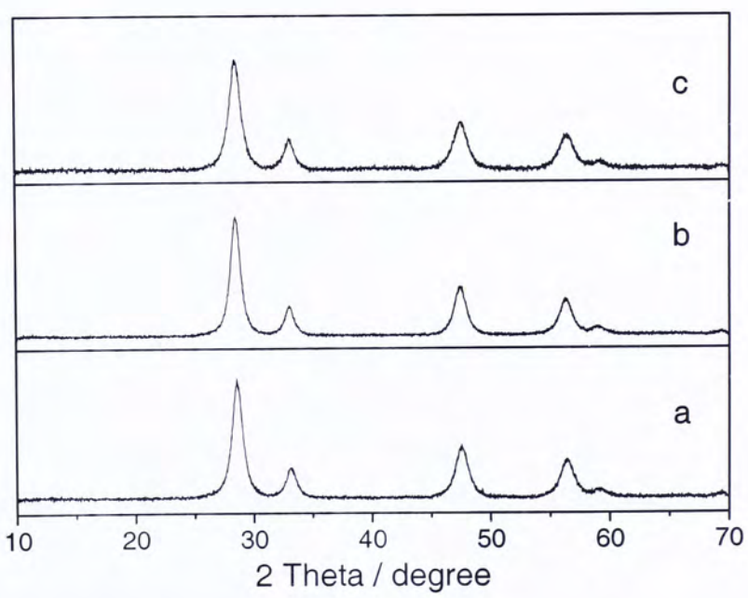

Figures 3.4 XRD pattern for calcined CeO_2 samples: a) nanospheres b) microrods and c) spindle-like particles.

All samples maintain their original morphology but they all exhibit face-centered cubic lattice structure after calcination at 600°C for 4 h (Figures 3.4). The diffraction peaks match that of a face-centered cubic-phase CeO_2 reported in JCPDS (34-0394). The lattice parameters calculated from these patterns are summarized in Table 3.2. A closer observation of the reflection peak (111) at *ca* 28.5° (Figures 3.5) reveals that there is a slight down-shift from the nanospheres to microrods and spindle-like particles with a corresponding increase in the unit cell volumes (Table 3.2).

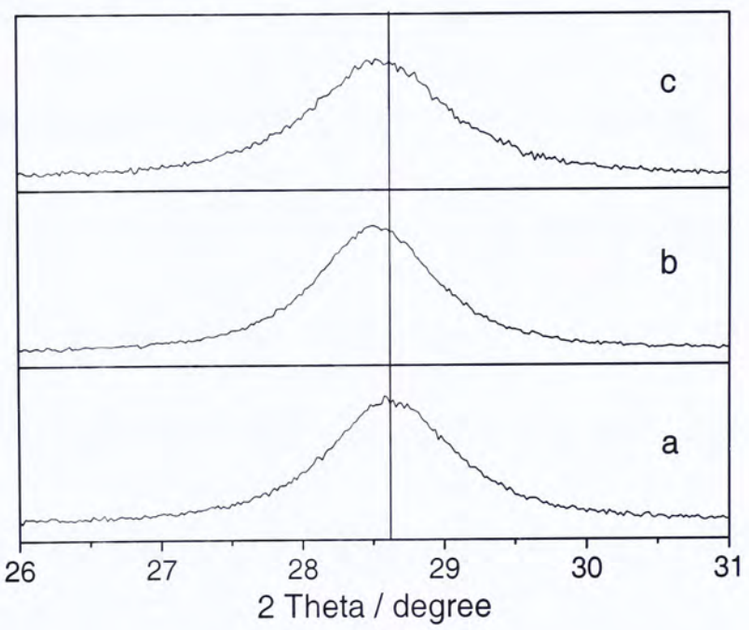

Figures 3.5 XRD spectra (2θ = 26° to 31°) for annealed samples: a) nanospheres, b) microrods and c) spindle-like particles.

Table 3.2 Summary of the lattice parameters.

Morphology	2θ	d / Å	a / Å	Lattice volume / $Å^3$	Crystal size / nm
Spheres	28.6(1)	3.11(8)	5.40(0)	157.(5)	8.9(7)
Rods	28.5(2)	3.12(7)	5.41(6)	158.(8)	8.4(1)
Spindle-like	28.5(1)	3.12(8)	5.41(9)	159.(0)	7.6(0)

3.3.3 N_2-Soprtion.

Physicochemical properties of as-prepared and annealed samples are listed in Table 3.3. Interestingly, both surface area and pore volume increased after calcination. The surface area of CeO_2 nanospheres shows a 4-fold increase while that of other samples (microrods and spindle-like particles) also increase significantly. Before calcination, the cerium formate repeating units are linked together through the organic-based bridge to give a 1D dimensional structure. High temperature treatment breaks the bridging units and initiates the crystallization of the repeating units. The secondary structure of calcined nanospheres, rod or spindle-like shape can be considered as the agglomeration of each primary nanoparticles. Therefore, the surface area and the pore volume greatly increased after calcinations. The nitrogen adsorption-desorption isotherms and the Barrett-Joyner- Halenda (BJH) pore size

distributions for as-prepared and calcined nanospheres, microrods and spindle-like particles are shown in Figures 3.6, 3.7 and 3.8. From Figure 3.7a, two distinct capillary condensation steps appear at P/P_o values of about 0.5 and 0.8, respectively. BJH model analysis of these as-prepared microrods gives one narrow peak centered at 5 nm in the pore size distribution and another broad peak in the range of 10 to 20 nm with an evident maximum at 13 nm, showing a dual mesoporous distribution. The desorption branch also displays two distinct steps. This suggests that two pore systems with different diameters are present to form a three-dimensional pore structure. A similar pattern can also be observed in the as-prepared spindle-like particles (Figure 3.8a). Two distinct capillary condensation steps also can be observed at P/P_o values of about 0.45 and 0.8, respectively, from Figure 3.8a. A narrow peak centered at 3.5 nm and another broad peak in the range of 10 to 20 nm with an evident maximum at 14 nm in pore distribution clearly suggests a bimodal porosity distribution. The isotherms for both samples are apparently of type IV, typical of mesoporous materials. These results confirm the formation of bimodal mesoporous cerium microrods and spindle-like particles.

Table 3.3 Physicochemical properties of the as-prepared and annealed samples

Shape of the samples	S_{BET}[a] (m^2g^{-1})	V[b]/ (cm^3g^{-1})	D_{BJH}[c]/ (nm)
Spheres (as-prepared)	40.3	0.077	7.6
Spheres (calcined)	158.2	0.23	5.8
Rod (as-prepared)	67.8	0.13	7.8
Rod (calcined)	145.0	0.20	5.6
Spindle (as-prepared)	67.4	0.11	7.1
Spindle (calcined)	170.0	0.19	4.4

a BET surface area calculated from the linear part of the BET plot (P/P_0 = 0.1–0.2).

b Total pore volume, taken from the volume of N_2 adsorbed at P/P_0 = 0.995.*c*

Average pore diameter, estimated using the desorption branch of the isotherm and the Barrett–Joyner–Halenda (BJH) formula.

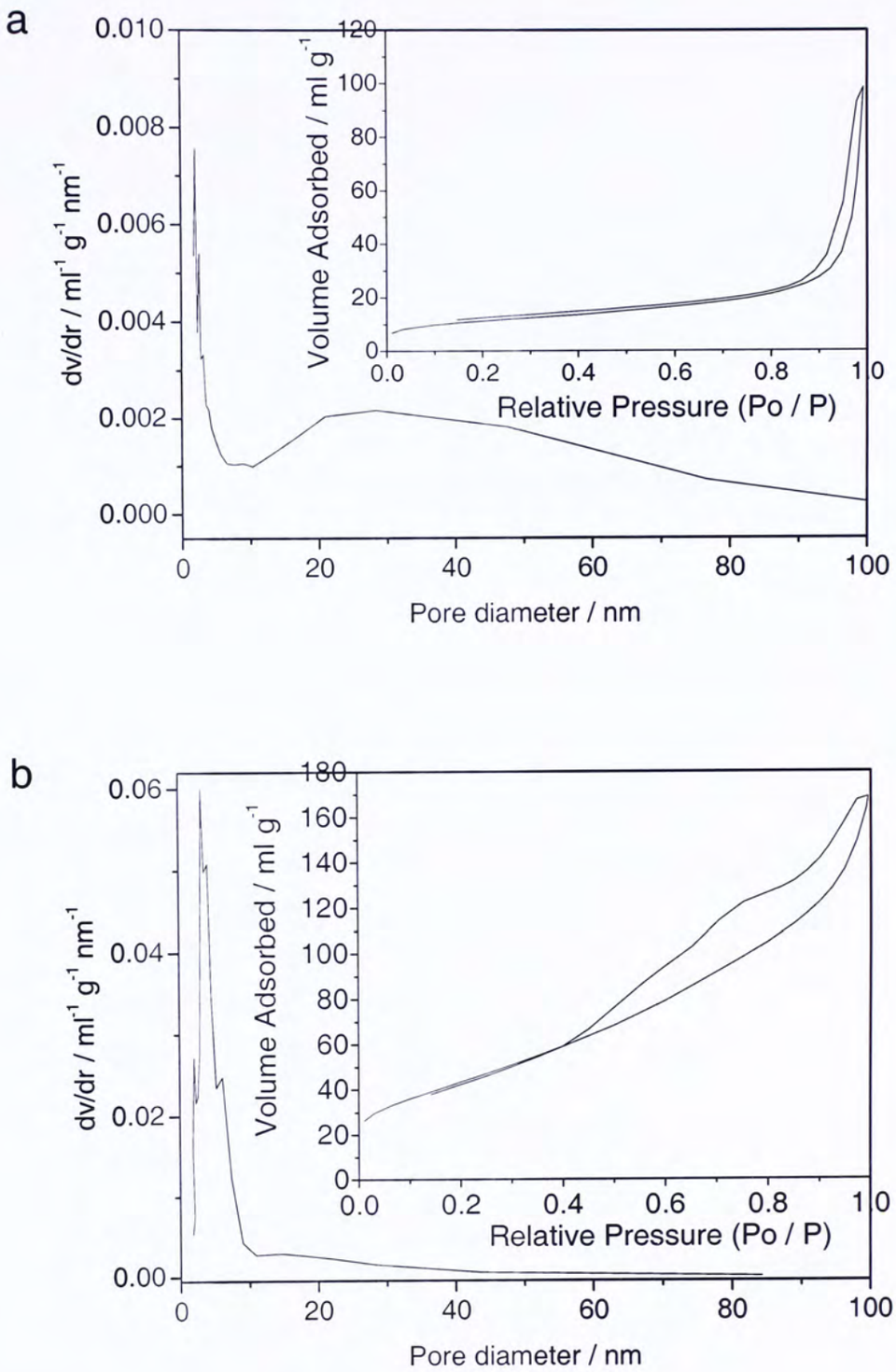

Figure 3.6 Nitrogen adsorption-desorption isotherms and BJH pore size distribution for a) as-prepared and b) calcined CeO_2 nanospheres.

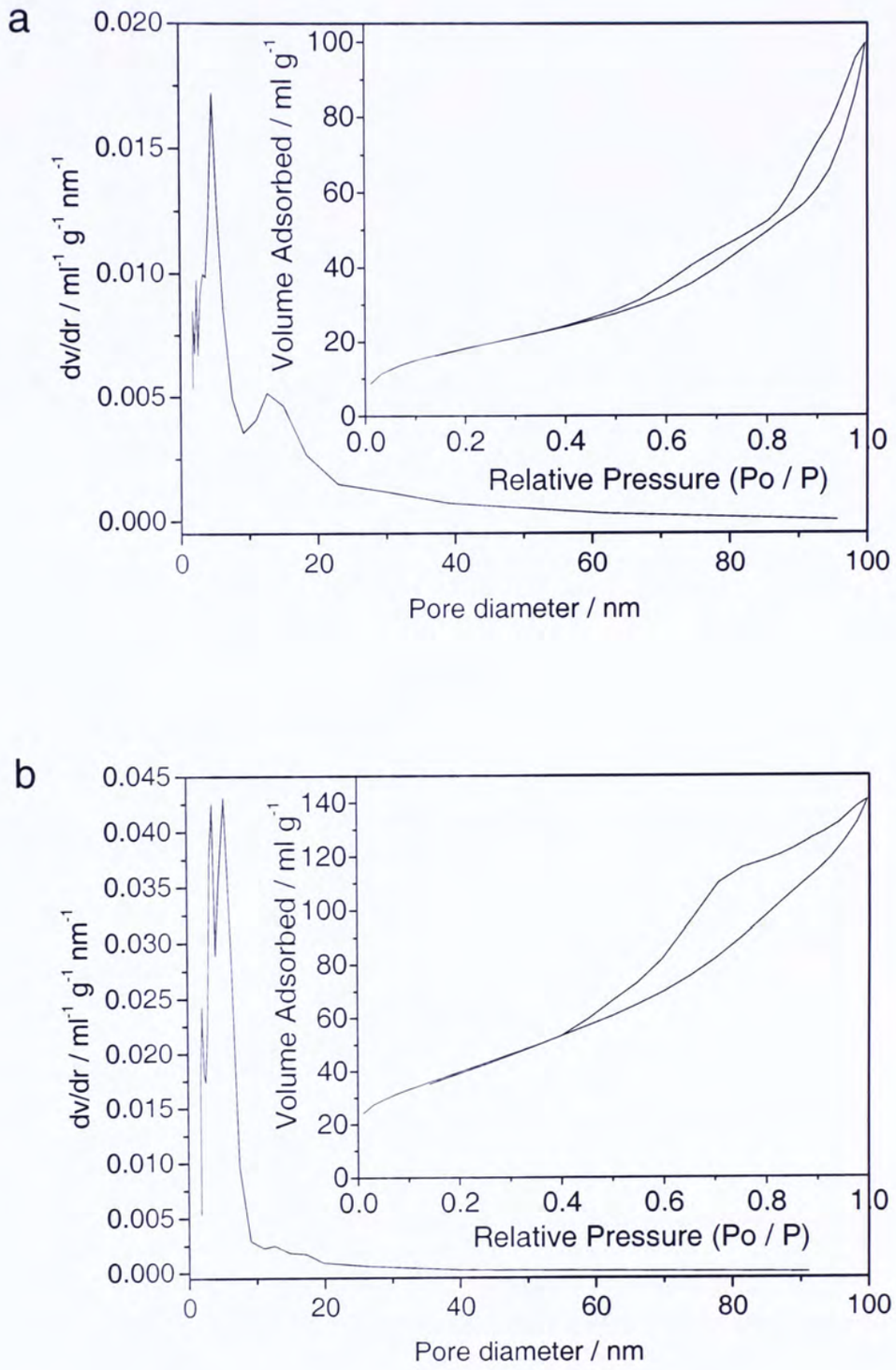

Figure 3.7 Nitrogen adsorption-desorption isotherms and BJH pore size distribution for a) as-prepared and b) calcined CeO_2 microrods.

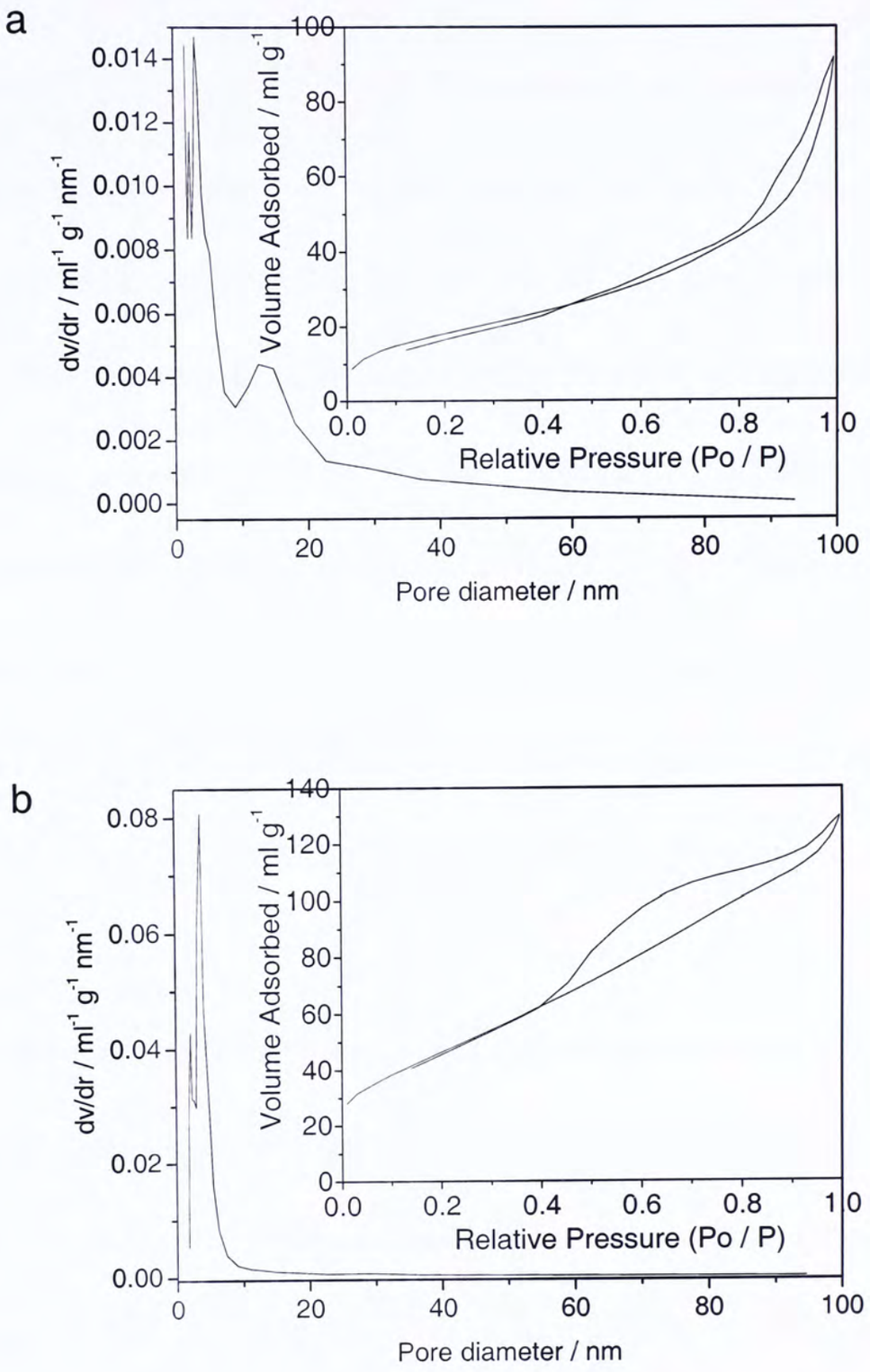

Figure 3.8 Nitrogen adsorption-desorption isotherms and BJH pore size distribution for a) as-prepared and b) calcined CeO_2 spindle-like particles.

3.3.4 X-ray Photoelectron Spectroscopy

Ce3d electron core level XPS spectra for as-prepared and calcined nanosphere, microrod and spindle-like particle samples are shown in Figures 3.9a to c. The 3d level is formed by two series of peaks: $3d_{5/2}$ and two very pronounced "shake-up" satellites; and $3d_{3/2}$ with the same characteristics. The peaks labeled v and v_2 have been assigned to a mixing of the Ce $3d^9\ 4f^2\ L^{n-2}$ and Ce $3d^9\ 4f^1\ L^{n-1}$ Ce(IV) final states, and the peak denoted v_3 corresponds to the Ce $3d^9\ 4f^0\ L^n$ Ce(IV) final state. Moreover, lines v_0 and v_1 are assigned to the Ce $3d^9\ 4f^2\ L^{n-1}$ and Ce $3d^9\ 4f^1\ L^n$ states of Ce(III). The same assignment can be applied to the u structures, which correspond to the Ce $3d_{3/2}$ levels.[19] The Ce3d XPS spectra of as-prepared microrods and spindle-like particles are very different from those of the CeO_2 nanospheres. The increasing intensity of the u_1, v_1 band and reduction of the other bands in as-prepared cerium microrods and spindle-like particles strongly suggest that the oxidation state of cerium is mainly from Ce(III) (Figures 3.9b, c). The energy separation between the v and v_1 peaks is about 3.0 eV, close to the values observed for Ce(III) compounds.[20] As compared with the XPS spectra for as-prepared and calcined cerium nanospheres (Figure 3.9a), an increase in band intensities of u_1 and v_1 reveals that cerium is already in a partially reduced form. This is because the reaction with CeO_2 and ethylene glycol leads to partial reduction of Ce(IV). The relatively high

intensity of other Ce(IV) lines leads to the conclusion that both Ce(III) and Ce(IV) co-existed in the nanosphere structure before calcination. Based on the relative intensity of Ce(IV) and Ce(III) lines, as-prepared nanospheres should mainly be built up from Ce(IV) nanocrystals. After high-temperature calcination, the sharp decrease in u_1 and v_1 lines and increase in other Ce(IV) lines reveals that all the cerium in samples convert to Ce(IV) as the final oxidation state. Therefore, the XPS and XRD results indicate that ammonium cerium nitrate first decomposes to cerium (IV) oxide and further reduces to cerium (III) formate by ethylene glycol. Reaction of ethylene glycol and cerium (III) formate induces the 1D morphology formations.

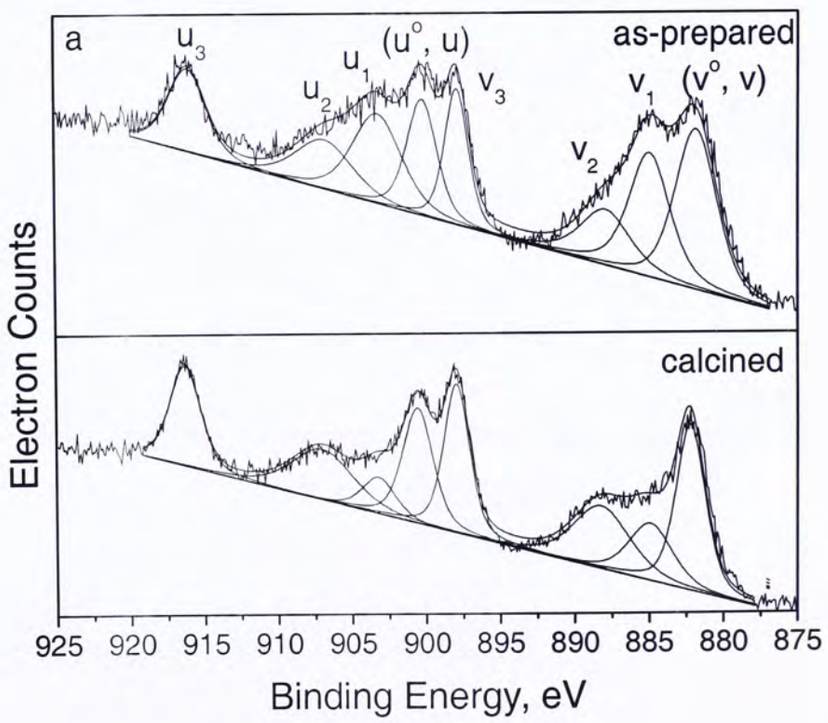

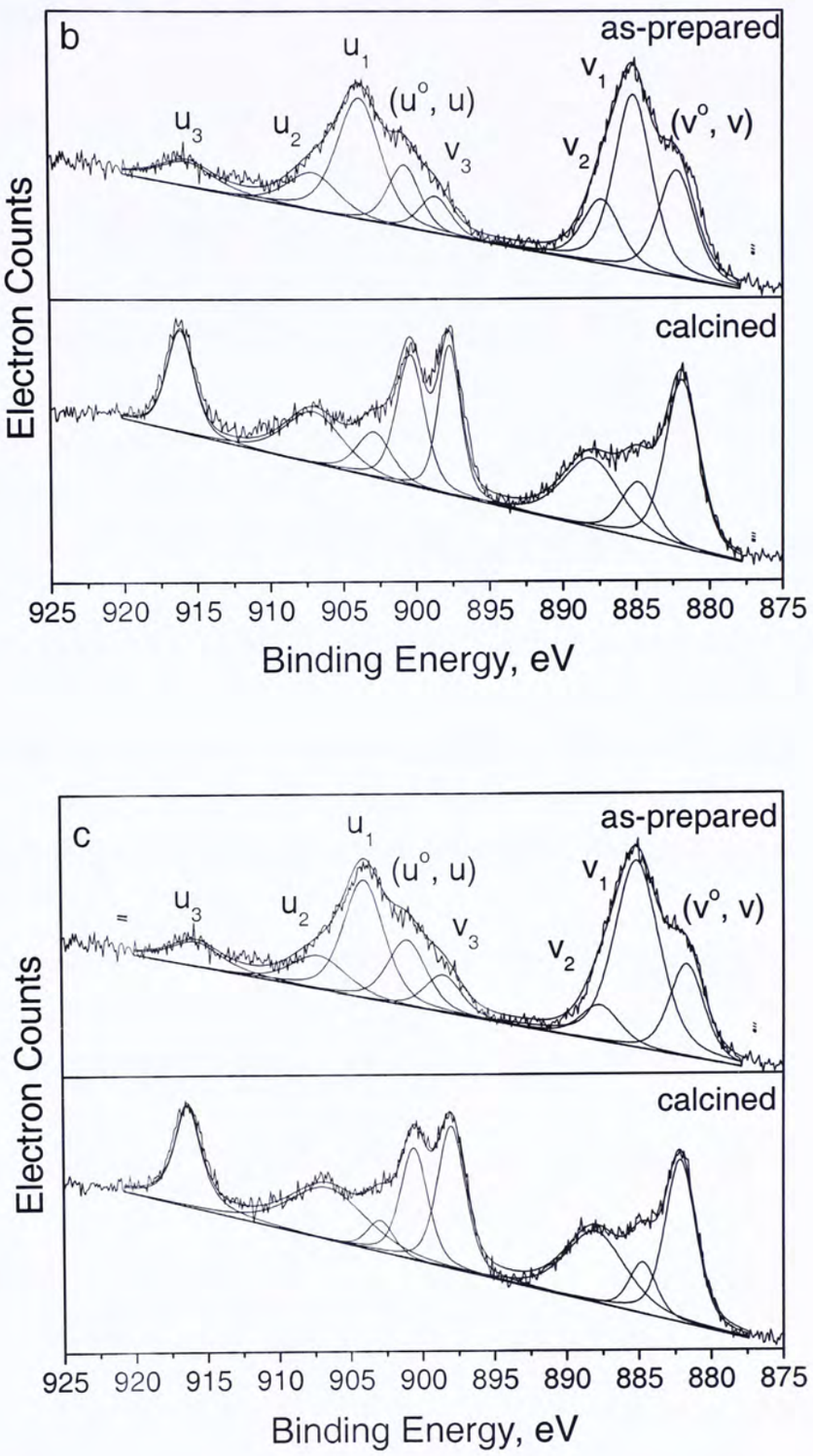

Figures 3.9 XPS spectra for as-prepared and annealed CeO_2 sample: a) nanospheres b) microrods and c) spindle-like particles

3.3.5 FT-IR Analysis

Figure 3.10a shows the FT-IR spectra for the as-prepared and calcined cerium microrods and spindle-like particles. The typical peaks for metal formate salt are found at *ca.* 1600, 1360 and 775 cm^{-1}. The first two frequencies correspond to the stretching mode of C=O in oxalate group and the last one refers to its bending mode. The absence of the Ce-O stretching band at *ca.* 400 cm^{-1} confirms that the as-prepared microrods and spindle-like particles are not composed of CeO_2. It should also be noted that no C-H stretching peaks (2800 to 2900 cm^{-1}) can be found in the FT-IR spectra, which is different from that reported by Xia *et al.* for the formation of titanium dioxide nanowires from titanium alkoxide.[4a, b] In the case of TiO_2, the 1D morphology is put together by the linking action of ethylene glycol to yield repeating units of (O-CH_2CH_2-O-M). In the present study, the repeating units are cerium formate.

After calcination, only the Ce-O stretching band remains at *ca.* 400 cm^{-1}, indicating the structural transformation to CeO_2 from the cerium formate as-prepared compound. The peak at *ca.* 3400 cm^{-1} corresponds to the physically adsorbed water on the sample. As compared with the nanospheres (Figure 3.10b), the disappearance of the peaks corresponding to C=O in oxalate group confirms the different formation

mechanisms in nanospheres and microrods. The creation of spherical particles should be mainly due to the capping action by PVP. This can also be supported by the appearance of C-N (1560 cm^{-1}) and C=O (1660 cm^{-1}) stretching frequency from the di-substituted amide group in FT-IR studies. Both FT-IR spectra for as-prepared and calcined samples show absorption peaks at 400 to 450 cm^{-1} and reveal that as-prepared samples are structurally combined as CeO_2.

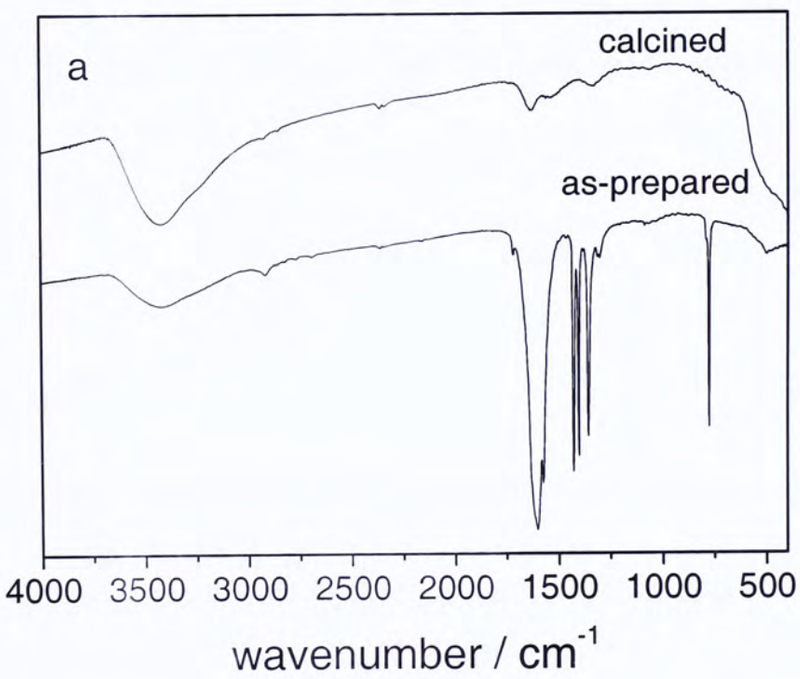

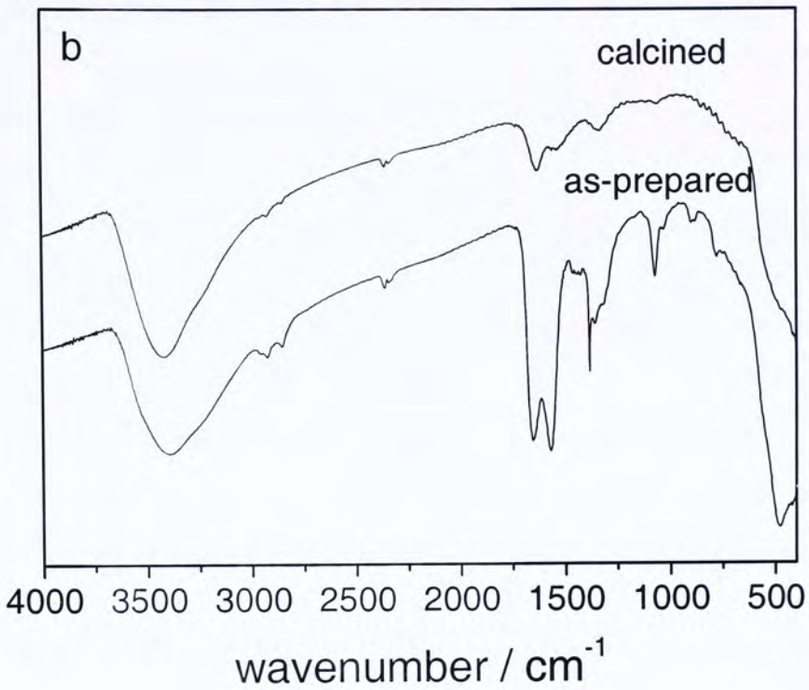

Figure 3.10 FT-IR spectra for a) rod-shaped and spindle-like shaped sample and b) nanospheres.

3.3.6 GC-MS Analysis

In order to study the reaction between ethylene glycol and ammonium cerium nitrate, 2 ml of the reaction mixture were withdrawn and analyzed at certain time intervals during reflux. Samples were centrifuged and a clear pale yellow solution was obtained. The content of the reaction mixture was analyzed by GC-MS. A polymerization product of ethylene glycol can be found in the GC chromatograph after 2 h (Figure 3.11a). This compound with a retention time of 5.65 min has been identified by MS (Figure 3.12a). The product, 2-[2-(2-hydroxyethoxy)ethyoxy]-ethanol, was formed by the polymerization reaction of ethylene glycol under the high

temperature. Xia *et al.* also suggested that the bridging unit of the 1D SnO_2 nanowires came from the polymerization of ethylene glycol. The other two peaks positioned at 5.19 and 5.46 min correspond to a smaller polymer of ethylene glycol and head of PVP (Figures 3.12b and c). After further heating reflux for 4, 8, and 10 h (Figure 3.11b, c and d), oxalic acid appeared as a peak positioned around 5.4 min (Figure 3.12d). It was surprised that the peak height of the oxalic acid increased with the reaction time, and indicated that there was more ethylene glycol molecule oxidized to oxalic acid (Figure 3.11e). From XRD analysis, it is clearly shown that the product obtained at the beginning was CeO_2 nanospheres and cerium formate compound was formed after 24 h. $(NH_4)_2Ce(NO_3)_6$ was decomposed to CeO_2 nanospheres in the first few hours of reaction. These CeO_2 nanospheres further reacted with ethylene glycol to give the cerium formate compound eventually. The gradual increase in the amount of oxalic acid suggests that the rate for the transformation of CeO_2 nanospheres to cerium formate may be dependent on the amount of oxalic acid. It is shown in Figure 3.2 that no cerium formate microrods were formed at the early stage. They begin to appear only when oxalic acid becomes available in the reaction system.

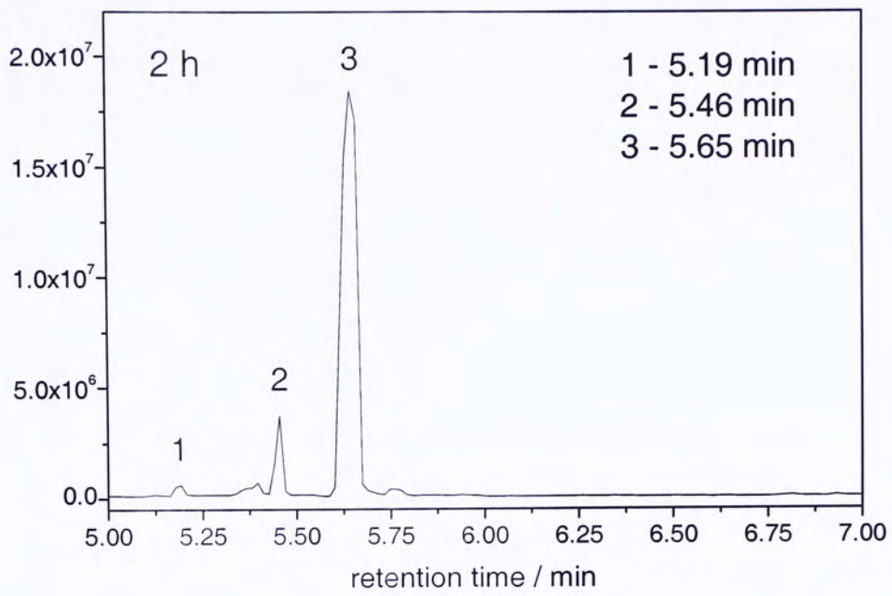

Figure 3.11a GC chromatograph of the solvent mixture after 2 h heating reflux. The highest peak with the retention time of 5.65 min is given by the product result of polymerization of ethylene glycol.

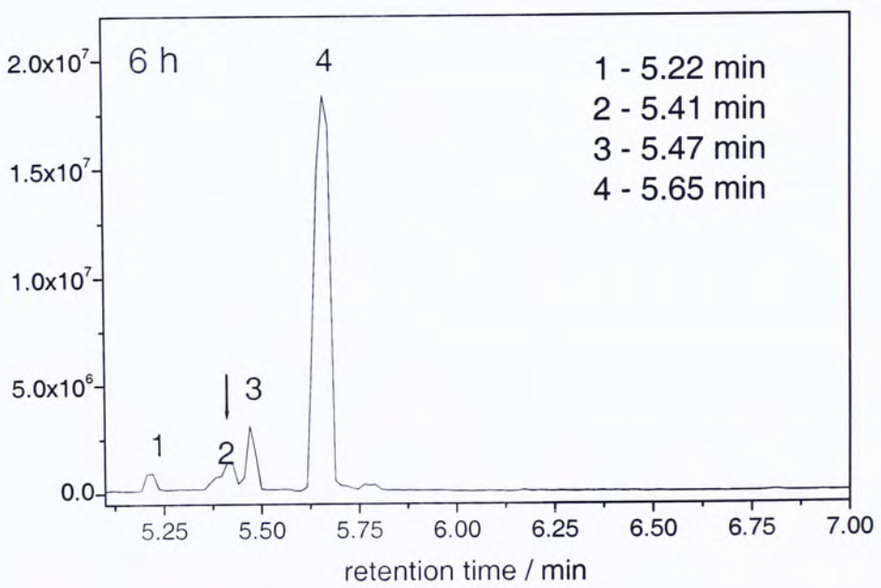

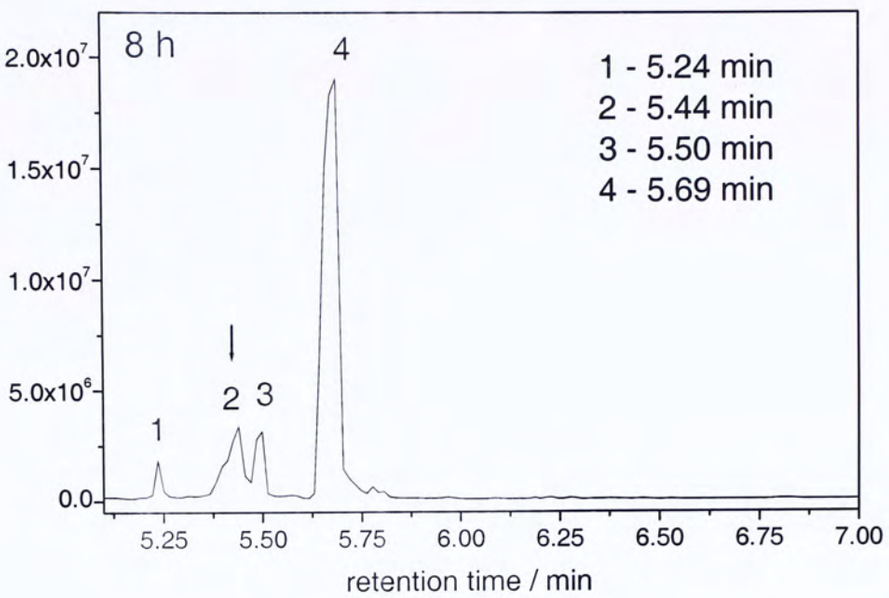

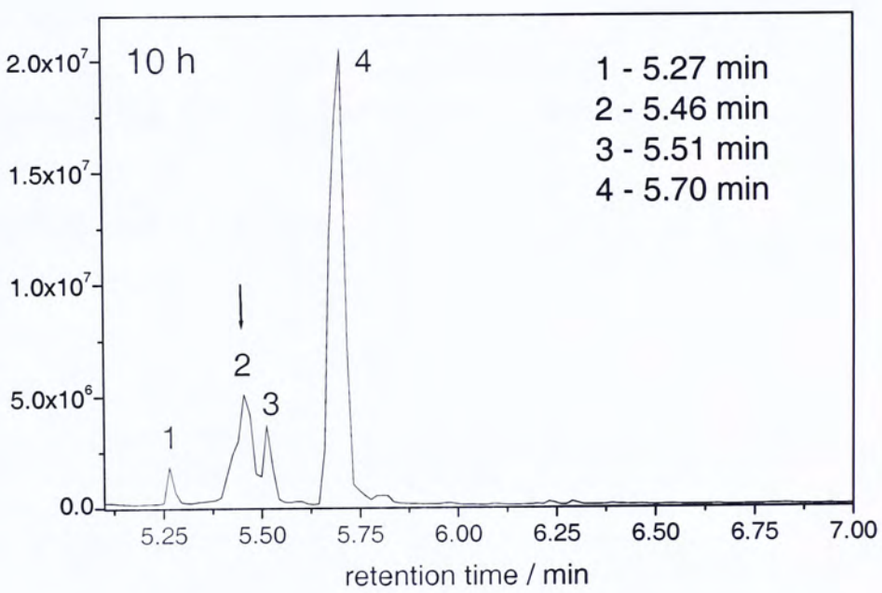

Figure 3.11b, c and d. GC chromatograph of the solvent mixture after 6, 8 and 10 h heating reflux. Increase in the peak intensity (~ 5.4 min) indicated the more oxalic acid formed in the prolonged refluxing reaction.

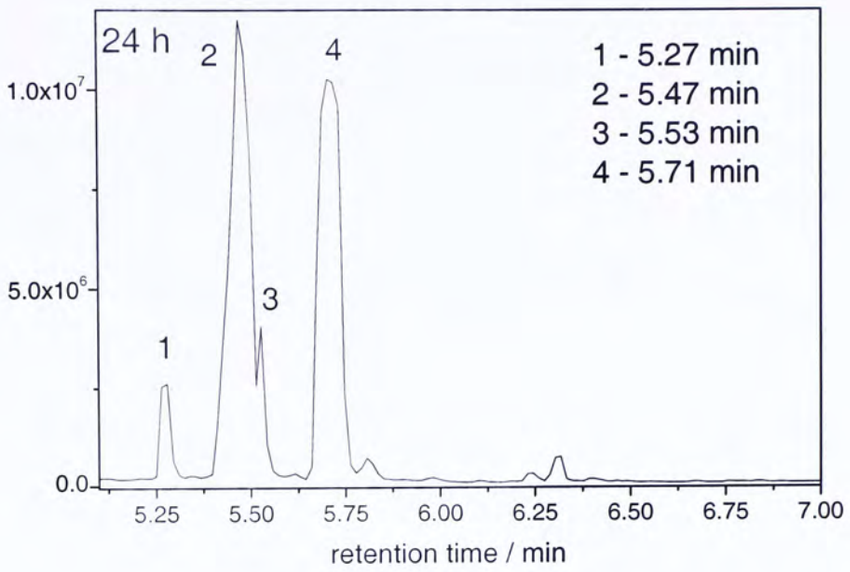

Figure 3.11e GC chromatograph of the solvent mixture after 24 h heating reflux. The gradual increase in the abundance of oxalic acid can be observed from peak height with the retention time of 5.47 min.

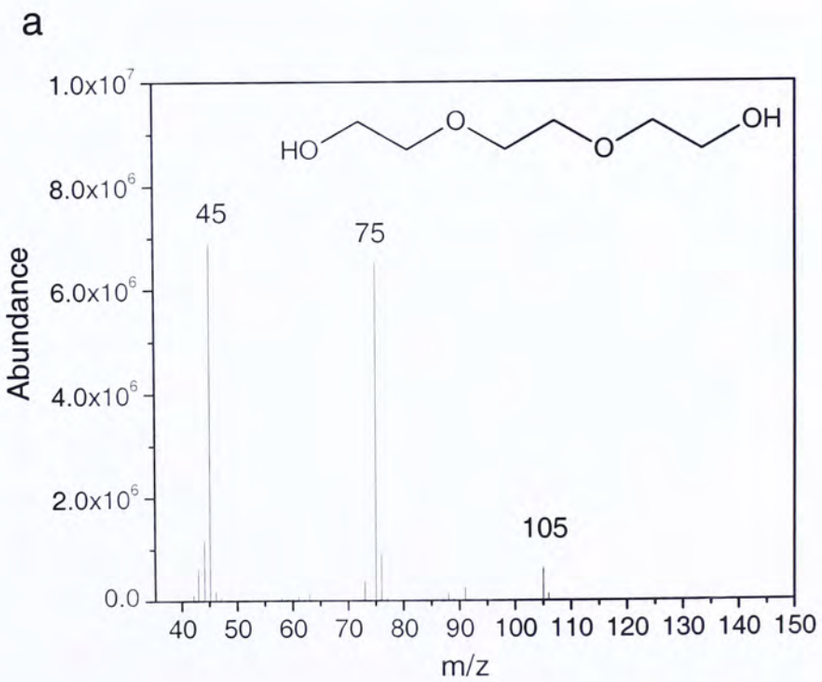

Figure 3.12a The MS data for 2-[2-(2-hydroxyethoxy)ethoxy]ethanol with a retention time of 5.65 min. This compound was obtained by the polymerization of ethylene

glycol.

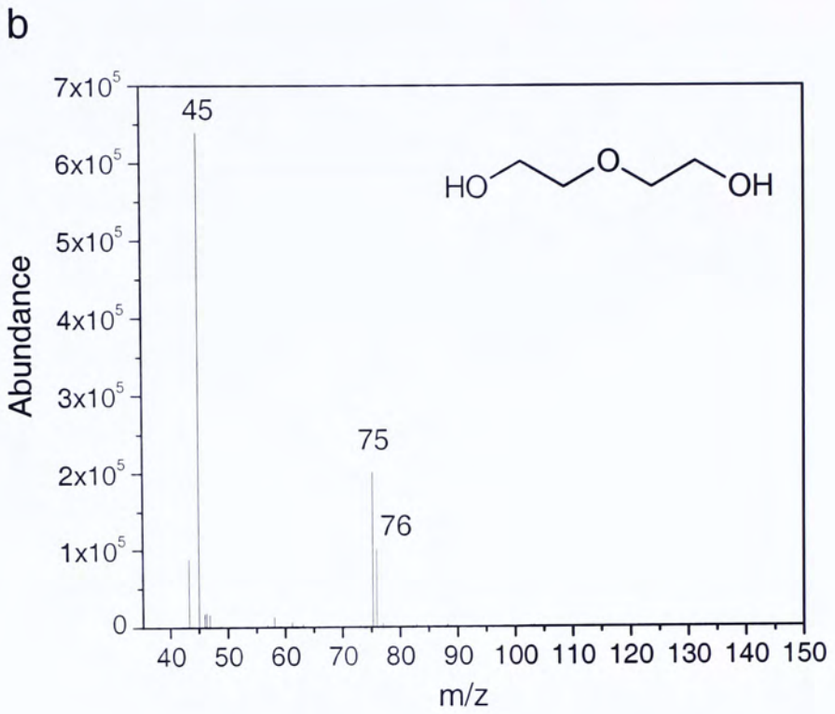

Figure 3.12b The MS data for the peak with a retention time of 5.19 min is corresponding to a smaller ethylene glycol polymer, 2(2-hydroxyethoxy)ethanol.

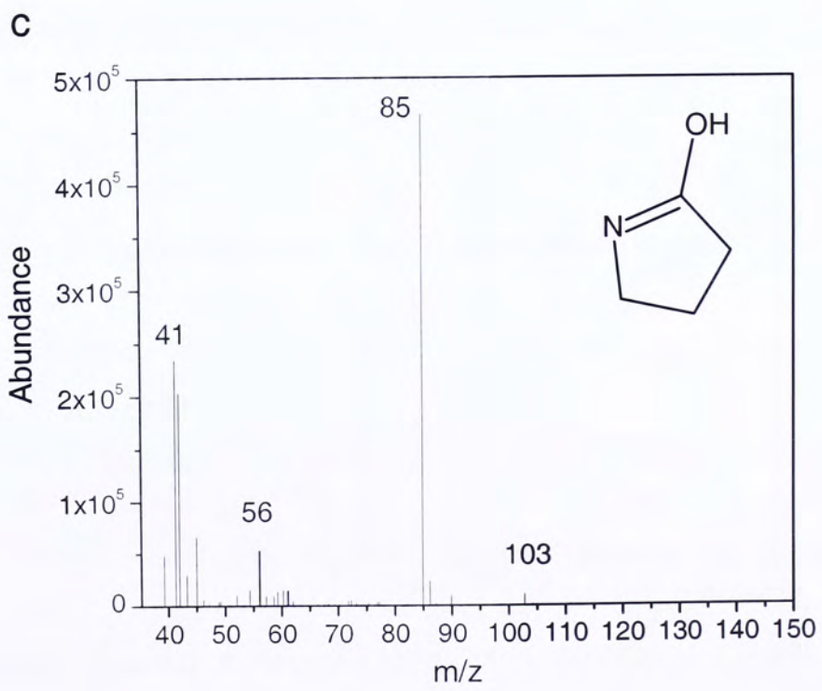

Figure 3.12c The MS data for the peak with a retention time of 5.46 min is corresponding to the head of PVP.

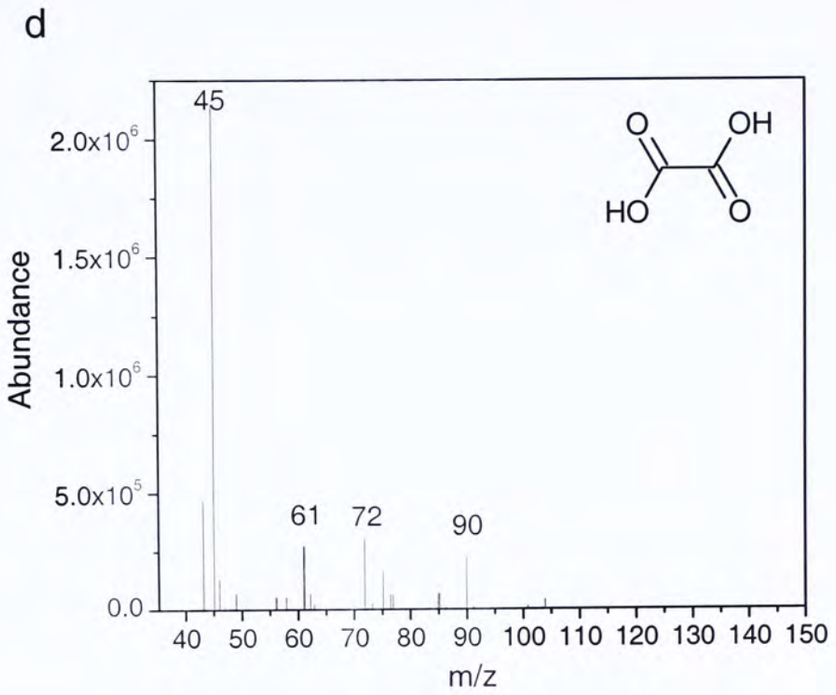

Figure 3.12d The MS spectrum for oxalic acid (retention time: 5.47 min).

3.3.7 Proposed Formation of CeO_2 nanospheres and their transformation to microrods

The cerium dioxide nanospheres are formed from the decomposition of ammonium cerium nitrate at temperatures above 185°C:

$$(NH_4)_2Ce(NO_3)_6 \rightarrow 4H_2O + 2N_2O + 4NO_2 + O_2 + CeO_2 \downarrow \text{(nanospheres)}$$

the spherical morphology results from the capping action of the surfactant PVP.[4f] The gradual transformation of nanospheres to microrods is illustrated in Figures 3.2a to d. These SEM images reveal that the microrods are not assembled by the

aggregation of the nanospheres. We believe the growth process starts with the reaction between the nanospheres and ethylene glycol. Ethylene glycol is an alcohol with a pKa value of about 15. It can be oxidized to carboxylic acids in the presence of oxidant, ammonium cerium nitrate as shown in the following reactions:[21]

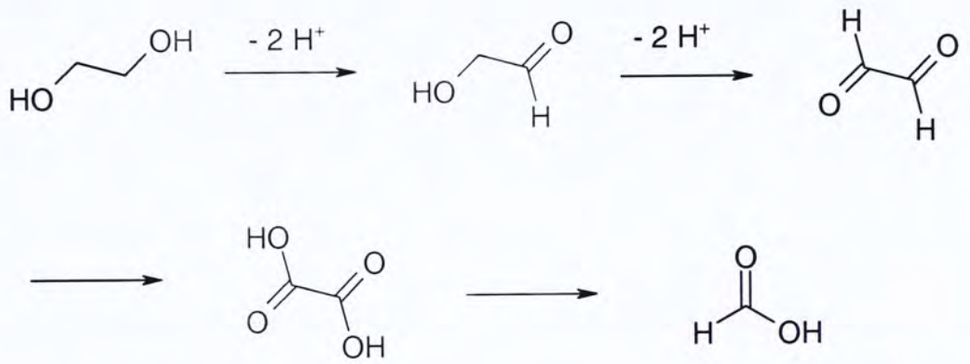

The oxidation of the alcohol groups gives aldehydes and then oxalic acid and formic acid. The presence of oxalic acid in the reaction mixture has been confirmed by GC-MS analysis (Figures 3.11d and 3.12d). Meanwhile, the cerium (IV) cations in CeO_2 are reduced by ethylene glycol to cerium (III). The Ce^{III} ion centers interact with the carboxylic groups in formic acid to yield cerium formate. The cerium formate acts as building blocks that is linked together to form the 1D microrods and spindle structures. However, the formate groups cannot be the bridging units due to a strong steric hindrance effect. The FTIR and GC-MS results reveal that the bridging unit is oxalic acid which comes from the oxidation of ethylene glycol. Each cerium formate unit reacts with oxalic acid to form a long chain. During the reaction, one of the formate groups of $Ce(HCOO)_3$ is substituted by an oxalate unit and the two remaining formate groups are arranged in a *trans*-geometry. The proposed formation

mechanism is as follows:

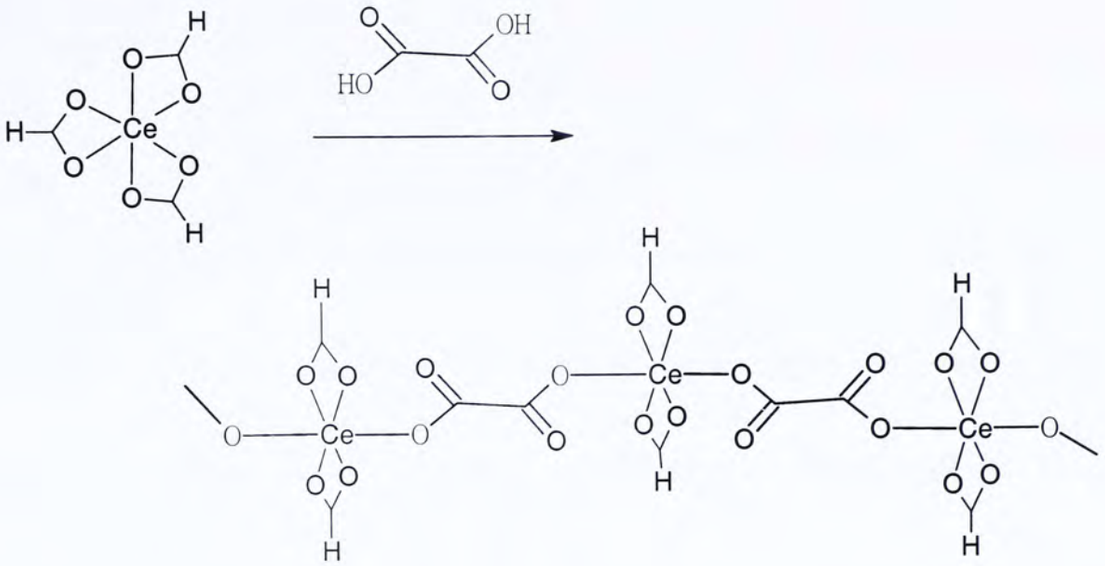

During calcination, the cerium formate nanostructures are oxidized to cerium dioxide.

3.3.8 UV absorption spectra and band gap energies

To reveal the correlation between the band gap energies and the grain size and morphology of the sample, the UV-Vis absorption spectra of calcined CeO_2 nanospheres, microrods and spindle-like particles were recorded. The optical absorption coefficient α was calculated according to the following equation:

$$\alpha = (2.303\times10^{3}A\rho)/lc,$$

where A is the absorbance of the sample, ρ is the real density of CeO_2 (7.28 g cm^{-3}), l is the path length of the quartz cell (1 cm), and c is the concentration of the ceria suspensions.[16] The UV-Vis absorption spectra of the cerium dioxide nanospheres, microrods and spindle-like particles were measured in ethanol suspensions (Figure

3.13). Both of them exhibit strong absorption bands at *ca.* 270 nm in the UV range, which originate from the charge-transfer between the O2p and Ce4f states in O^{2-} and Ce^{4+}.[22] This spectral profile indicates the charge transfer transition of Ce^{4+} overlaps with the $4f^1 \rightarrow 5d^1$ transition of Ce^{3+}. No absorption was detected above 500 nm in wavelength. A clear blue-shifting of the absorption threshold edge can be observed for the CeO_2 nanospheres and microrods, contrasting with the bulk powder. The plots of $(\alpha hv)^2$ vs. photon energy of CeO_2 nanospheres, microrods and spindle-like microstructure are shown in Figure 3.14. For direct transitions, the absorption coefficient near the absorption edge can be expressed in the equation:

$$\alpha \propto \frac{\sqrt{hv - E_d}}{hv}, \text{[22]}$$

where E_d is the band gap energy for direct transitions and hv is the photon energy. From the intersection of the extrapolated linear portion, the E_d values of the CeO_2 nanospheres, microrods, spindle-like particles and bulk samples can be determined as 3.46, 3.62 and 3.36 eV, respectively. Compared to the non-oriented polycrystalline CeO_2 (E_d = 3.19 eV determined by UV-vis spectroscopy),[23] CeO_2 nanospheres, microrods and spindle-like particles showed an increase in E_d by a value exceeding 0.27, 0.43, 0.17 eV respectively, due to the quantum size effect. The blue-shifting in the UV absorption spectra of CeO_2 nanocrystals has attracted much interest of many researchers in recent years. [24] Generally, the absorption of ceria in the UV region

originates from the charge-transfer transition between the O2p and Ce4f states in O^{2-} and Ce^{4+}. This absorption is much stronger than the $4f^1$-$5d^1$ transition from the Ce^{3+} species in the mixed valence ceria system.[22, 25] It was theoretically deduced that the value of blue-shifting resulting from the reduction of particle size is inverse proportional to the square of the size due to quantum confinement effect. Tsunekawa *et al.* stated that the blueshifts could also be explained by changes in the electronic band structure.[25d]

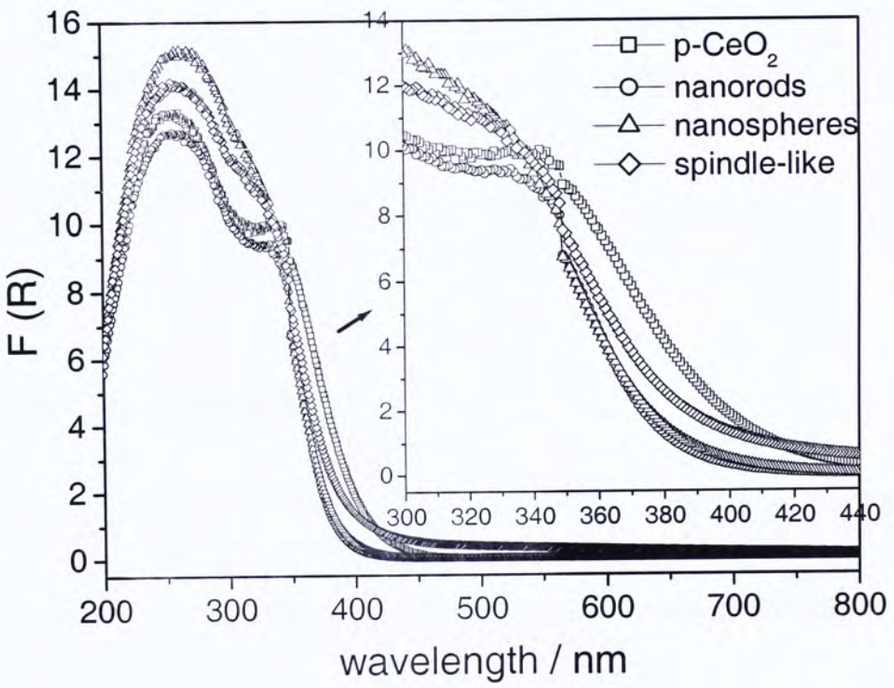

Figure 3.13 UV spectra for annealed CeO_2 nanospheres, microrods and spindle-like particles.

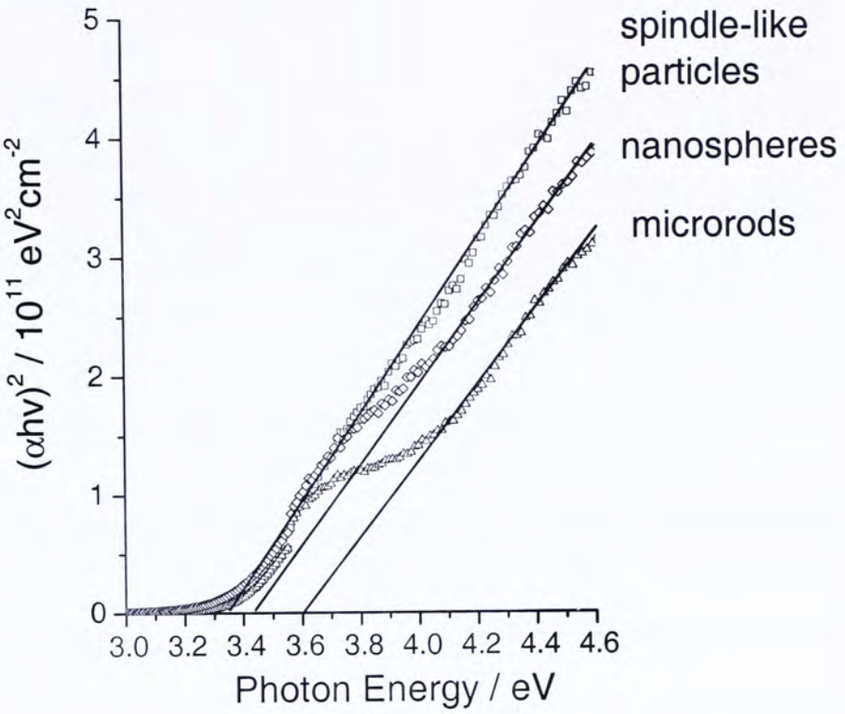

Figure 3.14 Plots of $(\alpha hv)^2$ vs. photon energy for annealed CeO_2 nanospheres, microrods and spindle-like particles.

3.3.9 Thermal Catalysis Study

The spherical, rod-shaped and spindle-like anneal CeO_2 samples as well as reference sample (P-CeO_2) were tested for their ability to oxidize carbon monoxide:

$$CO + \frac{1}{2} O_2 \rightarrow CO_2$$

Figure 3.15 shows the catalytic activity profiles of CO conversion for the samples. The results of the catalytic activity measurements are summarized in Table 3.4. The spindle-like sample shows the highest CO conversion rates 0.861 μmol $g^{-1}s^{-1}$, which is almost 4.5 times of that for our reference P-CeO_2, 0.189 μmol $g^{-1}s^{-1}$. The large

difference in catalytic activity is partly due to the variation in surface area. The surface area of the spindle-like sample is 170.0 m^2g^{-1} but that of P-CeO_2 calcined at 600°C is only 65.3 m^2g^{-1}.

Interestingly, the surface area and pore volume for the three types of samples are almost the same (Table 3.3) but the spindle-like and rod-shaped samples show much higher catalytic activities than the nanospheres. XRD analysis indicates that the order of lattice cell volume is spindle-like ≈ rod-shaped > spherical (Table 3.2) and the lattice cell expansion is strongly related to the degree of Ce(IV) reduction and the extent of oxygen vacancy.[26] In addition to the surface area, structural defects and oxygen vacancy also have a positive effect on CO oxidation.[26] The formation of oxygen vacancy can be expressed by the following equation:

$$4Ce^{4+}{}_{(s)} + O^{2-}{}_{(s)} \rightarrow 4Ce^{4+} + 2e^{-}/V_{(O,s)} + \frac{1}{2}O_2 \rightarrow 2Ce^{4+}, 2Ce^{3+}{}_{(s)} + V_{(O,s)} + \frac{1}{2}O_2$$

where $V_{(O, s)}$ represents an empty position (anion-vacant site) originating from the removal of O^{2-} from the lattice. Charge balance is maintained by the reduction of two cerium cations from +4 to +3. The radius of the Ce^{3+} ion (1.14Å) is larger than that of Ce^{4+} (0.97Å) and hence the lattice expansion is a consequence of the reduction of Ce^{4+} ions to Ce^{3+}.[27] There is a gradual decrease in the concentration of oxygen vacancies extended from the surface to the bulk. Such gradient enables the

outward diffusion of lattice oxygen to the surface. Therefore, reduction of Ce^{4+} to Ce^{3+} by oxygen ion leads to the generation of surface oxygen vacancy. These oxygen vacancies can act as promoting sites for NO and CO conversion. According to the lattice cell parameters in Table 3.2, we would expect the extent of Ce^{4+} reduction to be spindle-like ≈ rod-shaped > spherical. Fornasiero *et al.*[28] reported that the stress induced by the decrease of unit cell volume would create structural defects and generate oxygen vacancies. Moreover, the smaller crystalline size in the spindle-like microstructure also provides a larger percentage of atoms at the edges and corners (Table 3.2). The cerium and oxygen atoms at these locations are more chemically active.[29]

Table 3.4 Summary of results from CO oxidation measurements

	T_{50} (°C)	Rate / μmol $g^{-1}s^{-1}$	Ea / kJ mol^{-1}
P-CeO_2	294	0.189 (250°C), 1.019 (300°C)	69.80
Sphere	284	0.332 (250°C), 1.300 (300°C)	57.55
Rods	265	0.646 (250°C), 1.347 (300°C)	43.44
Spindle-like	250	0.861 (250°C), 1.554 (300°C)	52.55

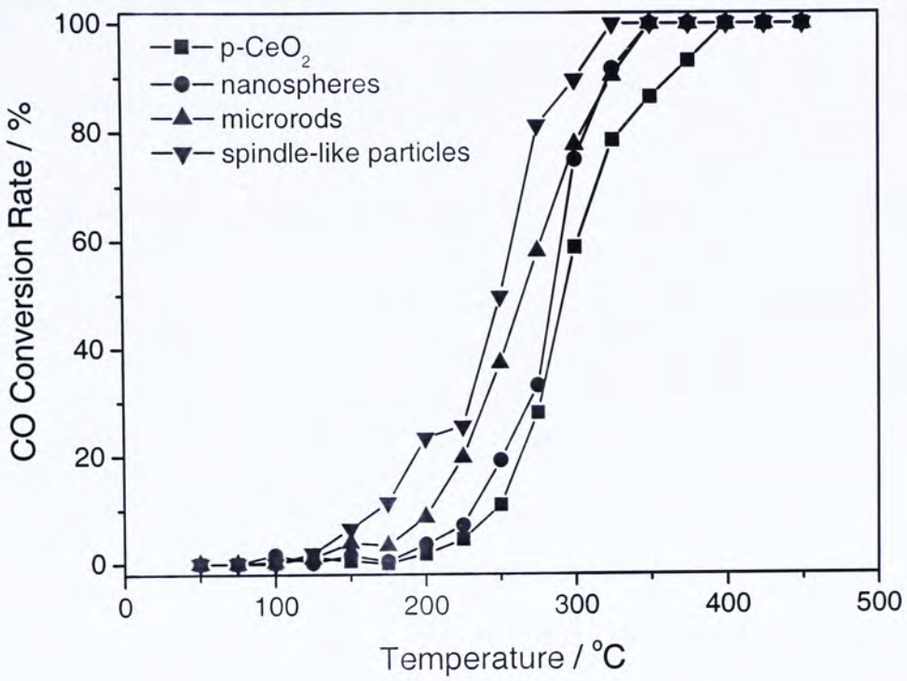

Figure 3.15 CO conversion as a function of temperature over CeO_2 nanospheres, microrods and spindle-like microstructure.

3.4 Conclusion

We have successfully fabricated uniform CeO_2 nanospheres, microrods and spindle-like microstructure using a one-step procedure. Our results indicate that the morphology is controllable by the duration of reaction and the concentration of the cerium precursor. We believe that the decomposition of ammonium cerium nitrate and the redox reaction involving ethylene glycol leads to the growth of CeO_2 nanostructures. The band gap energies of these CeO_2 nanomaterials are found to be shape-dependent (microrods > nanospheres > spindle-like particles). The higher catalytic activity on CO conversion in spindle-like particles can be explained from

the extent of Ce(IV) reduction and the oxide anion vacancies. The simple preparation approach holds promise in the future large-scale synthesis of morphology-controllable CeO_2 for applications in solid electrolytes and electrochromic devices.

3.5 Reference

(1) (a) Y. Xia, P. Yang, Y. Sun, Y. Wu, B. Mayers, B. Gates, Y. Yin, F. Kim, H. Yan, *Adv. Mater.* **2003**, *15*, 353. (b) C. M. Lieber, *Solid State Commun.* **1998**, *107*, 607. (c) R. E. Smalley, B. I. Yakobson, *Solid State Commun.* **1998**, *107*, 567. (d) J. Hu, L. S. Li, W. Yang, L. Mamnna, L. W. Wang, A. P. Alivisatos, *Science* **2001**, *292*, 2060.

(2) (a) T. S. Ahmadi, Z. L. Wang, T. C. Green, A. Henglein, M. A. El Sayed, *Science* **1996**, *272*, 1924. (b) W. Huynh, X. G. Peng, A. P. Alivisatos, *Adv. Mater.* **1999**, *11*, 923. (c) H. Mattoussi, L. H. Radzilowski, B. O. Dabbousi, E. L. Thomas, M. G. Bawendi, M. F. Rubner, *J. Appl. Phys.* **1998**, *83*, 7965. (d) W. C. W. Chan, S. M. Nie, *Science* **1998**, *281*, 2016.

(3) (a) G. R. Patzke, F. Krumeich, R. Nesper, *Angew. Chem. Int. Ed.* **2002**, *41*, 2446. (b) Z. L. Wang, *Adv. Mater.* **2003**, *15*, 432.

(4) (a) Y. Wang, X. Jiang, Y. Xia, *J. Am. Chem. Soc.* **2003,** *125*, 16176. (b) X. Jiang, Y. Wang, T. Herricks, Y. Xia, *J. Mater. Chem.* **2004**, *14*, 695. (c) Y. Sun, Y. Xia, *Adv. Mater.* **2003**, *15*, 695. (d) Y. Sun, B. Mayers, Y. Xia, *Adv. Mater.* **2003**, *15*, 641. (e) Y. Sun, B. Mayers, Y. Xia, *Nano Lett.* **2003**, *3*, 675. (f) Y. Sun, B.

Mayers, T. Herricks, Y. Xia, *Nano Lett.* **2003**, *3*, 955. g) C. Feldmann, *Adv. Funct. Mater.* **2003**, *13*, 101.

(5) E. Lifshitz, M. Bashouti, V. Kloper, A. Kigel, M. S. Eisen, S. Berger, *Nano Lett.* **2003**, *3*, 857.

(6) (a) J. Zhang, L. Sun, J. Yin, H. Su, C. Liao, C. Yan, *Chem. Mater.* **2002**, *14*, 4172. (b) L. Vayssieres, *Adv. Mater.* **2003**, *15*, 464. (c) C. Pacholski, A. Kornowski, H. Weller, *Angew. Chem. Int. Ed.* **2002**, *41*, 1188. (d).J. Y. Lao, J. G. Wen, Z. F. Ren, *Nano Lett.* **2002**, *2*, 1287.

(7) L. A. Perez-Maqueda, L. Wang, E. Matijevic, *Langmuir* **1998**, *14*, 4397.

(8) (a) Z. R. Dai, Z. W. Pan, Z. L. Wang, *Adv. Funct. Mater.* **2003**, *13*, 9. (b) N. S. Ramgir, I. S. Mulla, K. P. Vijayamohanan, *J. Phy. Chem. B* **2004**, *108*, 14815.

(9) N. Pinna, M. Willinger, K. Weiss, J. Urban, R. Schlogl, *Nano Lett.* **2003**, *3*, 1131.

(10) B. C. H. Steele, *Solid State Ionics* **2000**, *129*, 95.

(11) S. C. Laha, R. Ryoo, *Chem. Commun.* **2003**, 2138.

(12) (a) T. Masui, K. Fujiwara, K. I. Machida, G. Y. Adachi, *Chem. Mater.* **1997**, *9*, 2197. (b) R. X. Li, S. Yabe, M. Yamashita, S. Momose, S. Yoshida, S. Yin, T. Sato, *Solid Sate Ionics* **2002**, *151*, 235.

(13) (a) H. J. Beie, A. Gnoerich, *Sens. Actuators B.* **1991**, *4*, 393. (b) P. Jasinski, T. Suzuki, H. U. Anderson, *Sens. Actuators B* **2003**, *95*, 73.

(14) J. M. Pemba-Mabiala, M. Lenzi, J. Lenzi, A. Lebugle, *Surf. Interf. Analysis* **1990**, *15*, 663.

(15) Y. M. Chiang, E. B. Lavik, I. Kosacki, H. L. Tuller, J. Y. Ying, *Appl. Phys. Lett.* **1996**, *69*, 185.

(16) Y. W. Zhang, R. Si, C. S. Liao, C. H. Yan, C. X. Xiao, Y. Kou, *J. Phy Chem B*, **2003**, *107*, 10159.

(17) S. Carrettin, P. Concepcion, A. Corma, J. M. Lopez Nieto, V. F. Puntes, *Angew. Chem. Int. Ed.* **2004**, *43*, 2538.

(18) (a) M. Yada, S. Sakai, T. Torikai, T. Watari, S. Furuta, H. Katsuki, *Adv. Mater.* **2004**, *16*, 1222. (b) C. Sun, H. Li, Z. X. Wang, Li, Chen, X. Huang, *Chem. Lett.* **2004**, *33*, 662. (c) G. S. Wu, T. Xie, X. Y. Yuan, B. C. Cheng, L. D. Zhang, *Mater. Res. Bull.* **2004**, *39*, 1023.

(19) (a) A. E. Nelson, K. H. Suhulz, *Appl. Surf. Sci.* **2003**, *210*, 206. (b) A. Pfau, K. D. Schierbaum, *Surf. Sci.* **1994**, *321*, 71. (c) G. U. Kulkarni, C. N. R. Rao, M. W. Roberts, *J. Phys Chem.* **1995**, *99*, 3310. (d) A. Kotani, H. Mizuta, T. Jo, J. C. Parlebas, *Solid State Commun.* **1985**, *53*, 805. (e) E. Wuilloud, B. Delley, W. D. Schneide, Y. Baer, *Phys. Rev. Lett.* **1984**, *53*, 202. (f) S. Tsunekawa, T. Fukuda, T.; Kasuya, A. *Surf. Sci.* **2000**, *457*, L437.

(20) J. Z. Shyu, W. H. Weber, H. S. Gandhhi, *J. Phys. Chem.* **1988**, *92*, 4964.

(21) C. Bock, C. Paquet, M. Couillard, G. A. Botton, B. R. MacDougall, *J. Am. Chem. Soc.* **2004**, *126*, 8028.

(22) R. A. Van Leeuwen, C. J. Huang, D. R. Kammler, J. A. Switzer, *J. Phys Chem. B* **1995**, *99*, 15247.

(23) Z. Z. Orel, B. Orel, *Phys. Status Solidi B* **1994**, *186*, K33.

(24) (a) M, Inoue, M. Kimura, T. Inui, *Chem. Commun.* **1999**, 957. (b) L. X. Yin, Y. Q. Wang, G. S. Pang, Y. Koltypin, A. Gedanken, *J. Colloid Interface Sci.* **2002**, *246*, 78.

(25) (a) S. Tsunekawa, T. Fukuda, *J. Appl. Phys.* **1999**, *87*, 1318. (b) S. Tsunekawa, R. Sahara, Y. Kawazoe, A. Kasuya, *A. Mater. Trans. JIM* **2000**, *41*, 1104. (c) T. Murata, M. Sato, H. Yoshida, K. Morinaga, *J. Non-Cryst. Solids* **2005**, *351*, 312.

(d) S. Tsunekawa, J. T. Wang, Y. Kawazoe, A. Kasuya, *J. Appl. Phys.* **2003**, *94*, 3654.

(26) A. Trovarelli, *Catalysis by Ceria and Related Materials*, Imperial College Press, London, **2002**, pp 15-50.

(27) R. D. Shannon, C. T. Prewitt, *Acta Cryst. B.* **1969**, *25*, 925.

(28) P. Fornasiero, R. Di Monte, G. Ranga Rao, J. Kašpar, S. Meriani, A. Trovarelli, and M. Graziani, *J. Catal.*, **1995**, *151*, 168.

(29) (a) C. Burda, X. Chen, R. Narayanan, M. A. El-Sayed, *Chem. Rev.*, **2005**, *105*, 1025. (b) R. Di Monte, J. Kaspar, *J. Mater. Chem.*, **2005**, *15*, 633.

Chapter Four

Conclusion

A series of hierarchically macro-mesostructured $Pd/Ce_xZr_{1-x}O_2$ three-way catalysts have been prepared by using a surfactant-assisted method. These particles contain a macroporous array having diameters of 1-2 μm. They are usually of one-dimensional orientation, parallel to each other, and that extend through almost the whole particle. These hierarchically mesoporous macroporous networks are preserved even at a high cerium content of 60% and after calcination at 800°C. These frameworks possess large BET surface area and pore volume, and favor surface Ce^{4+} reduction and oxide anion vacancy formation. Moreover, samples prepared from this templating method show higher phase homogeneity than the ones obtained from the co-precipitation method. The carbon monoxide conversion rate for macro-mesostructured sample (Pd-MM60) is much higher than the sample which prepared by the traditional method (Pd-CP60). The superior performance of Pd-MM60 can be explained by its large surface area, porous texture, better chemical homogeneity, high oxide anion vacancy and structural defects.

We also successfully fabricated uniform CeO_2 nanospheres, microrods and spindle-like particles using simple route. Our results show that the morphology is controllable by the duration of reaction and the concentration of the cerium precursor. We believe that the decomposition of ammonium cerium nitrate and redox reaction involving ethylene glycol leads to growth of CeO_2 nanostructures. From the results of GC-MS analysis, the rate of conversion of ethylene glycol to oxalic is a rate-determining step for the formation of cerium formate microrods/spindle-like particles. The band gap energies of these CeO_2 nanomaterials are found to be shape-dependent (microrods > nanospheres > spindle-like particles). The higher catalytic activity on CO conversion in spindle-like particles can be explained by the extent of Ce(IV) reduction and oxide anion vacancies. The smaller-size crystalline also provides a larger percentage of edge and corner atoms. The cerium and oxygen atoms at these locations are more chemically active. The simple preparation approach holds promise in the future large-scale synthesis of morphology-controllable CeO_2 for applications in solid electrolytes and electrochromic devices.

List of Publications

C. M. Ho, J. C. Yu, T. Y. Kwong, A. C. Mak, "Morphology Controllable Synthesis of Mesoporous CeO_2 nanostrucutres, " *Chemistry of Materials*, in press.

C. M. Ho, J. C. Yu, X. C. Wang, S. Y. Lai, Y. F. Qiu, "Meso- and Macro-porous $Pd/Ce_xZr_{1-x}O_2$ as Novel Oxidation Catalysts," *Journal of Materials Chemistry*, 15, 2193 – 2201 (2005).

X. C. Wang, J. C. Yu, **C. M. Ho**, A. C. Mak, "A Robust Three-Dimensional Mesoporous Ag/TiO2 Nanohybrid Film," *Chemical Communications*, 17, 2262-2264 (2005).

X. C. Wang, J. C. Yu, C. **M. Ho**, Y. D. Hou, X. Z. Fu, "Photocatalytic Activity of a Hierarchically Macro/Mesoporous Titania," *Langmuir* 21, 2552-2559 (2005).